Virginia Commonwealth University
VCU Scholars Compass

Theses and Dissertations

Graduate School

2009

ORGAN MOTION AND IMAGE GUIDANCE IN RADIATION THERAPY

Jining Zhou
Virginia Commonwealth University

ORGAN MOTION AND IMAGE GUIDANCE IN RADIATION THERAPY

A dissertation submitted in partial fulfillment of the requirements for the degree of Doctor of Philosophy at Virginia Commonwealth University.

By

JINING ZHOU
M.S., Virginia Commonwealth University, 2001
B.S., Central South University of Science and Technology, China, 1992

Director: DING-YU FEI, PH.D.
ASSOCIATE PROFESSOR, DEPARTMENT OF BIOMEDICAL ENGINEERING

VIRGINIA COMMONWEALTH UNIVERSITY
RICHMOND, VIRGINIA
May, 2009

Acknowledgement

There are many people I would like to thank for their various contributions to the research presented in this dissertation.

First of all, I would like to thank my advisor, Dr. Ding-Yu Fei, for his encouragement, support, and mentoring over the past several years. He guided me to form the dissertation topic, helped me to keep the research on track, and encouraged me to solve the technical problems with persistence. I cannot imagine having a better advisor and mentor for my Ph.D., and without his knowledge and perceptiveness, I would never have finished this work.

I would like to thank Dr. Steve Jiang and Dr. Lily Wang from the Department of Radiation Oncology, University of California, San Diego, for sharing their views and interests on my research topics, and giving their feedback on specific technical details of 4DCT imaging and deformable registration. I would like to thank Dr. Yeh-Chi Lo from Mount Sinai Medical Center, NYC, for his valuable suggestion on the clinical implementation of image guidance on tumor margin reduction.

I would like to thank all my colleagues from the Department of Radiation Oncology, Sharp Grossmont hospital, for their help to obtain the clinical data I needed in this work.

I would also like to thank my committee members, Dr. Martin L. Lenhardt and Dr. Ou Bai from School of Engineering, Dr. Kenneth A. Kraft and Dr. Azhar Rafiq from School of Medicine, for carefully reviewing this manuscript, and for offering criticism and suggestions.

Finally, I dedicate this dissertation to my husband, Li-ke Gao, for his support in every respect.

Table of Contents

List of Tables

List of Figures

List of Abbreviations

3DCT	Three-Dimensional Computed Tomography
4DCT	Four-Dimensional Computed Tomography
ACR	American College of Radiology
AP	Anterior-Posterior (Vertical)
CT	Computed Tomography
CBCT	Cone Beam CT
CTV	Clinical Target Volume
D_{max}	Maximum Dose to Target
D_{min}	Minimum Dose to Target
D_{mean}	Mean Dose to Target
DQA	Delivery Quality Assurance
DRR	Digitally Reconstructed Radiograph
DOF	Degree of Freedom
DVH	Dose Volume Histogram
EOE	End of Exhale
EOI	End of Inhale
EPID	Electronic Portal Image Device
fx	Fraction
GTV	Gross Tumor Volume
Gy	Gray (A unit of absorbed radiation)

HAT   Hexaphant Accuracy Test

HN   Head and Neck

ICRU   International Commission on Radiation Units and Measurements

IGRT   Image Guided Radiation Therapy

IMRT   Intensity Modulated Radiation Therapy

ITK   Insight Tool Kit

ITV   Internal Target Volume

KVCT   Kilo Voltage Computed Tomography

LR   Left-Right (Lateral)

M   Slope factor in Lyman Normal Tissue Complication Probability model

MVCT   Mega Voltage Computed Tomography

N   Volume-effect parameter in Lyman Normal Tissue Complication

           Probability model

NTCP   Normal Tissue Complication Probability

OAR   Organ at Risk

PET   Positron Emission Tomography

PTV   Planning Target Volume

PTV_{3D} Planning Target Volume drawn from 3D CT scan

PTV_{4D} Target Volume drawn from 4D CT scan

RPM   Real-time Position Management

SBRT   Stereotactic Body Radiation Therapy

SI   Superior-Inferior (Longitudinal)

SD	Standard Deviation
SPSS	Statistical Package for the Social Sciences
TD	Tolerance Dose
$TD_{5/5}$	Tolerance dose that could cause 5% complication within 5 years
$TD_{50/5}$	Tolerance dose that could cause 50% complication within 5 years

Abstract

ORGAN MOTION AND IMAGE GUIDANCE IN RADIATION THERAPY

By Jining Zhou, Ph.D.

A dissertation submitted in partial fulfillment of the requirements for the degree of Doctor of Philosophy at Virginia Commonwealth University.

Virginia Commonwealth University, 2009

Major Director: Ding-Yu Fei, Ph.D.
Associate Professor, Department of Biomedical Engineering

Organ motion and inaccurate patient positioning may compromise radiation therapy outcome. With the aid of image guidance, it is possible to allow for a more accurate organ motion and motion control study, which could lead to the reduction of irradiated healthy tissues and possible dose escalation to the target volume to achieve better treatment results. The studies on the organ motion and image guidance were divided into the following four sections.

The first, the interfractional setup uncertainties from day-to-day treatment and intrafractional internal organ motion within the daily treatment from five different anatomic sites were studied with Helical TomoTherapy unit. The pre-treatment mega voltage computed tomography (MVCT) provided the real-time tumor and organ shift coordinates, and can be used to improve the accuracy of patient positioning. The interfractional system errors and random errors were analyzed and the suggested margins for HN, brain, prostate, abdomen and lung were derived.

The second, lung stereotactic body radiation therapy using the MIDCO ^{TM} BodyLoc whole body stereotactic localizer combined with TomoTherapy MVCT image guidance were investigated for the possible target and organ motion reduction. The comparison of 3D displacement with and without BodyLoc immobilization showed that, suppression of internal organ motion was improved by using BodyLoc in this study.

The third, respiration related tumor motion was accurately studied with the four dimensional computed tomography (4DCT). Deformable registration between different breathing phases was performed to estimate the motion trajectory for lung tumor. Optimization is performed by minimizing the mean squared difference in intensity, and is implemented with a multi-resolution, gradient descent procedure.

The fourth, lung tumor mobility and dosimetric benefits were compared with different PTV obtained from 3DCT and 4DCT. The results illustrated that the PTV_{3D} not only included excess normal tissues but also might result in missed target tissue. The normal tissue complication probability (NTCP) from 4D plan was statistically significant smaller than 3D plan for both ipsilateral lung and heart.

CHAPTER 1

Introduction: Image Guided Radiation

Therapy and Organ Motion

The patient's position and anatomy during the course of radiation therapy usually vary from those used for therapy planning purposes. This is mainly due to patient movement, inaccurate patient positioning, and organ motion. Consequently, the actual received dose distribution differs from the planned absorbed dose distribution. This difference will compromise the clinical treatment results with either insufficient dose coverage of targeted tumor or overdose to normal tissue. A detailed study needs to be conducted to determine how much the position related organ motion could exist during routine clinical treatment, and how much improvement could be reached with the help of precise patient position systems and rigid immobilization devices. However, even when the external body is immobilized and rigid, the internal motion of organs due to physiological processes still remains a challenge which affects the treatment results. With the usage of the recently developed four dimensional CT scanner, the internal organ motion could be studied in a more accurate way so better treatment results could be achieved.

1.1 Background

Radiation therapy plays an important role in multi-modality treatment for cancer patients. Its effectiveness in controlling a tumor is proportional to the dose of radiation delivered, and this is traditionally explained in a linear–quadratic model of cell killing.[1]

In this model, the radiation dose to tumor killing levels is limited by the damage caused to nearby normal tissues, or in other words, the irradiated volume of normal tissue during the development of radiation-induced toxicity. To lift this limit, one method is to create a conformal dose distribution that tightly matches the shape of the targeted tumor volume, without increasing the irradiated volume of nearby normal tissues. Recent technical advances in planning and delivering intensity-modulated radiation therapy (IMRT) provide such an unprecedented means that produces exquisitely shaped radiation doses to treat tumor with conformal high dose and, at the same time, spare normal tissue with sharp dose gradient.[2-4] Figure 1.1 demonstrates the features and advances of IMRT beam delivery characteristics to target and normal tissues, as compared to traditional 3D conformal radiation therapy.

By allowing the escalation of the radiation dose, IMRT has increased the tumor killing levels. It has further improved the outcomes by increasing organ sparing, providing better local control of disease, and reducing treatment associated morbidity and toxicity, and thus enhances quality of life.[5, 6]

During the IMRT treatment, accurate patient setup and reproducible anatomic motion are essential in minimizing the margin and providing high dose gradient around tumor. In clinic, large uncertainties exist in tumor motion management, inaccurate patient positioning, and target localization due to inter- and intrafractional organ motions. (The definition of these motions will be explained later in this chapter.) Patient's anatomy and position during the course of radiation therapy usually vary from those when they underwent simulation for the purpose of treatment planning. Consequently, the actual received absorbed dose distribution differs from the planned absorbed dose distribution.

These two effects lead to insufficient dose coverage of the targeted tumor volume and over dosage of normal tissues, and hence potentially compromise the clinical results.

(a)   (b)
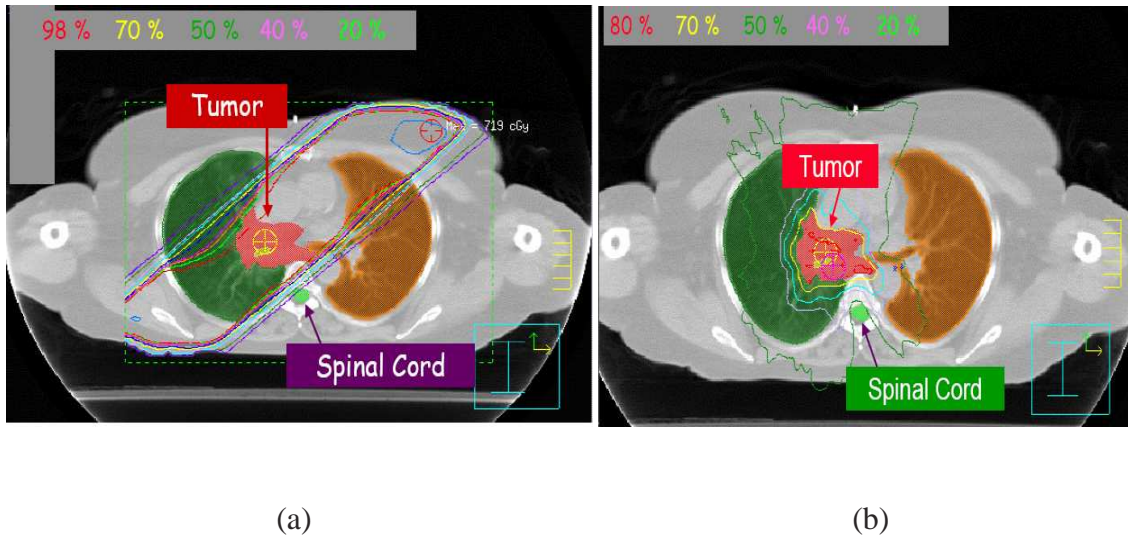
Figure 1.1 Comparison of traditional conformal 3D planning (a) and IMRT planning (b)

The recent advance of image-guided radiotherapy (IGRT) has provided a means to target tumors more accurately while effectively sparing the normal tissues. The basic idea of IGRT is to provide image guidance tool before, during and after the radiation treatment process. Specifically, it allows registering the daily images to a reference image set that has usually been generated at the time of treatment planning and, by doing so; it can represent the ideal situation (i.e., better alignment of treatment beam and target volume). This image registration helps to find the transformation (translation, rotation and deformation) that maps the real time patient image set onto the one when patients underwent CT simulation to obtain the corresponding adjustments.

With the better knowledge of the exact position of the tumor and the better control of organ motion to be established during treatment, the planning target volume (PTV)

margins of patient set-up can be substantially decreased (e.g., from centimeters to millimeters). This leads to a substantial reduction in the volume of radiated normal tissue volume.[7-10]

1.2 Current Techniques in Image Guided Radiation Therapy

The clinical applications of IGRT for patient set-up verification and correction can be generally classified as either an off-line or an online approach. The off-line approach, also known as adaptive radiotherapy (ART), monitors the position of the patient during a limited number of fractions and adapts the safety margins and the treatment plan accordingly. The online approach offers the real time observation and adjustment of patient position, which usually requires automating the quantification and correction of target localization errors so it can be efficiently used in clinical routine.

IGRT approaches make use of imaging modalities that range from planar imaging to fluoroscopy to CT based solutions. Currently, the four mostly frequently used IGRT techniques are electronic portal imaging devices, ExacTrac Novalis system, Varian On-Board Imager™, and TomoTherapy. The following sections describe each of the first three techniques, and details the last one, as TomoTherapy is the one main platform studied in this dissertation. Additionally, this section also presents the recent breakthrough of IGRT, the four-dimensional CT (4DCT) technique that can generate spatial and temporal information on mobility in a single investigation.

1.2.1 Electronic Portal Imaging Devices

For the last 30 years, weekly port films have been used as routine clinical standard for ensuring accurate targeting of external beam radiotherapy.[11] The early

studies on port films indicated the benefits of portal film verification before the treatment on the weekly basis. [12, 13] The subsequent studies have characterized the magnitude and nature of setup errors for a variety of clinical conditions. The importance of geometric accuracy has driven the development of digital imagers that can monitor treatment accuracy more effectively than weekly port filming,[14] with minimal increase in workload.[15] The modern era of electronic portal imaging devices (EPIDs) began in the early 1980s with the demonstration of a fluoroscopic system to acquire megavoltage transmission images.[16] The introduction of the scanning liquid ionization chamber system in 1990 [17] was quickly followed by the introduction of camera-based fluoroscopic EPIDs from other manufacturers.

An EPID can acquire images automatically with near real time display, store them digitally, and provide quantitative analysis tools. Studies have shown that the increased portal imaging frequency can reveal daily variations in patient alignment that are not observed with weekly filming.[18, 19] Furthermore, an EPID can provide immediate patient alignment information, without the delay involved in processing a film. This instant-image availability enables the development of on-line correction protocols and daily targeting adjustments.[20, 21] In addition to aiding acquisition, the digital nature of EPIDs can be exploited to enhance the portal review process. Studies have examined the process of subjective portal image evaluation by clinicians and have found a wide variation among reviewers in reporting setup deviations in portal images.[22, 23] Many EPID systems offer computer-assisted image review with anatomy-matching routines and quantitative alignment analysis.

However, poor soft tissue contrast and unclear projection of the bony anatomy are usually observed in this approach. To improve the situation, planar KV x-ray imaging has been implemented in a variety of systems. Although these systems have shown significantly increased contrast for bony structure differentiation, observing soft-tissue detail remains problematic and correcting the daily organ motion is still challenging.

1.2.2   ExacTrac Novalis System

The ExacTrac Novalis system, developed by Brain LAB company, combines a robotic couch and an infrared tracking system to subtract patient's anatomy information on the basis of bony structures or the implanted radio-opaque markers in the tumor, and superpose the real time two orthogonal images on the planning orthogonal digitally reconstructed radiographs (DRRs).[24-26] In this system, a set of the infrared reflective markers is placed on the patient's chest area that allows real-time monitoring of the patient's position in space and extraction of a respiratory signal (Figure 1.2). Two flat-panel detectors mounted to the ceiling and two X-ray tubes embedded in the floor are used to subtract 3D information of the patient's anatomy on the basis of bony structures or implanted radio-opaque markers. Robotic couch is used to adjust translational and rotational set-up errors before treatment. The beam on–off signal of the linear accelerator (LINAC) is triggered by the respiratory signal that is obtained from the real-time tracking of the infrared reflective markers.

<center>(a)   (b)</center>
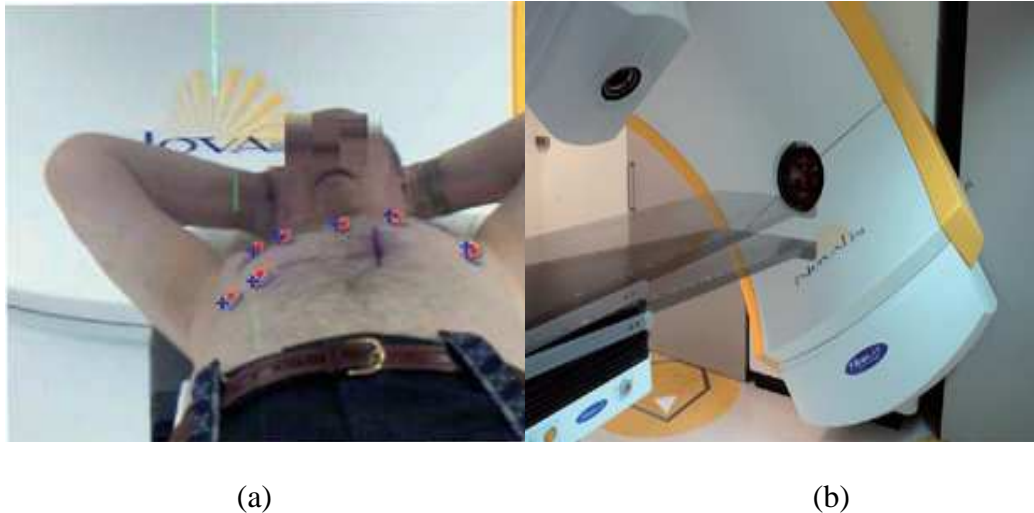
Figure 1.2 ExacTrac Novalis system (Brain LAB). (a) a set of reflective markers are placed on the patient chest area allowing real-time monitoring of the patient's position in space and extraction of a respiratory signal; (b) a robotic couch to adjust translational and rotational set-up errors before treatment.

The ExacTrac Novalis system usually is used for stereotactic radiosurgery or stereotactic radiotherapy for brain or body, and can provide a high precision tumor location and thus accurate tumor targeting. The disadvantage of this technique is that the images are 2D and there is no volume information could be obtained at the current development stage.

1.2.3   On-Board Imager™

The On-Board Imager™ (OBI) is one of the volumetric imaging systems that are designed for online image guidance. It enables clinicians to obtain high resolution kilo-voltage x-ray images prior to treatment, and register those digital images against the reference (i.e., planning) digital images. Patient position could be adjusted automatically

when necessary. A kilovoltage x-ray source and large-area flat-panel digital detector on either the Clinac® or Trilogy™ medical linear accelerators are used for radiography, volumetric cone-beam CT, or fluoroscopy. In this highly integrated form, the control system combines imaging and delivery components in a single machine.

Figure 1.3 Example of Clinical setup with OBI. The system incorporates an x-ray tube and an amorphous-silicon flat-panel image detector on a pair of robotic arms.

The OBI is mounted on the treatment machine gantry via two robotically-controlled arms; each operate along 3 axes of motion (i.e., lateral, longitudinal and vertical), so that they can be positioned optimally for the best possible imaging of the target volume (Figure 1.3). The KV imaging system operates in a plane orthogonal to the megavoltage treatment beam and its associated amorphous silicon PortalVision™ imager. The amorphous silicon flat-panel x-ray image detectors yield digital images showing internal anatomic landmarks with a high degree of spatial accuracy and soft tissue detail. The imaging software then registers pre treatment images against a set of corresponding

reference images. These reference images can be radiographs acquired on a simulator or they can be DRR images computed from the volumetric CT data set used in treatment planning. The matched image sets are then overlaid with registration tools for visual verification and confirmation. Once the match is accepted, the corrected position offsets are automatically downloaded to the treatment couch, which can be repositioned remotely from outside the treatment vault.

The most useful imaging modality in this system is cone beam CT (CBCT). In this mode, an entire volumetric CT data set is reconstructed with a single gantry rotation, while the patient and treatment couch remain stationary. The overall CBCT process is very similar to the radiographic repositioning technique, except that 3D CBCT images, rather than a pair of radiographs, are acquired. The CBCT operating mode is preferred when direct visualization of 3D soft-tissue detail is important for patient repositioning prior to treatment, e.g., prostate, pancreas, liver tumor, etc. CBCT imaging can also be used when small targets are being treated without fiducial markers, or when a small number of treatment fractions are being used (e.g., hypofractional radiosurgery), or when adaptive planning is desired.[27-30] In the OBI system, image acquisition, image registration, image match and verification, and automatic remote repositioning of the treatment couch are all integrated to optimize efficiency.

The disadvantages of kilo-voltage cone-beam CT are that it is not of diagnostic quality, and the soft tissue contrast need to be further improved. Another disadvantage is that the imaging acquisition time is too long for real-time volumetric scanning.

1.2.4   Helical TomoTherapy System

Helical TomoTherapy is a volumetric image-guided, fully dynamic, IMRT delivery system. It was developed at the University of Wisconsin and is now commercially manufactured as the TomoTherapy Hi·Art System.[31, 32] While standard radiotherapy is delivered using a few static fields, helical TomoTherapy delivers treatment with a rotating, intensity-modulated fan beam. The beam delivery is similar to that of helical or spiral computed tomography (CT) and requires slip rings to transmit power and data. The patient is continuously translated through the ring gantry resulting in a helical source trajectory about the patient. The ring gantry provides a stable and accurate platform to perform tomographic verification of both the patient setup and delivered dose. The design of the helical TomoTherapy unit allows for continuous delivery over 360 degree beam angles.

In addition to the full integration of IMRT delivery, an important advance with helical TomoTherapy over the other current systems is the ability to provide accurate verification of radiation delivery via onboard megavoltage computed tomography (MVCT). The daily use of its pretreatment MVCT imaging for patient setup verification allows clinicians to correct for setup errors in a real time manner. In particular, image guidance using MVCT allows for direct target position verification when the patient is in the actual treatment position just prior to therapy delivery.

1.2.4.1 Architecture of Helical TomoTherapy System

The TomoTherapy treatment unit has an 85 cm source to axis distance (SAD) and produces a fan beam with a width of 40 cm and a length of 1.0, 2.5 or 5 cm.

TomoTherapy's binary multi-leaf collimator is composed of 64 individual leafs of 0.6 cm width which are pneumatically driven in a binary fashion for intensity-modulation. The TomoTherapy Hi•ART System consists of the components described below and is illustrated in Figure 1.4.

(1) Planning Station

The Planning Station is used to prescribe a treatment and calculate an optimized plan for treatment based on CT acquisition and structure definition data.

(2) Optimization Server

The Optimization Server is where the dose optimization calculations are performed. This device uses dedicated hardware to accelerate the optimization process.

(3) Data Server

The Data Server (located with the Optimization Server) is used to store data for rapid patient data search and retrieval and is connected to the Optimization Server, Planning Station, and Operator Station.

(4) Operator Station

The Operator Station (located outside the treatment room) is used to perform MVCT scans and treatment procedures after the patient has been positioned in the treatment. The Operator Station is also used to perform image registration after an MVCT scan has been acquired.

(5) Status Console

The Status Console (located adjacent to the Operator Station) is used to select the procedure type and start a procedure. It also supports a Stop button and Emergency-stop button.

(6) Power Control Panel

The Power Control Panel is mounted to the side of the gantry enclosure. It is used primarily to turn power ON and OFF to the system and indicate the status of the system during operation.

(7) Positioning Control Panel

A Positioning Control Panel is mounted to the front-left and front-right side of the gantry enclosures. Each panel is used to manually and automatically move the couch during patient setup, as well as give the current position of the couch and the moveable lasers.

(8) Rotating Gantry Assembly

The linear accelerator and CT detector subsystems are mounted to a covered Rotating Gantry Assembly. The temperature control subsystem is also mounted on the rotating gantry.

(9) Patient Couch

The Patient Couch is a composite flat couch top used to support the patient and move the patient through the rotating gantry.

(10) Laser System

A Class II laser system (not pictured in Figure 1) is used with the delivery subsystem to help the operator position the patient for MVCT and treatment procedures.
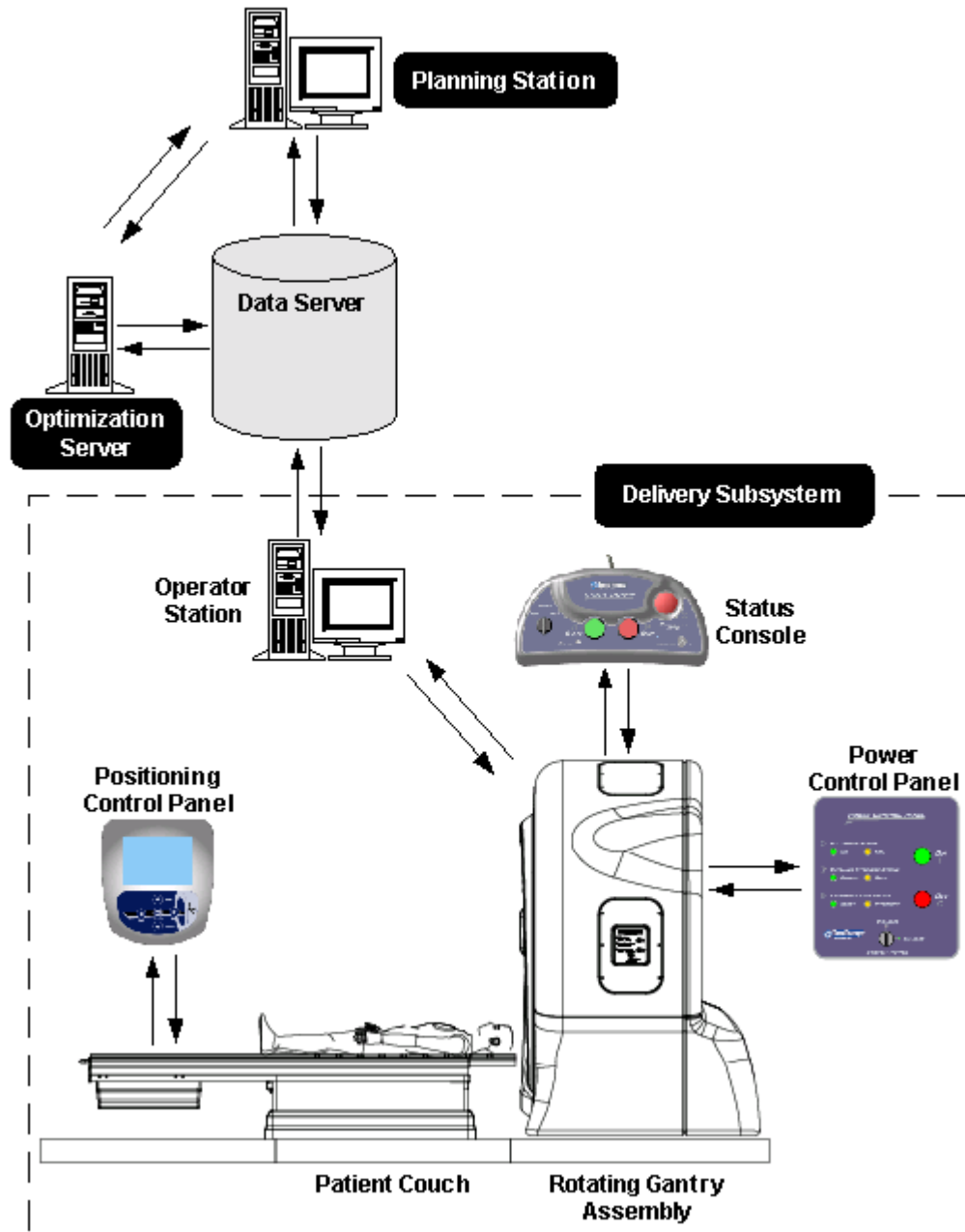
Figure 1.4 Illustration of TomoTherapy Hi•ART System components (picture from TomoTherapy operation menu)

1.2.4.2 MVCT Imaging Chain

MVCT images system consists of a ring gantry with a xenon ion-chamber array mounted opposite the radiation source.[31] The nominal energy of the incident electron beam is reduced from 6 MeV to 3.5 MeV [33] for the imaging mode. The source-to-detector distance is 145 cm and the source-to-axis distance is 85 cm. The imaging field of view (FOV) is defined by the width of the HI-ART multi-leaf collimator, which projects to 40 cm at isocenter. Figure 1.5 illustrates the Diagram of TomoTherapy mega-voltage CT imaging chain.
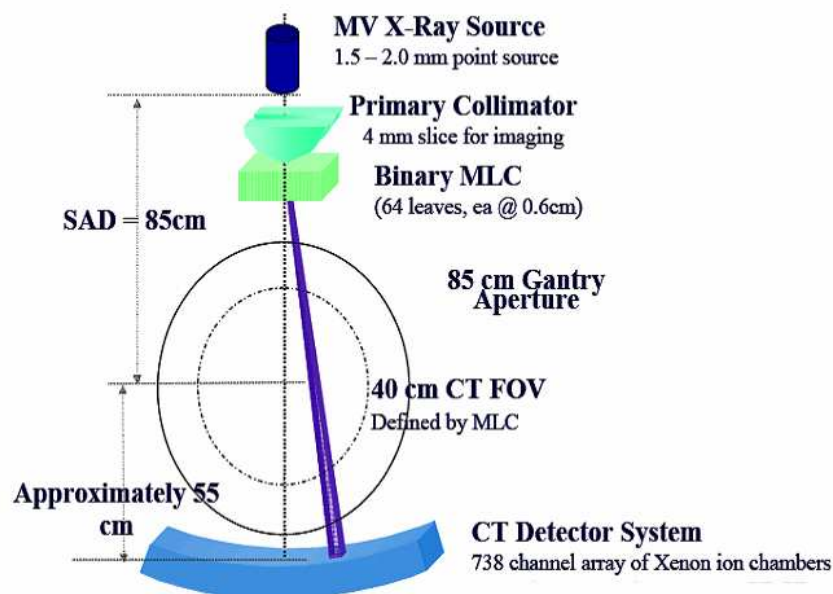
Figure 1.5 Diagram of TomoTherapy mega-voltage CT imaging chain

During MVCT acquisition, the beam is collimated to a length of 5 mm and a width of 400 mm at isocenter. The slice spacing resolution of the MVCT images is determined by the distance that the couch travels per rotation. MVCT images acquired with TomoTheapy system have a user-defined axial resolution. There are three clinical MVCT acquisition modes (fine, normal and coarse) available for clinical use. Each mode corresponds to pitch ratio of 1, 2 and 3. The pitch is the couch travel distance per gantry rotation divided by the axial beam width at the axis of rotation for single detector array scanner (e.g. MVCT scanner). So the couch travels 4mm, 8 mm and 12 mm per rotation for fine, normal, and coarse respectively. About 180 degrees per slice (the rays back-projected through angles 0-179 are equivalent to the rays back-projected through angles 180-359) is needed to reconstruct the image, and therefore there are two slices per rotation (which gives 2mm per slice for fine, 4mm per slice for normal, and 6mm per slice for coarse). The Axial (or in-plane) resolution is 0.78mm pixel. (400mm/512 =0.78 mm)

$$\text{Pitch} = \frac{\text{Couch increment per rotation (mm)}}{\text{Beam collimation (mm)}}$$

If pitch <1, implies image overlapping and higher patient dose; if pitch >1, implies extended imaging and reduced patient dose.

Once the MVCT is reconstructed it is registered with the planning KVCT to determine if the patient or phantom is positioned correctly for treatment. All MVCT images that were acquired for this work were registered automatically with the automatic registration program in TomoTherapy, and visually adjusted by therapists if necessary, and finally verified by physician. Axial, sagittal and coronal views of the two image sets

are available during registration. Translational and rotational adjustments can be made to the MVCT image set. The KVCT structure set was unaltered and superimposed on the MVCT anatomy (Figure 1.6). MVCT Scans are usually obtained within 5 minutes, according to how large the scan area might be.
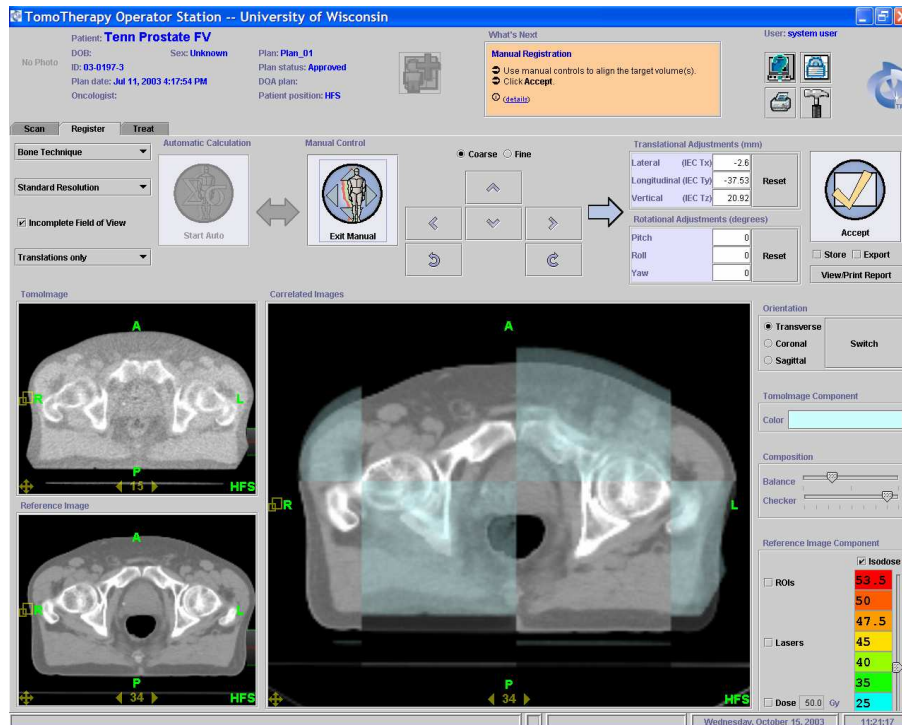
Figure 1.6 Example of image registration with prostate using TomoTherapy unit. Left upper: MVCT which is taken before daily treatment, left lower: kilovoltage computed tomography image, and center: registration of both images shown overlaid in checker box format.

The result from MVCT to KVCT anatomical matching is a computed offset with 6 degrees-of-freedom (6DOF). They are lateral, longitudinal and vertical translations plus the in-plane rotations (pitch and yaw) and rotation variation (roll). These offsets are automatically computed with the TomoTherapy automatic image registration algorithm.

For TomoTherapy Hi ART MVCT system, the principal interactions during the image acquisition are Compton scattering and pair production. These interactions are not as sensitive as regular CT scanner to high atomic number material. As a result, bony structure (with a higher number of Z) is less distinct from fat and muscle when imaged with high energy photons. These phenomena cause MVCT to exhibit lower soft tissue contrast than regular KVCT.

1.2.5 Four-Dimensional Computed Tomography

Recently, a 16-slice CT scanner became available, and it allowed for four-dimensional (4D) or respiration-correlated CT scans to be performed. 4DCT scans generate spatial and temporal information on mobility in a single investigation and represent a major breakthrough in imaging for radiotherapy planning.[34] In this technique described as retrospective gating, the respiratory waveform is synchronously recorded during CT acquisition, and multiple CT slices are acquired at each table position for at least the duration of one full respiratory cycle.[35] With four-dimensional computed tomography (4DCT), multiple CT volumes that are consistent in respiratory phase are reconstructed, each representing a different respiratory state of the patient. 4DCT scans can capture intrafractional tumor mobility for radiotherapy planning and generate accurate internal target volume (ITV), which covers the movement range of clinical tumor volume (CTV). It was recently reported that using 4DCT to determine ITV for lung cancer could substantially reduce the planning target volume (PTV) while safely covering the target.[36, 37]

1.3 Terminology Related to Motion of the Tumor Volume

Tumor motion is commonly accounted for by the use of margins that encompass the tumor volume. ICRU (International Commission on Radiation Units and Measurements) Reports 50 and 62 [38, 39] define the relevant terminology. First, the gross tumor volume (GTV) is defined as the volume containing demonstrated tumor. Second, the clinical target volume (CTV) is defined to enclose the GTV plus a margin to account for suspected tumor involvement. The planning target volume (PTV) is defined as the CTV plus a margin to allow for geometrical variations such as patient movement, positioning uncertainties, and organ motion. In ICRU Report 62, this margin is further divided into two components: (a) internal margin (IM) to account for variations in size, shape, and position of the CTV; and (b) setup margin (SM) to account for uncertainties in patient position and beam alignment. For daily radiation therapy treatment, the uncertainties could be further categorized into inter- and intra- fraction according to whether the treatment is done within the single treatment day: interfractional setup uncertainties were defined as the setup error between daily treatments for the whole course of radiation. Intrafractional organ motion was defined as the shift between the KVCT and the pre-treatment MVCT scan after the first treatment session and before the second treatment sessions of a single treatment day.

1.4 Purpose of the Study

Patient motion is inevitably involved in medical imaging and radiation therapy, producing artifacts and uncertainties in target identification, delineation, localization and treatment.[40, 41] Several factors contribute to the overall treatment accuracy. Among them,

the image modality, the treatment setup accuracy and organ motion are the three major sources of treatment uncertainty:

- The first source is the geometrical uncertainties that are involved during the obtaining of image modalities, such as the limited image resolution, the characteristic of the imaging modality, and tumor delineation uncertainties.

- The second source, the setup uncertainties, occurs during the planning simulation and patient treatment. Specifically, the setup error, which has both a random and systematic component, arises from the motion between the skin tattoos that are obtained during simulation and the internal anatomy motion or changes during the time of daily treatment.

- The third source of the treatment uncertainty is the organ motion, which could arise from respiratory motion, cardiac motion, digestive motion, muscular motion, etc.

This study chooses TomoTherapy as the clinical platform to analyze the setup uncertainties and organ motion. It is assumed that the tumor contour is outlined accurately, i.e., there is no CTV delineation uncertainty in this study. The imaging techniques focused on assuring the patient is in the proper position prior to treatment, so individual treatment margins can be used, rather than population-based margins. The purpose of this study is to investigate how much the error and motions were included in the daily treatment and how much margin could be given for the specific anatomic sites in a specific clinic practice, (i.e., daily patient treatment in Grossmont hospital with TomoTherapy unit). Furthermore, effects of respiration on the organ motion will be

investigated with 4DCT. More specifically, this study has investigated the following four aspects.

Firstly, the interfractional setup uncertainties from day-to-day treatment and intrafractional internal organ motion within the daily treatment from different anatomic sites were studied with Helical TomoTherapy unit. The pre-treatment MVCT provided the real-time tumor and organ shift coordinates, and can be used to improve the accuracy of patient positioning. The interfractional setup errors, system errors and random errors were analyzed and the suggested margin for HN, brain, prostate, abdomen and lung in the direction of lateral, longitudinal and vertical was derived from the study.

Secondly, lung stereotactic body radiation therapy (SBRT) using the MIDCO BodyLoc whole body stereotactic localizer combined with TomoTherapy megavoltage CT (MVCT) image guidance were investigated for the possible target and organ motion reduction. The comparisons of 3D displacement with BodyLoc immobilization and without BodyLoc immobilization were performed and analyzed.

Thirdly, 4DCT is investigated to accurately describe respiration related tumor motion. Deformable registration between different breathing phases was performed to estimate the motion trajectory during the respiratory cycle for lung tumor. Optimization is realized by minimizing the mean squared difference in intensity, and is implemented with a multi-resolution, gradient descent procedure.

Finally, lung tumor mobility and dosimetric benefits with 4DCT were investigated with different planning target volume (PTV) obtained from 3DCT and 4DCT. The PTV_{4D} obtained from 4D image was compared with the PTV_{3D} from 3D

images. The normal tissue complication probability (NTCP) from both 3D and 4D plan was compared for both ipsilateral lung and heart.

1.5 Roadmap

This dissertation was organized in the following chapters: Chapter 2 investigated the daily interfractional setup uncertainties and intrafractional internal organ motion from five different anatomic sites; Chapter 3 performed the detailed analysis of how much improvement could be achieved with proper immobilization devices for stereotactic radiation therapy; To describe the tumor and organ motion in an accurate way, Chapter 4 presented the 4DCT technique for moving target delineation and deformable registration that correlates images in different respiratory phases; Chapter 5 analyzed the patient internal organ motion with 4DCT and the associated dosimetric effects; Finally, Chapter 6 summarized all the studies and directed the future work that could be done from the studies.

CHAPTER 2

Analysis of Daily Setup Variation with TomoTherapy

Mega Voltage Computed Tomography (MVCT)

2.1 Introduction

Intensity-modulated radiation therapy has been shown to benefit the patient by delivering uniform high doses of radiation to the target while at the same time, reducing the radiation exposure of surrounding normal tissues. However, it becomes riskier if the target is partially missed due to miscalculation of the tumor's location. The ICRU Report 62 [39] defines a margin that should be included in the definition of a planning target volume (PTV), which includes internal margin (IM) to account for variations in size, shape, and position of clinical target volume (CTV) and setup margin (SM) to account for uncertainties in the positioning of the patient.

Numerous authors have published setup accuracy studies that explored the use of different imaging methods for guidance. For example, portal image,[42, 43] ultrasound,[44, 45] cone-beam CT [46,47] and embedded internal markers [48,49] have been used to study interfractional setup uncertainties and intrafractional organ displacements and deformations. Generally, image guidance can be classified into two categories: on-line and off-line approaches. The on-line approach refers to pre-treatment image guidance, and has the advantage of being used for real-time patient position verification and adjustment. The off-line approach involves a retrospective review of patient setup

variation to allow for patient position adjustments during the subsequent treatment, and has the advantage of potentially reducing both treatment time and systematic setup error.

The purpose of this study was to evaluate the setup uncertainties using TomoTherapy megavoltage computed tomography (MVCT) for five different anatomical sites. Helical TomoTherapy provides on-line verification of radiation delivery via on-board MVCT imaging to verify tumor position and shape before treatment. With an anatomy registration tool, the patient can be repositioned more accurately. In this study, both pre-treatment and post-treatment MVCT scans were performed to quantify the interfractional setup error and the intrafractional internal organ displacement.

2.2 Methods and Materials

2.2.1 Patients and Image Registration between MVCT and KVCT

Ninety-two consecutive patients treated between December 2005 and May 2008 with tumors in five different locations (25 HN, 15 brain, 27 prostate, 9 abdomen, and 16 lung patients) were identified from patient database. Their fraction numbers varied according to tumor site. For example, HN patients were treated with 20-38 fractions, brain patients with 25-35 fractions, prostate patients with 30-35 fractions, abdomen patients with 25-30 fractions, and lung patients with 25-35 fractions.

The patients were brought to the CT simulator and immobilized in the supine position. A Type-S™ head extension board (CIVCO, Orange City, Iowa, USA) with a thermoplastic facemask was used for HN and brain patients. Vac-Lok™ cushions (CIVCO) were used to immobilize the lower extremities up to the thighs for prostate patients. No respiration suppression or immobilization devices were used for lung and

abdomen treatments. For each patient, the CT images were taken and transferred to a commercial planning system (ADAC, Philips) for contouring. The final RT structure sets and CT images were transferred to TomoTherapy for treatment planning.

The MVCT scans from the TomoTherapy unit for all patients in this study were performed at a fixed gantry period of 10 seconds per full rotation. MVCT images were acquired at a rate of one slice per 5 seconds using a 3.5 megavoltage x-ray fan beam. Before treatment, patients were positioned according to skin tattoos marked during the CT-simulation (KVCT). A normal slice thickness (4 mm spacing with pitch of 2) was chosen for all patients. A set of image slices across a region that included the tumor location was chosen for the subsequent MVCT scan. MVCT images were taken and fused with the planning KVCT using mutual information/extracted feature fusion algorithm focused on both soft tissues and bony structures. 3D translational (lateral, longitudinal, and vertical) and rotational corrections were calculated using the TomoTherapy software. The operator performed manual adjustment if the automatic image fusion did not match the KVCT data. Pitch and yaw was reset to zero since there was no automatic couch adjustment function in the TomoTherapy treatment unit; the lack of such a feature would make this procedure difficult and tedious for routine daily treatment. Roll adjustment was performed using automatic gantry rotation if necessary. The system allows for automatic vertical and longitudinal movements consistent with the registration results. The lateral shift was manually adjusted by the therapist. Patients were repositioned to the shift coordinates and treated.

The bony structures or sinuses were used for adjusting the results from automatic registration for HN and brain tumor patients. The interface between prostate and rectum

was used for prostate patients' image registration. When the tumor was in soft tissue, such as abdomen and lung, the tumor itself was used to verify that it was centered inside the prescribed isodose lines in all 3D translational directions. Other anatomic structures, like the kidney or liver, were also used to assist the registration for the correctness adjustment.

2.2.2 Inter- and Intrafractional Uncertainties

Interfractional uncertainty was defined as the setup variation and organ displacement for each fraction of treatment. After matching the setup tattoos and lasers, the discrepancy between planning KVCT and pre-treatment MVCT was considered the interfractional uncertainty. The intrafractional uncertainties were derived from the discrepancy of MVCTs taken immediately before and after a treatment. A total of 2900 recorded daily shift data points were collected and analyzed for interfractional setup variation analysis. A total of 115 post-treatment MVCTs were performed immediately after treatment to investigate the intrafractional organ displacements. The intrafractional variation study was performed for five randomly chosen patients, with five fractions for each patient.

The systematic and random errors were analyzed according to the method suggested by Bijhold et al.[50] Mean and standard deviations in daily measurements were first obtained for each patient. The mean and standard deviation of the mean across treatments for all patients were then calculated. The systematic group mean, μ, is the mean of all data means. Systematic error Σ is determined from the standard deviation of the means of the displacements between the planning KVCT scan and the pretreatment

MVCT scan. The root mean square of standard deviation from all patient data gives the random setup error, denoted σ. CTV-to-PTV setup margin were suggested by Stroom[51] and Herk:[52]

$$\text{CTV-to-PTV margin} = 2.0\ \Sigma + 0.7\ \sigma \tag{2.1}$$

Where Σ is systematic error and σ is random error.

Several variables were defined as the following: The position of the tumor center of mass in relation of the planned position is given by x_{ik}, where x_{ik} is a vector of the three spatial dimensions. The subscripts represent the patient number and fractions of treatment of each patient:

$k = 1, \ldots, P$, P is the number of patients;

$I = 1, \ldots, I_k$, I_k is the number of fractions per patient k.

$$Group\ mean = M(m_k) = \frac{\sum_{k=1}^{p} I_k m_k}{\sum_{k=1}^{p} I_k} \tag{2.2}$$

$$System\ error = \Sigma^2(m_k) = \frac{1}{\sum_{k=1}^{p} I_k - 1} \sum_{k=1}^{p} I_k (m_k - M(m_k))^2 \tag{2.3}$$

$$Random\ error = RMS^2 = \frac{1}{\sum_{k=1}^{p} I_k - 1} \sum_{k=1}^{p} ((I_k - 1)s_k^2) \tag{2.4}$$

Where s_k is the standard deviation of daily treatment $s_k^2 = \frac{\sum_{i=1}^{i_k} (x_i - m_i)^2}{\sum_{i=1}^{i_k} I_k - 1}$.

The CTV-to-PTV margin including both setup error and internal motion (i.e., global margin) could be expressed as:

$$\text{CTV-to-PTV margin} = \text{setup margin} + \text{internal organ motion margin} \qquad (2.5)$$

An ANOVA test with Bonferroni post-hoc comparison at a 95% confidence level (SPSS, V 16.0) was used to analyze the differences among the five anatomy sites. The three displacement directions were also analyzed with an ANOVA test. The comparisons between interfractional and intrafractional displacements were analyzed using Student's t-test. Correlations between the random setup errors and the patient's characteristics, e.g., age, weight, and sex, were analyzed using Pearson's correlation coefficient.

2.3 Results and Discussion

The values of mean setup variation and standard deviation for each patient from the five anatomic sites are shown in Figure 2.1. Group means, standard deviations of averages, and mean three-dimensional vectors of the setup variations are summarized in Table 2.1. The mean interfractional 3D displacements for HN (2.2 mm) and brain (2.3 mm) were smaller than the displacements for prostate (3.2 mm), abdomen (4.4 mm), and lung (7.7 mm). The mean rotational variation ranged from 0.2° to 0.5°, with standard deviation from 0.7° to 0.9°. The immobilization device (e.g., thermoplastic facemask) and the rigid anatomy in the intracranial group may contribute to the similar setup uncertainties for HN and brain patients. The extracranial group showed a larger setup error than the intracranial group. The largest setup error was found in lung patients in the longitudinal direction. There was no significant difference in the vertical direction and roll variation among the five anatomic sites.

Table 2.1 Mean and standard deviation of interfractional setup variations from 92 patients in lateral (LR), longitudinal (SI), vertical (AP) and rotational directions across five different sites.

Site	# of patients	LR (mm) Mean	LR (mm) S.D.	SI (mm) Mean	SI (mm) S.D.	AP (mm) Mean	AP (mm) S.D.	Roll (°) Mean	Roll (°) S.D.	mean 3D displacement (mm)
HN	25	0.4	1.6	-0.3	2.5	0.3	2.2	0.3	0.9	2.2
Brain	15	0.6	1.7	-0.8	2.4	0.2	1.3	0.2	0.9	2.3
Prostate	27	-1.2	5.1	0.4	2.5	0.6	4.7	0.5	0.7	3.2
Abdomen	9	0.9	4.9	-1.8	5.1	-0.2	3.2	0.5	0.9	4.4
Lung	16	0.5	4.0	-6.0	4.8	1.8	3.3	0.3	0.8	7.7

Abbreviations: LR: left-right (lateral), SI: superior-inferior (longitudinal), AP: anterior-posterior (vertical). SD: Standard Deviation.

Table 2.2 Interfractional uncertainties and maximum displacements for six anatomic sites.

Site	systematic error Σ X	Y	Z	Roll	random error σ X	Y	Z	Roll	maximum displacement mm, or degree X	Y	Z	roll
HN	1.5	1.6	0.4	0.6	1.7	2.5	2.4	0.9	8.6	8.7	6.0	5.8
Brain	1.5	1.6	0.3	0.6	2.6	2.6	1.3	0.9	8.5	10.1	4.3	2.5
Prostate	1.9	2.4	0.8	0.7	5.2	2.6	5.4	0.7	12.6	12.9	10.3	3.7
Abdomen	2.3	4.0	0.8	0.6	5.1	4.0	3.6	0.9	13.4	18.2	10.9	3.5
Lung	2.7	4.3	1.9	0.6	2.8	4.9	4.3	0.8	14.3	20.2	12.1	5.1

Abbreviations: X: LR (lateral); Y: SI (longitudinal); Z: AP(vertical).

The interfractional systematic errors, random errors, and maximum displacements for all patients are summarized in Table 2.2. The random error was larger than the

systematic error in all directions for all tumor sites. Roll variations were small and no significant difference among the five sites studied was found.

The comparison of inter- and intrafractional shifts is shown in Figure 2.2. Site numbers 1-4 represent HN, prostate, abdomen, and lung, respectively. The intrafractional patient and organ movements were generally smaller than the interfractional setup errors. However, except for lung in the longitudinal direction, the differences were not statistically significant. The maximum intrafractional displacement for all four sites was less than 4.5 mm.

The Pearson product-moment correlation coefficient was calculated to analyze relationship between the standard deviation of random setup error and patient characteristics, i.e., age, weight, and sex. The significance of the correlation was tested and no correlation was found.

Setup errors and organ displacements were larger in the extracranial tumor sites. The lung had the highest shifts in all three directions. Not surprisingly, the longitudinal shift in the lung was greater than other two directions because of breathing motion. Table 2.3 lists the interfractional setup uncertainties for one site versus the rest using an ANOVA test with Bonferroni post-hoc methods.

(a)

(b)

(c)

(d)
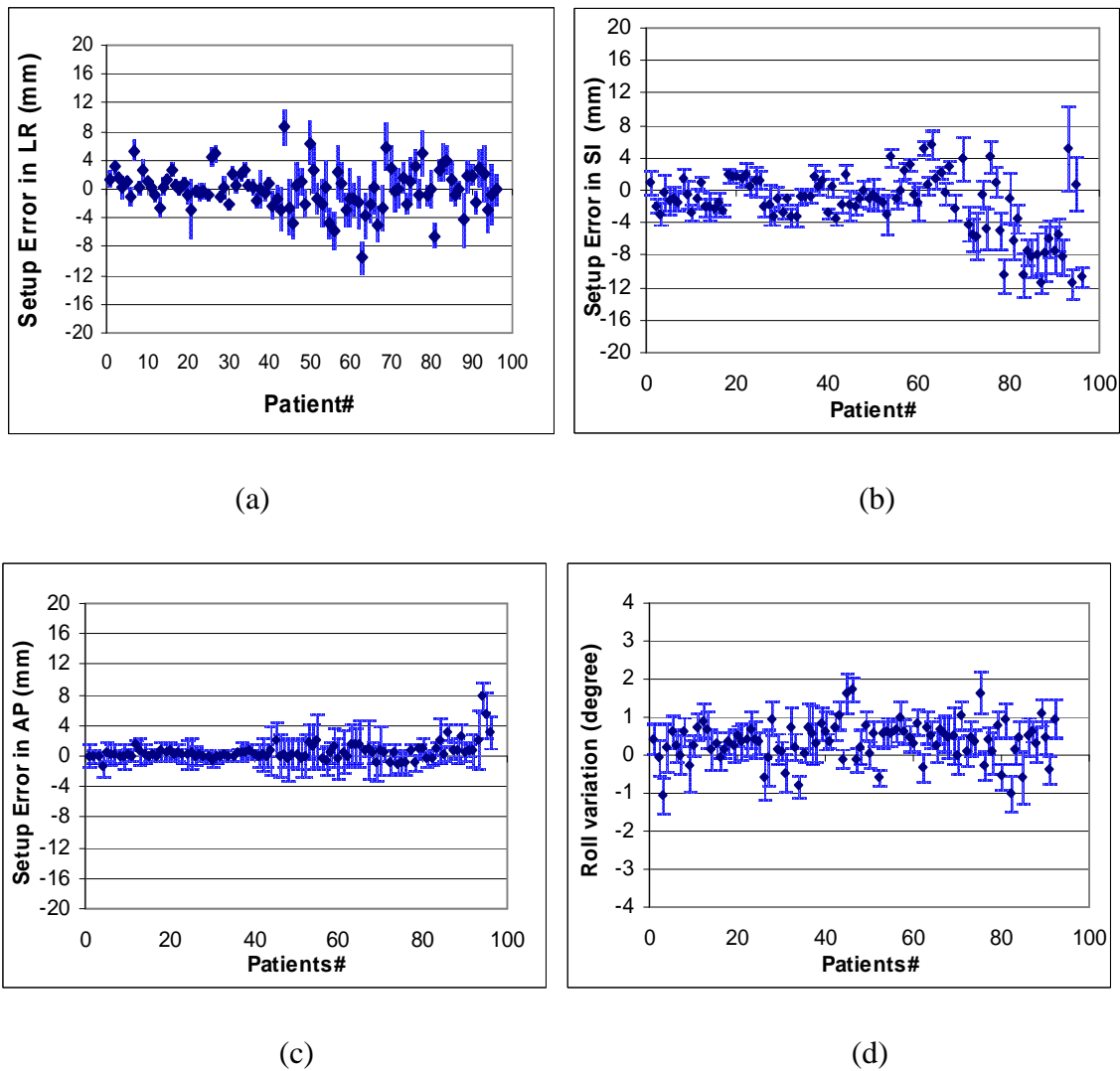
Figure 2.1 Interfractional setup uncertainty for each patient. HN cases were patient #1 to #25; brain: # 26 to 40; prostate: #41 to 67; abdomen: #68 to 76; lung: #77 to 92. Each point indicates the mean setup error and the standard deviation of a patient. Panel: (a) setup errors in lateral (LR); (b) longitudinal (SI); (c) vertical direction (AP); and (d) setup errors in rotation.

(a)   (b)

(c)   (d)
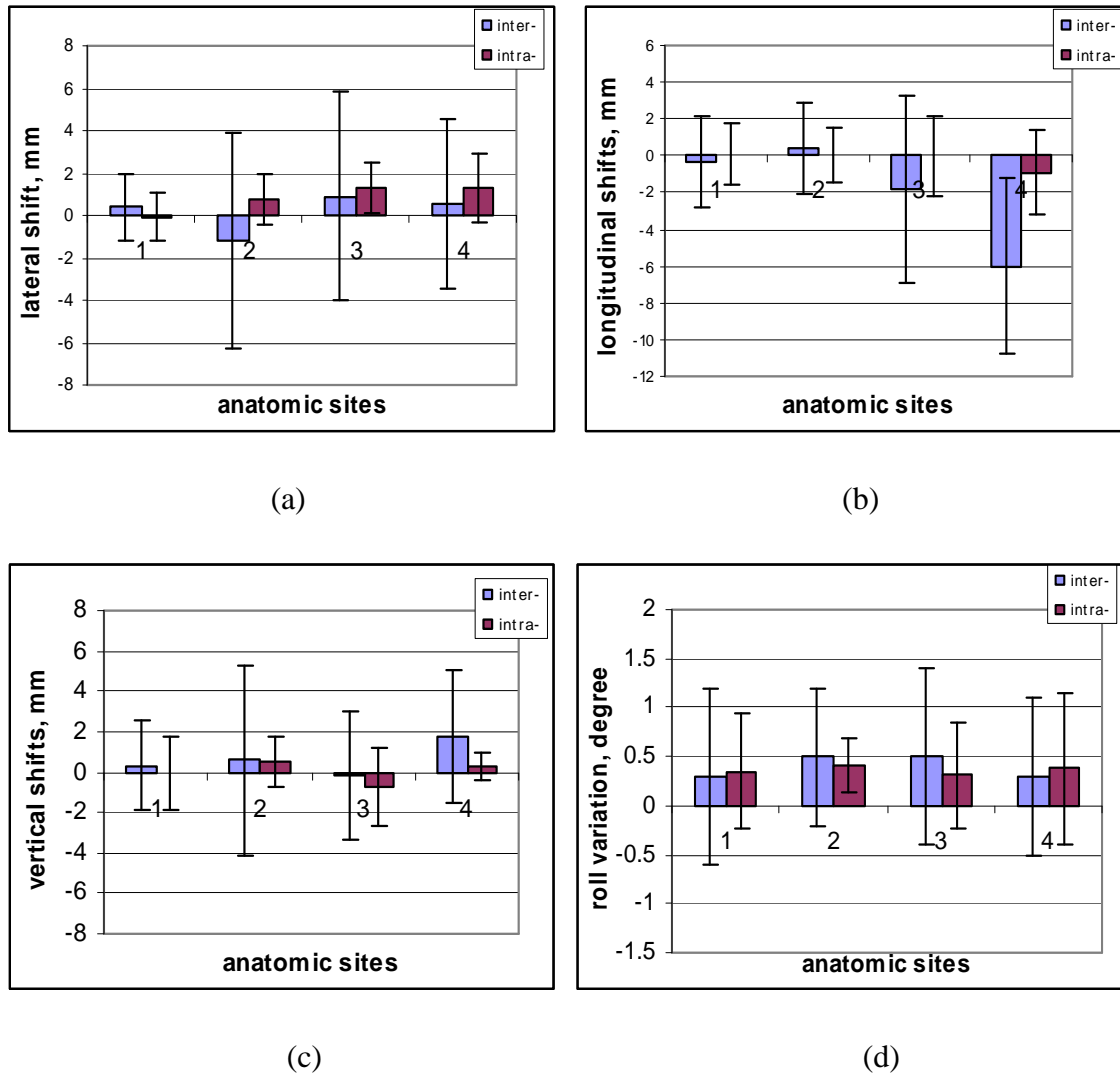
Figure 2.2 Comparison of interfractional and intrafractional uncertainties in the case of

HN (1), prostate (2), abdomen (3), and lung (4). Means and standard deviations are

shown.

Table 2.3 Significance (p<0.05) of site-dependent interfractional setup uncertainties.

	HN				Brain			Prostate		Abdomen
	Brain	Prostate	Abdomen	Lung	Prostate	Abdomen	Lung	Abdomen	Lung	Lung
LR	ns*	<0.05	<0.05	<0.05	<0.05	<0.05	<0.05	ns	ns	ns
SI	ns	ns	<0.05	<0.05	ns	<0.05	<0.05	<0.05	<0.05	<0.05
AP	ns	ns	ns	ns	ns	ns	ns	ns	ns	ns
Roll	ns	ns	ns	ns	ns	ns	ns	ns	ns	ns

*: Not significant (>0.05)

Setup uncertainties for HN and brain tumors showed a smaller variation compared to tumors in the extracranial sites in this study, i.e., abdomen and lung. The largest setup variation was found in the lung, which may be due to respiratory movements.[53, 54] The effect of respiratory motion could be reduced by instructing the patient to hold their breath, or by using a gating device.[36, 55, 56] In a preliminary study, it was found that thermoplastic immobilization suppressed breathing significantly and reduced the setup and organ displacements from 3.5 mm to 1.7 mm (p<0.01) when the same group of patents were treated with or without immobilization device for lung treatment. Detailed data will be reported separately in Chapter 3.

Tumor displacement in the lung is difficult to quantify and reproduce.[57-59] The movement varied with tumor location and size, and across individual patients. For example, the last two data points in Figure 2.1b were derived from tumors in the upper lobe, where these two patients showed a larger variation compared to other lung patients. Due to the limited number of patients in this study, the results need to be verified with investigations specifically designed to test the relationship between organ displacement and tumor location. 4DCT could be used to obtain more spatial and temporal information

about the effect of mobility on lung tumors, and this content will be discussed in detail in Chapter 4 and Chapter 5.

Table 2.4 Calculated CTV-to-PTV margins for global margin, interfractional setup margin and internal motion margin. Margin calculation follows Stroom's equation.

	Global Margin, mm			Internal Organ margin, mm			Setup Margin, mm		
	x	y	z	x	y	z	x	y	z
HN	4.2	5.0	2.5	2.1	2.9	0.4	2.1	2.1	2.1
Brain	4.8	5.0	1.5	1.9	2.5	0.3	2.9	2.5	1.2
prostate	7.4	6.6	5.4	2.2	2.3	1.7	5.2	4.3	3.7
abdomen	8.2	10.8	4.1	2.4	5.6	1.8	5.8	5.2	2.3
lung	7.4	12.0	6.8	1.9	5.4	1.7	5.5	6.6	5.1

Abbreviations: same as Table 2.2.

While IGRT reduces setup errors and certain random errors, it cannot mitigate uncertainty due to patient/organ movements during a treatment fraction unless a real-time monitoring device is used. If IGRT is not available, Stroom suggests a margin between CTV-to-PTV to deliver a full dose to the tumor. The equation suggested by Stroom is 2.0 Σ+0.7 σ, where Σ is systematic error and σ is random error. This margin is intended to cover 99% of CTV volume, a region that receives 95% of the prescribed dose.

The calculated CTV-to-PTV margins for global margin, interfractional setup margin and internal motion margin were summarized in Table 2.4. The internal organ margin obtained from the internal organ motion study and it indicated the extents of internal organ motion during the study. The setup margin was obtained from the interfractional setup variation study and it indicated the daily movement of organ or target. The suggested margins ranged from 4.2 to 8.2 mm, 5.0 to 12.0 mm, and 1.5 to 6.8 mm, for lateral, longitudinal, and vertical directions, respectively. These results were

comparable to other studies in the literature evaluating setup variations. For example, the setup variations for HN and brain were reported between 2-5 mm (lateral), 1-5 mm (longitudinal), and 1-6 mm (vertical);[60] prostate setup variation ranged from 5-8 mm (lateral), 4-12 mm (longitudinal), and 3-10 mm (vertical);[61] and thorax and abdomen variation ranged from 4-10 mm(lateral), 6-16 mm (longitudinal) and 8-12 mm (vertical). [62-64]

Van Herk [52] also published a similar but a slightly larger margin equation: $2.5 \Sigma + 0.7 \sigma$. It is not the goal of this study to verify the equations proposed by Stroom or Van Herk, because the margin should be determined by multiple factors, including treatment goals, tumor stages, tumor/normal tissue locations, immobilization technique, and confidence level. The margin formulas may then be used only for confirmation.

Note that the proposed CTV-to-PTV margins were obtained from the interfractional setup variation with the use of the immobilization techniques reported in this study. The overall CTV-to-PTV margin, including both setup uncertainties and internal organ displacement, should be fully investigated before determining PTV margin. In addition, IGRT minimizes the interfractional setup errors and the margin derived from this study should not be used if IGRT is available.

2.4 Conclusions

The setup variations in the lateral, longitudinal, and vertical directions were randomly distributed. Organ displacement should be taken into account in the PTV, especially for treatment of the lung. With Stroom's margin suggestion, the calculated global CTV-to-PTV margins, which include both interfractional setup error and

intrafractional organ motion, ranged from 4.2 to 8.2 mm (lateral), 5.0 mm to 12.0 mm (longitudinal), and 1.5 mm to 6.8 mm (vertical), for the HN, brain, prostate, abdomen and lung sites. The use of pre-treatment MVCT reduced the systematical setup error and showed that the tumor changed during the radiation course. Pre-treatment MVCT can be used to improve the accuracy of patient positioning.

CHAPTER 3

Image Guided Stereotactic Body Radiotherapy for Lung Tumors Using BodyLoc System with TomoTherapy

3.1 Introduction

Hypofractionated stereotactic body radiotherapy (SBRT) was reported to have a higher local control rate than conventional fractionated radiotherapy for medically inoperable non-small cell lung cancer.[65-68] Compared to the latter, it uses a higher dose per fraction to achieve a better tumor control rate. The requirements for SBRT generally include secured immobilization, accurate patient positioning, ablative dose fractionation, and minimum normal tissue exposure. However, high toxicity to the surrounding organs, such as the normal lung, spinal cord, esophagus, skin, and trachea, remains a challenge and a reduced safety margin and precise target localization are needed to improve dose delivery.

Consistent and reproducible immobilization devices are usually used in SBRT delivery. Rigid fixation devices (e.g., a vacuum pillow or vacuum sheet combined with a thermoplastic body cast) have been used to reduce daily setup uncertainties.[69, 70] For motion-controlled SBRT treatment systems of abdomen compression, the maximum inspiration breath-hold technique and respiratory gating have been used to minimize tumor motion.[56, 71-73] Recent developments in image-guided therapy, including four-dimensional computed tomography (4DCT), have been used to accurately delineate tumor boundaries and reduce the tumor margin.[36, 55, 74] Furthermore, a pre-treatment

cone-beam CT (CBCT) was recently described for daily use to verify the target position.[27, 28, 75, 76]

Helical TomoTherapy provides an innovative way to administer image-guided SBRT. It enables tumor localization with a CT setup, and allows treatment on the same machine with automatic adjustment of the patient position. The embedded anatomy registration tool provides real-time tumor/organ shift coordinates so the patient can be repositioned to match the planning CT's orientation and position. Furthermore, the included TomoTherapy megavoltage CT (MVCT) serves as a volumetric 3D imaging and registration tool that gives more detailed information regarding tumor shape and position. This 3D tool is distinct from the 2D tools described in other studies, such as portal film and implanted fiducial markers, which have been used for target localization.[69, 70, 77]

This study presents the clinical implementation of the MIDCO [TM] BodyLoc system (Whole Body Stereotactic Localizer; MIDCO; San Diego, CA) to reduce patient motion with a TomoTherapy treatment unit. Additionally, it reports the inter- and intrafractional setup variations that were observed during the course of stereotactic lung treatment.

3.2 MIDCO[TM] BodyLoc System

The BodyLoc system employs a unique imaging resolver, which consists of a pair of sine wave fiducials coupled with a linear fiducial enabling stereotactic localization in the Z dimension (or longitudinal direction. Note that the definition of X, Y, Z in the BodyLoc system is different from TomoTherapy). Because the two sinusoidal fiducials are out of phase by 90 degrees, the positioning of the three fiducials establishes a unique

Z coordinates for each CT slice in the transverse plane. Additional pairs of the linear fiducials give the position for anterior-posterior and left-right coordinates (Figure 3.1a). Each fiducial line is made of a non-ferromagnetic fiber optic material that has a high contrast on both radiographic and CT images. The BodyLoc system has a cross bar with x-axis and y-axis scales for target localization for its "Body" section localization (b). The "Head" section of the system employs a targeting box for localization (c). The system also has sets of QA fiducial markers at Z = 100 mm, 300 mm, 500 mm, 700 mm and 900 mm that are used to verify the accuracy of stereotactic coordinate determination in the Z-axis (d). The BodyLoc software uses a mathematical algorithm to calculate the 3D stereotactic coordinates that identify the target point.
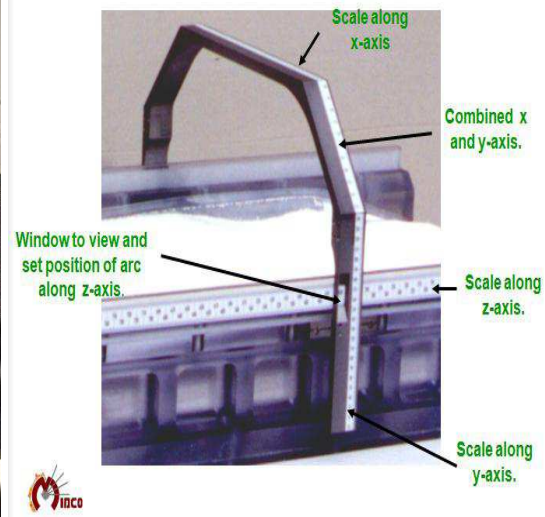
(a)   (b)
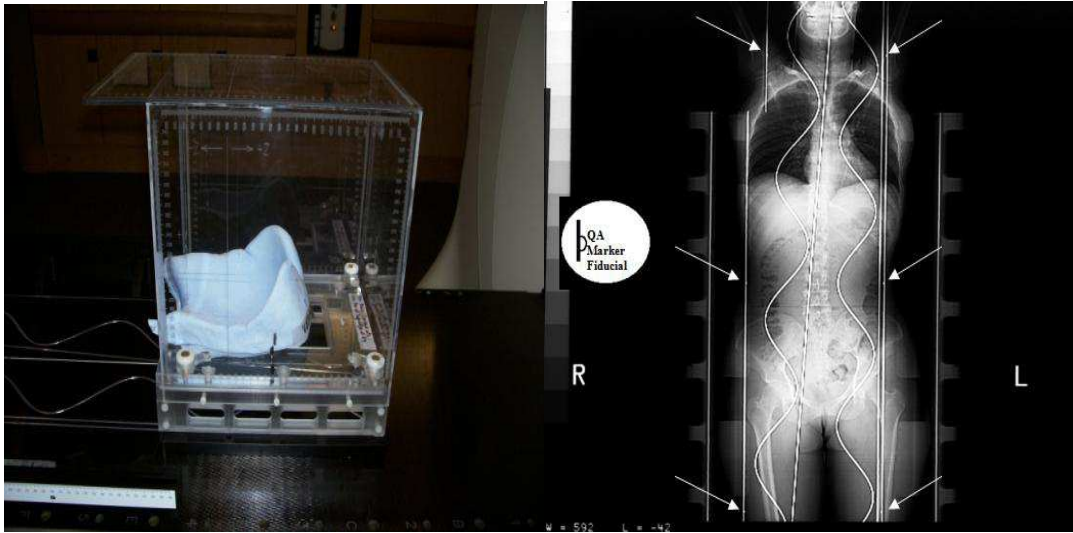
(c)   (d)

(e)
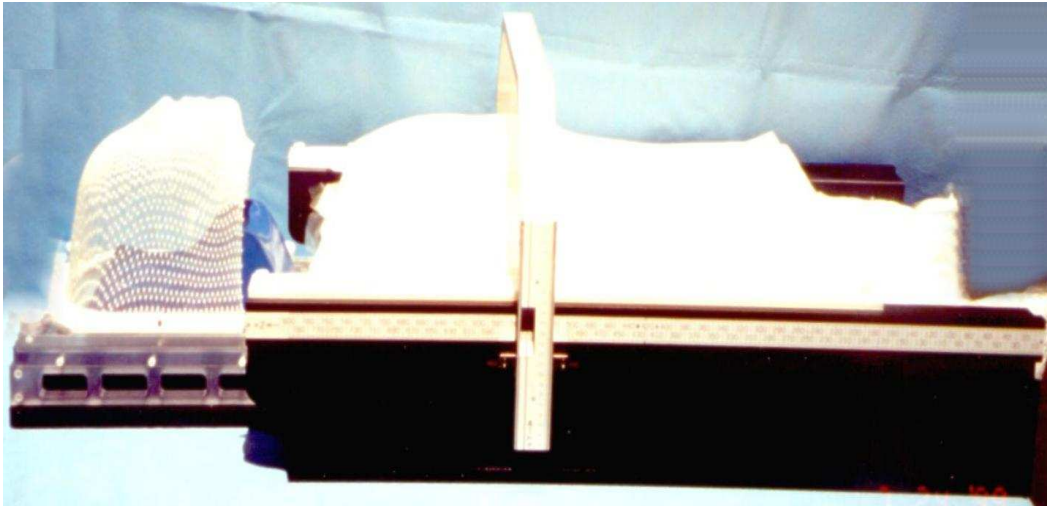
Figure 3.1 MIDCO ^{TM} BodyLoc system. (a) BodyLoc fiducial array; (b)BodyLoc

moveable indexer bar used for stereotactic target coordinate setup in the body section; (c)

BodyLoc target box for stereotactic target coordinate setup in the head section; (d) CT

scout image with QA markers in the base are placed at known Z locations; (e) overall

patient setup with head/brain immobilization and body immobilization with BodyLoc system.

3.3 Methods and Materials

3.3.1 Patients Selection, Simulation and Immobilization

Eight lung patients were treated with hypofractionated stereotactic body radiation therapy. The patients' ages ranged from 54 to 95 years old, with a mean age of 75.8. Four patients had lesions on their right sides and the other four had lesions on their left sides. No patients showed metastatic disease. The lesion boundaries were drawn based on PET-CT images. SBRT was given at doses ranging from 30 Gy to 60 Gy in 3–5 fractions.

The BodyLoc system was used as the base plate for patient immobilization during both the CT simulation and treatment. It was attached to the CT scanner couch with an index bar. Patients were supine on the BodyLoc system with their both arms facing upward and attached to a wing board. A thermoplastic body mask combined with the posterior SecureVac^{TM} from Bionix (100×70) was utilized to cover the patient's chest and abdomen. Patients were coached to use shallow breaths during creation of the thermoplastic body mask. Simulation images were acquired on a Picker/ PQ5000 single slice CT simulator. All patients underwent a free breathing CT scan while active breathing control was not performed during the scanning procedure. Serial CT scanning was performed with a slice thickness of 2.0 mm and an index of 2.0 mm.

Treatment planning was performed with a TomoTherapy treatment system. The optimization goal in common practice is to achieve 98% of the Gross Tumor Volume (GTV) receiving 100% prescribed dose. The normal lung volume was the total lung

volume subtracting the PTV volume, and the dose constraint was that 20% of the total normal lung volume received less than 18 Gy. A patient-specific margin was determined for each GTV. An intensity modulation factor of 2.0-2.5 and a pitch of 0.287 were chosen for most cases; however, for large tumors, an intensity modulation of 2 was chosen to reduce treatment time.

The TomoTherapy delivery machine was calibrated for a dose rate of 899 mu/min. Large doses or treatment times were divided into two sessions due to delivery time limitations. All patients in this study underwent a pre-treatment MVCT scan prior to beam delivery. A fine slice thickness (2 mm slice thickness with a pitch of 1) was chosen for all patients. MVCT images were acquired and fused with the planning KVCT using mutual information algorithms that focused on both soft tissue and bony structure. Patients were repositioned according to the shift coordinates, and the final position was reviewed and approved by the physician before beam delivery.

Using the BodyLoc software, 3D coordinates for localization were calculated before treatment. The BodyLoc's coordinate rulers were used in the initial setup by matching the setup lasers with the BodyLoc's indexers. In addition, BodyLoc localizer was used for cross comparison with the MVCT for patient positioning. Patient's target isocenter position was verified using the image fusion between pre-treatment MVCT and planning KVCT. If there was no setup error, there should be little discrepancy between the BodyLoc localization and MVCT fusion.

Due to the time limitation in dose delivery from TomoTherapy unit, for the prescribed doses used in the SBRT, the prescribed dose per fraction needed to be divided into 2-3 sessions in treatment delivery. For the first few treatments, verification MVCT

were repeated before each of the 2-3 session to investigate target motion during the treatment (i.e., intrafractional error). The deviation between the daily pre-treatment MVCT and the planning KVCT showed the interfractional errors. From the preliminary study, it was found that the intrafractional error was small and the use of the BodyLoc arc indexer bar alone without verification MVCT between two sessions was adequate.

3.3.2 Interfractional and Intrafractional Setup Uncertainties

Stereotactic coordinates were calculated for each patient using the MIDCO BodyLoc stereotactic software and was used for the patient setup. MVCT was performed to visualize the target position. The first MVCT scan was taken for patient daily setup and the second MVCT scan was performed to verify the target position after the first treatment session and before the second treatment session. Interfractional and intrafractional setup uncertainties were defined the same as in the Chapter 2. In short, the interfractional is the setup error between daily treatments over the whole course of radiation therapy. Intrafractional uncertainties were defined as the shift between the KVCT scan and the pre-treatment MVCT scan after the first treatment session, but before the second treatment session on a single treatment day.

The data collected for analysis included tumor volumes, target location, disease stage, and patient age, sex, and weight. In total, 224 recorded daily shifts from eight patients were collected and the inter- and intrafractional setup variations were analyzed.

3.3.3 Verification of System Mechanical Accuracy

An acrylic hexagonal shaped phantom called the HexaPhant® was developed to verify the system mechanical accuracy on TomoTherapy unit. The HexaPhant was designed with a film cassette holder that has six brass pins and accommodates an 85 mm x 85 mm piece of film. An ion chamber holder can be positioned in place of the film cassette. The HexaPhant has two test probes that have 8 mm MR compatible gelatin balls and two probes that contain five 2 mm tungsten balls spaced 3 mm apart that are radiologically identifiable. The HexaPhant can be mounted to the BodyLoc frame so that the film cassette or ion chamber can be oriented in either the sagittal or coronal plane. The location of the center pin within the film cassette is designed to coincide with the stereotactic target coordinate of a 5 mm cylindrical irradiated volume. MD-55 Radiochromic film was then loaded into the BodyLoc film cassette and punctured with the six pins. The film was irradiated with the treatment plan. The Delivery Quality Assurance (DQA) module of the TomoTherapy Planning system was used to analyze the dose profiles on the exposed film.

3.4 Results and Discussion

3.4.1 Hexaphant Accuracy Test

Figure 3.2 illustrated the setup of the HexaPhant for the accuracy test. Film was inserted in the cassette in both sagittal and coronal planes. By comparing the centers of the calculated dose profiles and the measured dose profiles from the film based HAT results, the coincidence of the planned and delivered center of the irradiated target

volume was verified. HAT profile analysis results on the TomoTherapy treatment unit are shown in Figure 3.3 for sagittal and the coronal dose profiles.
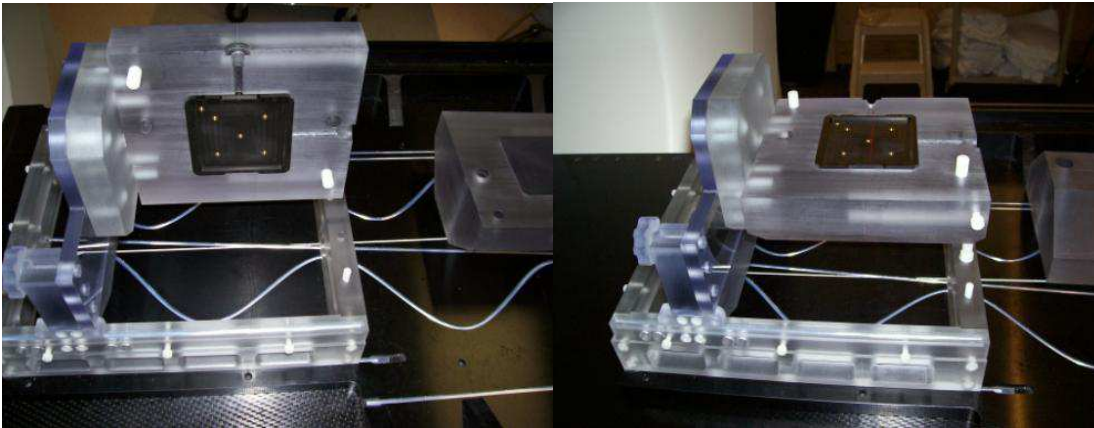
Figure 3.2 HexaPhant setup with film cassette oriented in sagittal and coronal planes for positioning accuracy test.

Coronal X   Sagittal Z   Sagittal Y
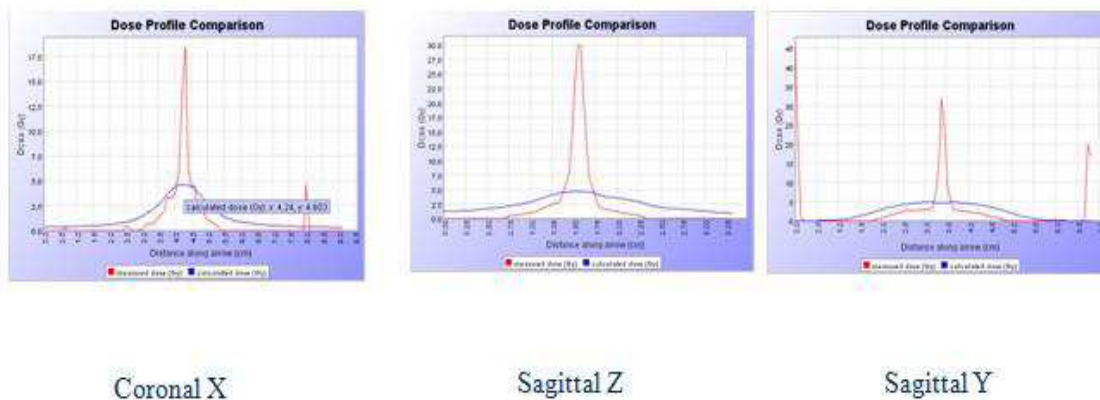
Figure 3.3 Resultant profiles from the HAT. The measured dose profile is shown in red and calculated dose profile in blue. The location of the center pin within the film cassette is designed to coincide with the stereotactic target coordinate of a 5 mm cylindrical irradiated volume. X, left–right (lateral); Y, superior-inferior (longitudinal); and Z, anterior-posterior (vertical).

HAT profile analysis in the sagittal plane showed that the discrepancy between the two centers along the longitudinal (Y) direction was approximately 0.3 mm and the discrepancy along the vertical (Z) direction was approximately 0.2 mm. The results in the coronal plane showed that the discrepancy between the two centers along the lateral (X) direction was approximately 0.5 mm. The overall system accuracy was found by calculating the vector sum of the X, Y and Z displacements (see Table 3.1): These data analysis demonstrated that the total discrepancy from the calculated radiation isocenter to the measured radiation isocenter was approximately 0.6 mm. This value fell well within the 2 mm tolerance that is recommended in the ACR Guidelines. This value is comparable to other stereotactic machines such as the Leskell Gamma Knife, with typical discrepancies between two centers along X, Y, and Z directions of approximately 0.25 mm.[78]

Table 3.1 Hexaphant Accuracy Test (HAT) - System Delivery Accuracy

	Calculated Position	Measured Position	Displacement
X-direction	42.5 mm	43.0 mm	0.5 ± 0.1 mm
Y-direction	15.4 mm	15.7 mm	0.3 ± 0.1 mm
Z- direction	34.1 mm	34.3 mm	0.2 ± 0.1 mm
Total Displacement			0.6 ± 0.2 mm

3.4.2 Inter- and Intrafractional Setup Uncertainties

Patient treatment parameters were summarized in Table 3.2. Total dose ranged from 30 Gy to 60 Gy with 3-5 treatment fractions. Daily treatment times ranged from 24 min to 45 min with two or three deliveries per fraction. Stereotactic coordinates were calculated for each patient using the MIDCO BodyLoc stereotactic software. These

coordinates were used for patient setup. MVCT was performed to visualize the target position. The first MVCT scan was used for the daily setup of the patient and the second MVCT scan was performed to verify the target position after the first, but before the second treatment delivery during the same day.
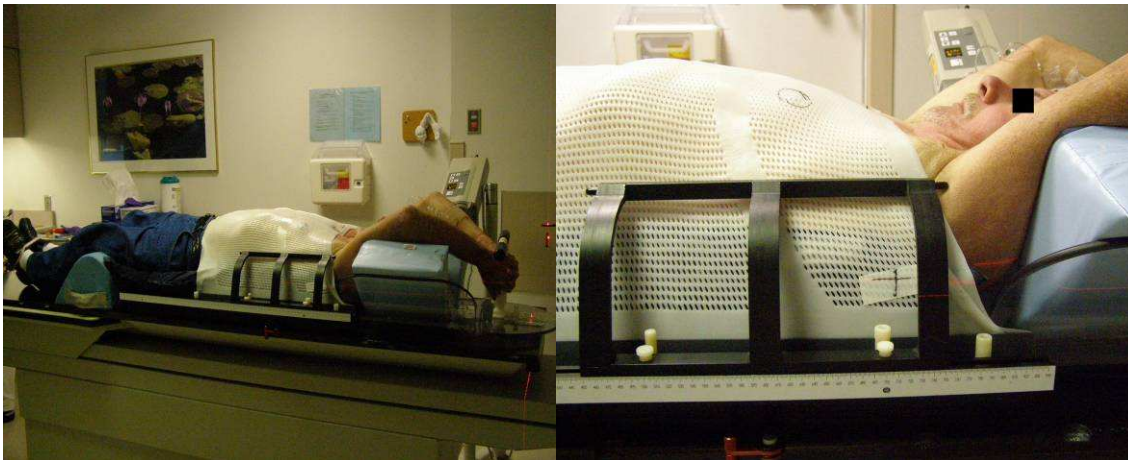
(a)   (b)

(c)

Figure 3.4 SBRT lung patient CT simulation setup with MIDCO BodyLoc system. (a) BodyLoc and thermoplastic body mask combined with posterior VacLoc immobilization

device was used for patient setup. (b) Side movable indexer bar fiducial provides the vertical coordinates for the patient setup. (c) Setup of SBRT treatment on the TomoTherapy machine for lung cancer treatment.

Table 3.2   Summary of patient disease location, stages and treatment parameters. Field width 1.1 cm, modulation factor of 2.5 and pitch 0.287 was set for all patients SBRT treatment planning. 98% of PTV volume was planned to get prescription dose. Fine dose calculation grid was used for all IMRT plans. Secure Vac ^{TM} from Bionix was used for all patient immobilization.

Patient ID	Target Location	Disease Stage	Total dose, Gy	No. of treatment fractions	Daily treatment duration, min	No. of session per fraction
1	RUL	T2N0M0	45	3	45	3
2	RUL	T1N0M0	40	4	20	2
3	RLL	T1N0M0	40	4	40	2
4	LUL	T4N0M0	30	3	34	2
5	LLL	T1N0M0	60	3	32	2
6	RML	T1N0M0	60	3	24	2
7	LUL	T1N0M0	50	5	42	2
8	LUL	T2N0M0	60	3	33	2

Table 3.3   Means, standard deviations, and maximum shifts from inter- and intrafractional setup uncertainties with BodyLoc immobilization for SBRT patients.

	Interfractional uncertainties, mm			Intrafractional uncertainties, mm		
	mean	SD	Max shifts	mean	SD	Max shifts
x	-1.1	2.8	5.5	0.1	0.7	1.3
y	-2.5	8.7	13.5	-0.3	2	3.8
z	4.1	2.6	8.2	0.5	1.1	2.9
roll	-0.3	0.7	1.6	0.1	0.2	0.4

x, left–right (lateral); y, superior-inferior (longitudinal); z, anterior-posterior (vertical). A two tailed t test was performed to compare the values obtained during the first and second scans for each of the 3D translational shifts and rotational movement. p values were less than 0.01 for all variables.

The means and standard deviations of inter- and intrafractional uncertainties calculated from the accumulated data points are summarized in Table 3.3. The interfractional lateral, longitudinal, and vertical setup uncertainties were -1.1 ±2.8 mm, -2.5 ±8.7 mm, and 4.1 ±2.6 mm, respectively. The mean rotational variation was -0.3° ±0.7°. The intrafractional lateral, longitudinal, and vertical organ motion variations were 0.1 ±0.7 mm, -0.3 ±2.0 mm, and 0.5 ±1.1 mm, respectively. The mean rotational variation was 0.1° ±0.2°. Student t tests comparing the first scan and second scan in terms of translational and rotational movements were performed and were statistically significant, with $p < 0.01$, for all directions.

In a comparison along the three directions (lateral, longitudinal, and vertical), the maximum shifts were found to be in the longitudinal direction for both the first and second scans, with a 13.5 mm shift in the first scan and a 3.8 mm shift in the second scan. The intrafractional organ motion was within ±2 mm in all translational directions.

(a)

(b)

(c)

(d)
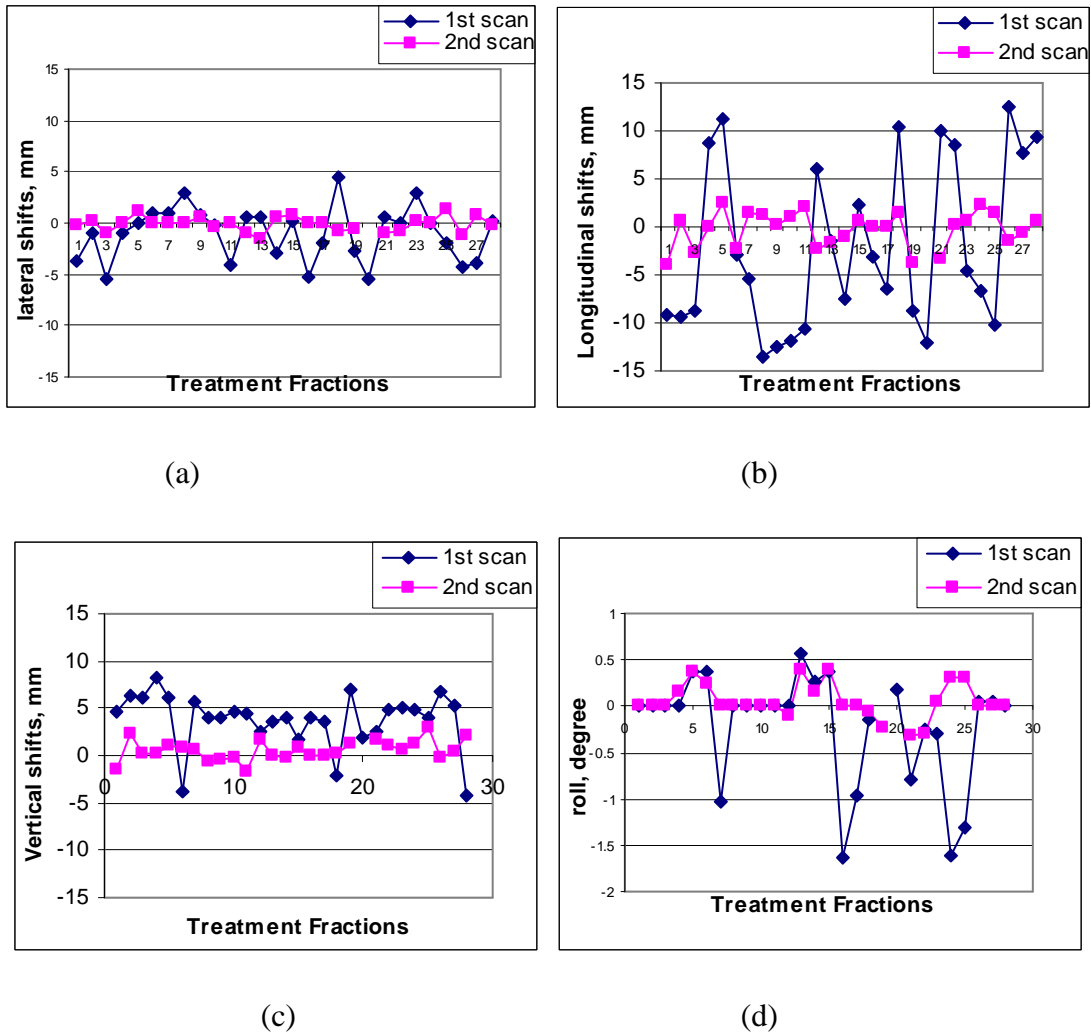
Figure 3.5 Comparison of inter- and intrafractional setup variations for eight patients. All patients' data were included in the figure. (Patient 1: fraction #1 to #3; patient 2: #4 to #7; patient 3: #8 to #11; Patient 4: #12 to #14; patient 5: #15 to #17; patient 6: #18 to #20; patient 7: #21 to #25; patient 8: #26 to #28.)
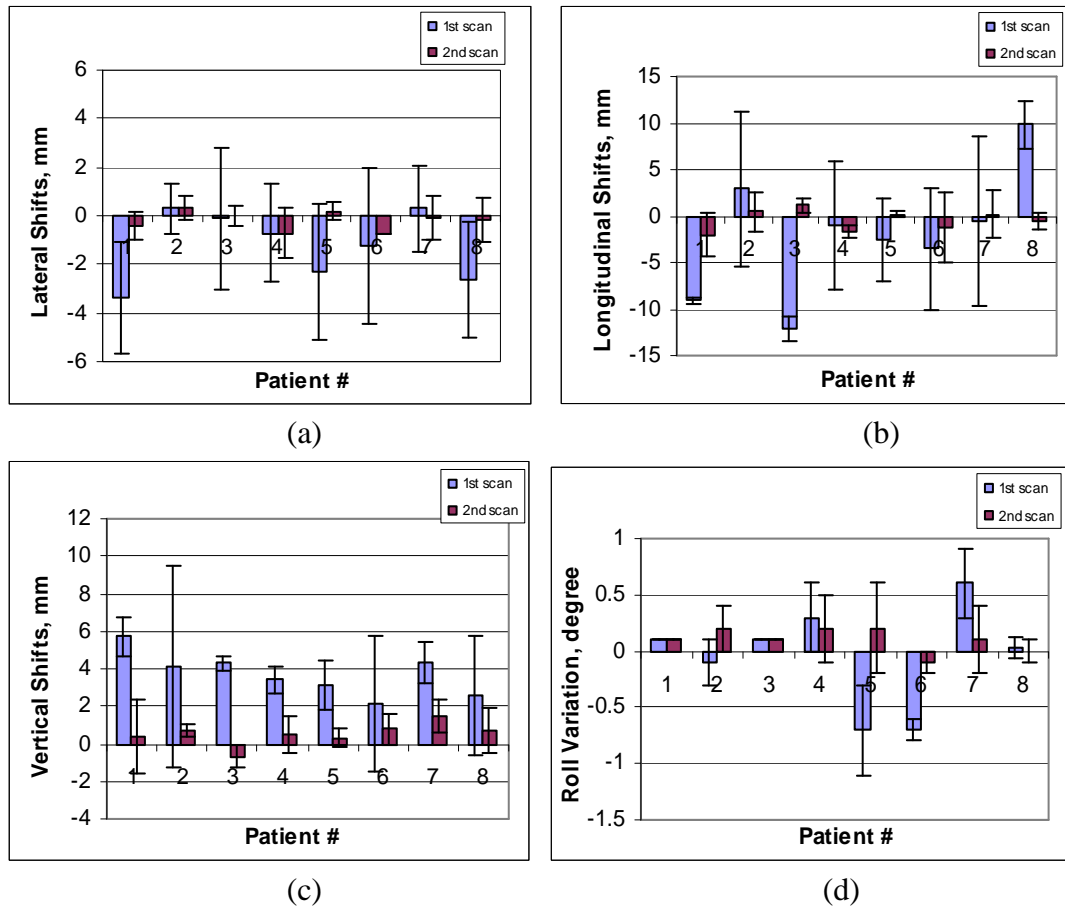
Figure 3.6   Comparison of the averages and standard deviations of inter- and intrafractional setup uncertainties. Panel (a), (b), (c) are the setup variations in the lateral, longitudinal and vertical directions, respectively; and (d) roll variation.

Figure 3.5 shows the setup shift (first scan) variation and organ motion (second scan) for each treatment for eight patients. Comparison of average setup uncertainties and their standard deviations for inter- and intrafractions for each patient are shown in Figure 3.6.

The comparison of 3D displacement for those with and without the BodyLoc is shown in Figure 3.7, and the comparison of organ motion observed with and without use of BodyLoc stereotactic devices is summarized in Table 3.4.

Table 3.4 Comparison of Intrafractional uncertainties with and without BodyLoc thermoplastic body mask immobilization. Total of 13 patients (eight SBRT patients and five conventional fractionation IMRT patients) were included in this study. All patients were treated with TomoTherapy machine.

	Mean ± SD mm				Max shifts mm				Mean 3D* mm
	x	y	z	roll	x	y	z	roll	
With BodyLoc	-0.1±0.7	-0.3±2.0	0.5±1.1	0.1±0.2	1.3	3.8	2.9	0.4	1.7
Without BodyLoc	1.2±1.4	-0.9±2.3	0.3±0.7	0.2±0.4	2.9	5.1	3.3	0.6	3.5

* Mean 3D vector was calculated according to $\sqrt{\Delta x^2 + \Delta y^2 + \Delta z^2}$, where Δx, Δy, and Δz represents the shifts between planning CT and MVCT in the left–right (x), superior-inferior (y), and anterior-posterior (z) directions, respectively.

The data suggest that suppression of internal organ motion was improved by the use of BodyLoc immobilization devices. With the BodyLoc system, the mean 3D displacement vector was 1.7 mm, down from 3.5mm, and the means and standard deviations of intrafractional lateral, longitudinal, and vertical organ motions were -0.1 ±0.7 mm, -0.3 ±2.0 mm, and 0.5 ±1.1 mm, respectively. The difference between the two testing groups of using and not using BodyLoc was statistically significant (p=0.001), according to the t test.

Pearson's correlation coefficients between patient characteristics, including age, weight, sex, treatment time, GTV volume, and both setup error and organ motion were tested and the results are summarized in Table 3.5. The correlation tests showed that

there were no significant correlations existed ($p > 0.1$ for all the tests) among these factors.

Table 3.5   Pearson's correlation coefficients between SDs of random displacement and patient variables including age, weight, sex, treatment time, and GTV volume.

| | 1st scan | | | | | 2nd scan | | | | |
	age	weight	sex	treatment time	GTV volume	age	weight	sex	treatment time	GTV volume
sd X	-0.18	-0.45	-0.43	0.06	-0.11	-0.13	-0.01	0.06	0.34	0.15
sd Y	0.53	-0.62	-0.40	-0.71	-0.26	0.07	-0.25	0.07	-0.34	-0.15
sd Z	0.51	-0.18	0.02	-0.68	-0.47	-0.38	0.05	0.18	0.27	-0.18
sd roll	0.53	-0.45	-0.64	-0.77	-0.40	0.51	-0.30	-0.67	-0.42	-0.22

No significant correlation among these variables ($p > 0.1$ for all tests) was observed. The two-tailed probability values were not shown.
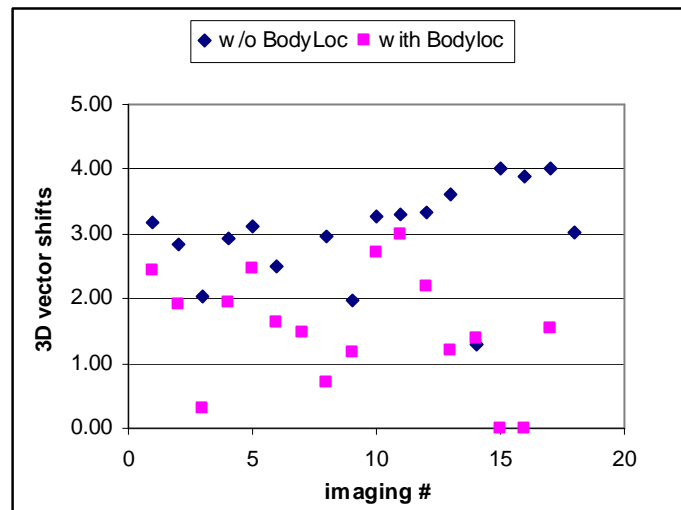
Figure 3.7   Intrafractional organ motion comparison for patients with and without BodyLoc immobilization devices.

Accurate target positioning with proper patient immobilization is essential for external beam radiation, especially for hypofractionated SBRT. However, accurate and reproducible patient setup is difficult to achieve due to respiratory motion and other factors that might affect accuracy, e.g., elongated treatment and verification times, and the use of a skin tattoo versus stereotactic coordinates as a reference in the setup method.

Several studies have reported on the accuracy of stereotactic frames and patient setup uncertainties. Grills et al reported on the stereotactic body radiotherapy setup error with CBCT image guidance.[27] Their calculated population margins were 9–13 mm pre-correction, 1–2 mm post-correction, and 2–4 mm post-treatment (including setup error and internal drift). Hodge et al. [65] reported the average positional shifts and the associated standard deviations for each of 9 patients treated by TomoTherapy SBRT with definition of tumor volume by 4DCT envelope. The maximum lateral, longitudinal, and vertical shifts in their studies were 6.79±2.9 mm, -9.89±2.6 mm and -9.19±3.8 mm, respectively. Another group utilized a commercially available stereotactic whole body immobilization system (BodyFIX, Medical Intelligence, Schwabmuenchen, Germany) for a study of 36 patients treated by hypofractionated stereotactic body radiation therapy. They reported median and mean magnitude vectors of target isocenter displacement of 4.9 mm and 5.7 ±3.7 mm, respectively.[69]

Similarly, relatively large interfractional setup uncertainties for patient setup (first scan) were observed in this study. The largest motion was in the longitudinal direction compared to vertical and lateral movements. These larger uncertainties might result from the image acquisition and registration technique or random patient setup error that was observed on a daily basis. Because of the slow gantry rotation of the MVCT scanner on

TomoTherapy (5 s per image slice), the motion pattern of the target is encoded into the pretreatment MVCT-scan, which yields a motion-encoded treatment target.[79,80] However, since the GTV/CTV volumes were obtained from a conventional CT simulator (scan time ~4 s), the stereotactic coordinates obtained from this study were related to the breathing phase for a given CT slice during the simulation CT scan. The differences in respiratory phases between the planning CT and MVCT scans may be a major factor that contributes to setup uncertainty.

The daily beam-on-time of the patient involved in this study ranged from 24 min to 45 min, and the average treatment time in this study, including patient setup, pretreatment imaging, and beam delivery, was about 60 min. The interval time between localization and the repeated second MVCT scan was usually between 15 and 30 min. In contrast to Purdie [81], who reported a significant intrafractional tumor position difference when the time interval exceeded 34 min, no obvious correlation was observed between elongated treatment time and intrafraction motion in this study.

The organ motion caused by respiratory motion was greatly reduced by the use of BodyLoc immobilization devices. The thermoplastic body mask combined with the SecureVac[TM] covered patients from the thoracic wall to the abdomen. Patients were told to take shallow breaths during the mask making process. If heavy breathing was observed, more abdominal pressure would be added. This was an efficient approach for motion suppression. The data in this study are similar to those reported by Negoro,[70] who utilized an abdomen suppression method. Briefly, they reported that application of the abdominal pressure method greatly reduced tumor movement from a range of 8–20 mm to a range of 2–11 mm.

Shortening treatment time is beneficial to SBRT patients since they undergo prolonged treatments with both arms up. The present study showed that the intrafractional error was small and the use of the BodyLoc arc indexer bar alone without verification MVCT between two sessions was adequate. Verification scan and reposition usually took 5-10 minutes during the setup, while the calculation of BodyLoc coordinates usually took 2-3 minutes before the treatment setup. Skipping the verification MVCT resulted in a decrease of the treatment duration by 5-10 minutes.

The limitation of the present study is the relatively small patient number analyzed. Eight patients were included in this study; data from a larger number of patients are needed for further statistical analyses. In addition, data obtained from patients with various tumor locations may improve our understanding of the degree to which tumor location is related to target shifts.

3.5 Conclusions

The preliminary data for lung SBRT using MIDCO [TM] BodyLoc whole body stereotactic localizer combining with TomoTherapy megavoltage CT image guidance was reported and analyzed in this chapter. Although the rigid immobilization devices were used for all SBRT patients, large setup deviation was still observed. Such deviations posed a requirement of a real-time tumor tracking system (i.e., pre-treatment MVCT scanning) to locate and treat target precisely.

CHAPTER 4

Implementation of 4DCT and Deformable Registration

for Accurate Moving Target Delineation

4.1 Introduction: Motion Artifacts with 3DCT Imaging and Related Problems

Lung cancer is the leading cause of cancer death in the industrial countries. In 2006, there were over 170,000 cases of new lung cancer arising in US, and among them, over 50,000 patients had unresectable tumors. Radiation therapy is one of the few curative options for these patients. With traditional radiation dose and fractionation, radiation therapy achieves local control in less than 20% of the patients. Though clinical study suggested that a higher curative rate is possible if the treatment dose is further increased,[82-87] the safety margin around the tumor sets the limit for further dose escalation. Since the tumor motion is related with respiration, this safety margin is specifically enlarged to account for the uncertainty in target delineation and treatment delivery. To better target the tumor with minimal normal tissue exposure in the radiation field, accurate tumor delineation is one of the critical issues in lung cancer treatment.

It has been recognized that severe artifacts can be introduced if organ motion is present during CT data acquisition.[88-94] The major cause of these artifacts is the dynamic interaction between trans-axial image acquisition and the asynchronous motion of tumor and normal organs. A commonly observed artifact is the distortion of the dome of the liver at the lung–diaphragm interface (Figure 4.1). In other instances, a lesion may be imaged as two distinct parts, and the axial slices may be shuffled out of order. Such

artifacts incorrectly characterize the geometric shape and extent of the organ. Figure 4.2 illustrates the severe distortions of the sphere when a rounded object was moving on a sliding table during a CT scan. Different artifacts are obtained when CT data acquisition starts at different positions of the motion cycle. The variations in artifacts shown in Figure 4.2 illustrate the unpredictability of motion artifacts in CT scanning if information about the motion during data acquisition is not available.
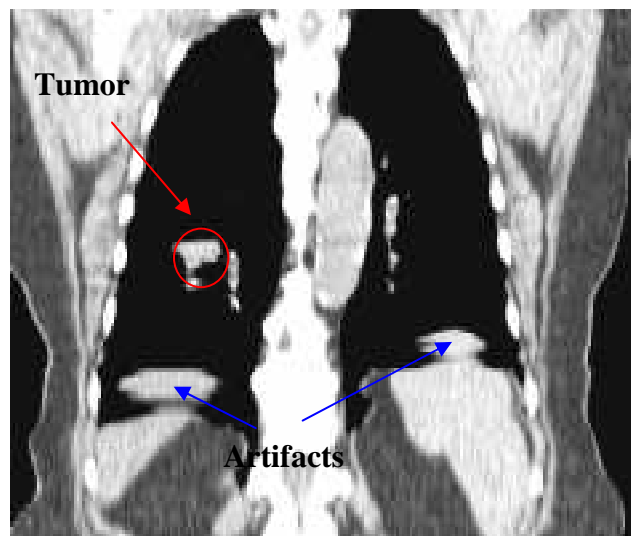
Figure 4.1 Distortion of the dome of the liver at the lung–diaphragm interface observed from a patient CT scan caused from respiratory motion. A fast imaging technique, such as single slice CT results in image deformation artifacts.
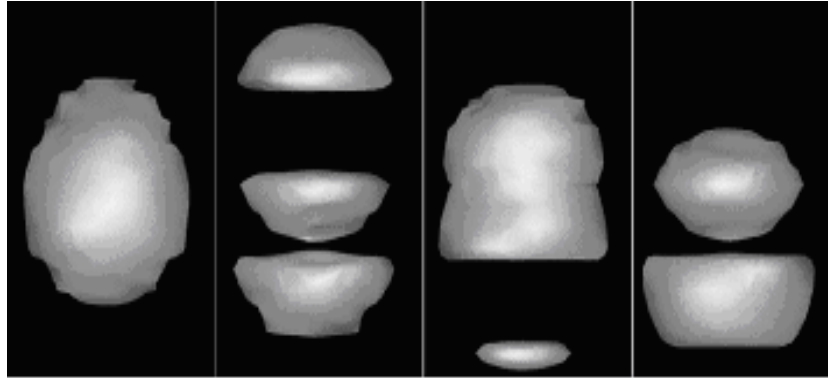
Figure 4.2 Different artifacts obtained by periodically moving a rounded subject on a sliding table during standard axial CT scanning.

Respiratory motion artifacts can be minimized if scanning is performed during breath hold,[95] or with thermoplastic immobilization to suppress breathing, e.g., the stereotactic body immobilization method studied in Chapter 3. Under these circumstances, however, the patients have to endure a prolonged respiratory holding, which is difficult for the lung disease patients, and more importantly, no information on organ motion will be obtained. Without explicitly considering the pattern and degree of organ motion, it is very hard to precisely deliver radiotherapy. To overcome this, some investigators chose the approach of using the scans acquired during breath hold at tidal exhale and tidal inhale to estimate the maximum extent of tumor motion.[56, 72, 96, 97]

Organ motion could also be assessed by visualization during fluoroscopy at the time of conventional simulation. This approach provides information useful in designing an aperture that geometrically covers the target, by assuming that the target position changes with inhale and exhale, and these two extreme conditions could provide the target motion envelope which generally covers the target motion trajectory (Figure 4.3). However, fluoroscopic data are limited to 2D projections, while respiratory motion in

general is three-dimensional. Furthermore, without the aid of implanted radio-opaque fiducial markers, soft tissue and lung tumors cannot easily be visualized through fluoroscopy, and hence it is hard to obtain the complete volumetric information of organ motion.

(a)   (b)
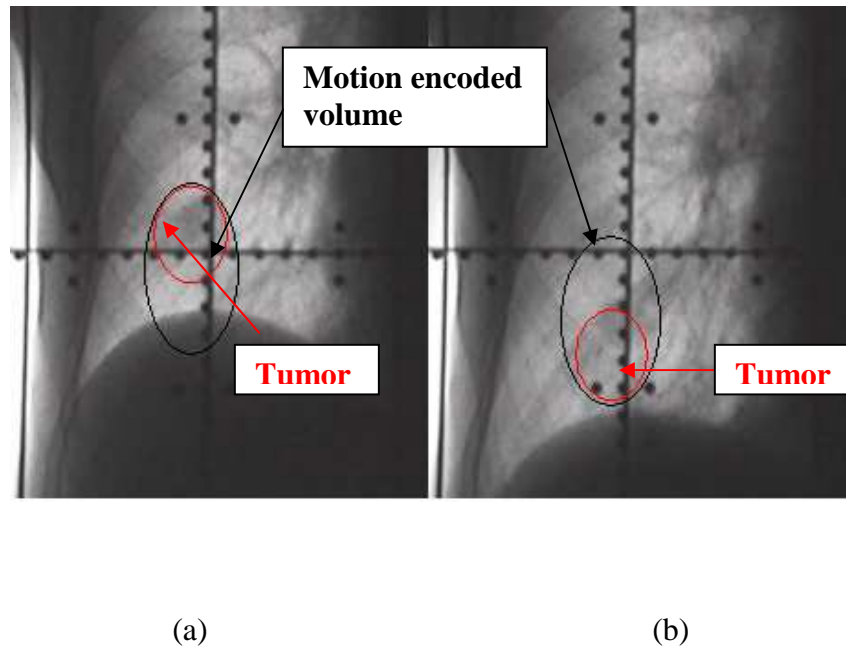
Figure 4.3 Tumor movement during (a) exhale, and (b) inhale phase. A motion encoded volume was derived by assuming the target position changes with inhale and exhale, and these two extreme conditions could provide the target motion envelope which generally covers the target motion trajectory.

4.2 Image Acquisition with 4DCT and Delineation of Targets

Four dimensional radiation therapy (4DRT) is a recent advance in radiation therapy to investigate the motion caused by respiratory movement. The 4th dimension beyond the 3D space is *time*, in which patient motion and anatomy changes could be

recorded in time frames. 4DCT scans have been utilized as one of the clinically valuable tools for assessment of respiration and tumor movement.[98, 99] A respiration-correlated 4DCT is usually performed with 16-slice CT scanner (Lightspeed 16, GE Medical System, Waukesha, WI) and the real-time position management system (RPM, Varian Medical system, Palo Alto, CA) under uncoached quiet respiration. The imaging protocol consists of obtaining both the free breathing CT scans and the respiratory phase related CT scans.

The 4DCT process is briefly described as the following: Patients are scanned in supine position with both arms up. Two kinds of scans are acquired to complete the imaging process. One is a regular CT scan, with no respiratory information included. The other is the cine mode scan, with couch stationary during scanning. During the cine mode scanning, a commercial respiratory monitoring system (e.g., RPM system from Varian) was placed on the top of patient's abdomen near the umbilicus, to acquire the respiratory pattern with the CT scan. There are 12-16 scans acquired at the first couch position. In each scan, images acquired are over several respiratory cycles, typically every 4 or 5 seconds. Then radiation is turned off before the couch is moved to adjacent position to start another scan. This process is automatically repeated until the entire thorax is scanned (about 16 to 19 couch positions). It's recommended that total of about 2500 images per patient should be obtained.

After the image acquisition is done, a resorting software (e.g., Advantage 4D: GE Healthcare) is used to resort and recombine all the obtained CT images according to each respiratory phase recorded by RPM system. The resorting software assigns a specific respiratory phase to each reconstructed image, and then sorts all the images into 10

phases, with phase T0 and phase T5 corresponding to end of inhale (EOI) and end of exhale (EOE) during a respiratory cycle (Figure 4.4), respectively. These separated sets of respiratory phase encoded as 3DCT images present the anatomy data during each phase of respiratory cycle. The sorted 3DCT images along with the free breathing CT are then transferred to a treatment planning system, such as Pinnacle ADAC treatment planning system (Phillips Medical Systems, Milpitas, CA), for contouring and volume study.
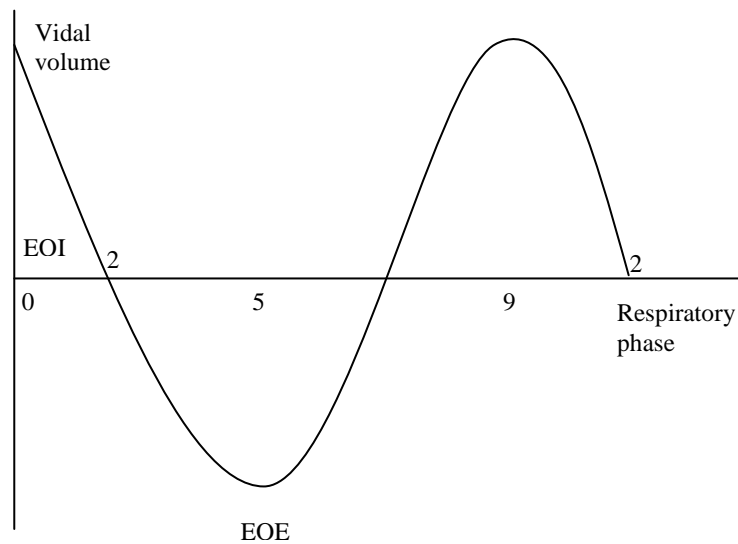
Figure 4.4. Illustration of phase and lung volume changes during a respiratory cycle. Total of 9 phases were defined for different phases, with phase T0 and phase T5 corresponding to end of inhale (EOI) and end of exhale (EOE) during a respiratory cycle. T stands for time variable.

Ideally, to accurately obtain the tumor position, the contour on each image sets from phase T0 to phase T9 is preferred. However, this would be very time consuming and is not practical in clinic practice. A simpler approach to reduce the workload is to

perform an automatic contouring based on the deformable registration from one phase to others in 4DCT image sets. For example, in clinic physicians could draw contours on phase T0, T5 and on the free breathing CT images, and then perform auto-contouring for all other phases to obtain contours on all the 10 phase image sets.[100-103]

The purpose of auto-contouring is to obtain the target delineation from one respiratory phase to the corresponding points in other phases. The first step of auto-contouring was to calculate the displacement vector between two phases. The source phase was chosen so that it has the smallest variation during different respiratory cycle. Here T0 was chosen as the source phase or the moving object for deformable registration. The displacement vector was calculated in several iterations from coarser voxel scales to finer scales until convergence was reached. The second step was to apply the transformation vector to the manual contour on the source CT and to obtain the deformed contour on the target CT set. The ROI masks on T0 images (or source images), Ms, were transformed onto the other images according to

$$M_t(\vec{x}) = M_s(\vec{x} + \vec{u}(\vec{x})) \tag{4.1}$$

Where M_t is the target ROI masks on T1-T9 phases; M_s is the source image ROI marks on T0 phase.

A Pinnacle script is used to generate binary masks of reference ROIs. The reference ROI masks were transformed onto target images using displacement maps from deformable image registration. As a consequence, target images were segmented automatically. A custom-developed algorithm is used to convert the ROI masks into Pinnacle's ROI file format so that the ROIs can be displayed in Pinnacle.

Figure 4.5 shows the flowchart of the deformable registration and obtaining automatic segmentation delineation (or auto-contouring).

```
┌─────────┐      ┌──────────────┐           ┌──────────────┐
│  4DCT   │ ───▷ │ Contouring on│  ◁────▷   │ Target image │
│         │      │     T0       │           │ with phase i │
└─────────┘      └──────────────┘           └──────────────┘
                           │
                    ┌──────────────┐
                    │  Deformable  │
                    │ registration │
                    └──────────────┘
                           │
                    ┌──────────────┐
                    │Deformed contours on│
                    │   phases i   │
                    └──────────────┘
                           │
                    ┌──────────────┐
                    │ITV from 10 phases│
                    └──────────────┘
                           │
                    ┌──────────────┐
                    │ PTV₄D for treatment│
                    │   planning   │
                    └──────────────┘
```
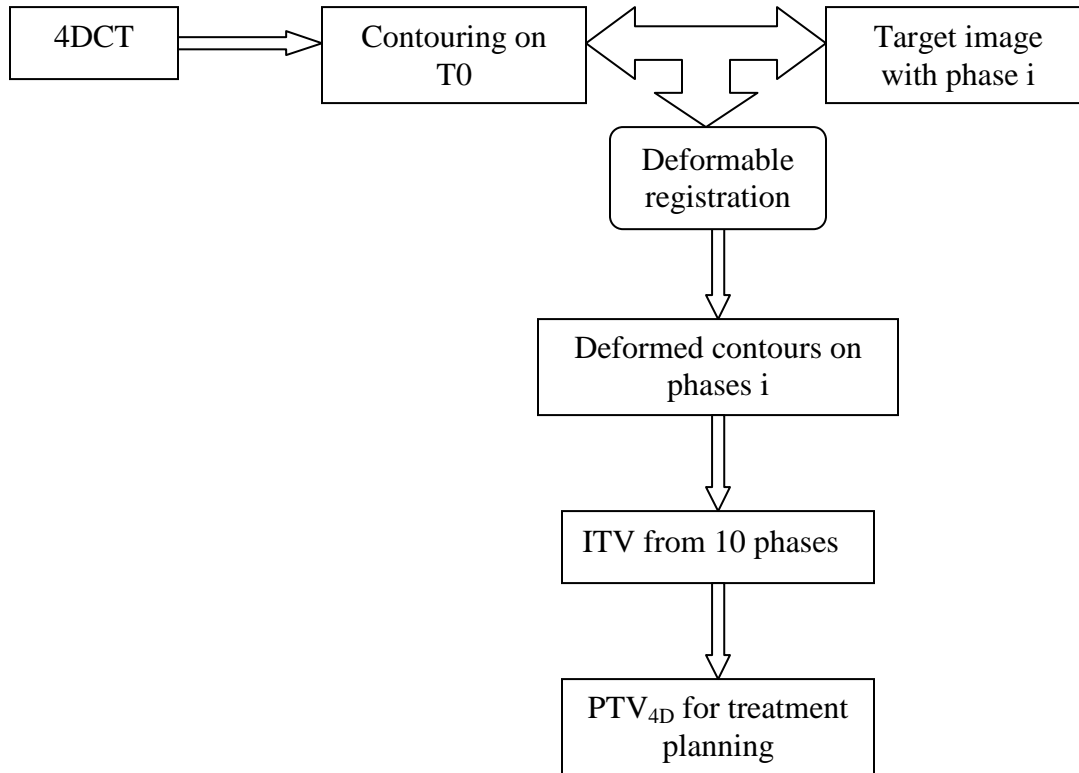
Figure 4.5 Flowchart of obtaining automatic segmentation delineation from 4DCT.

4.3 Rigid and Deformable Registration

It has been one of the most important research areas in radiation therapy to develop an effective image registration algorithm. Clinically, because of the extensive use of multi-modality imaging and the emergence of new imaging techniques and methods, the need is ever increasing for a robust image registration algorithm to compare/fuse images representing the same structures obtained under different conditions or on different modalities. Depending on the mathematical nature of the transformation,

image registration is divided into two categories: rigid registration and deformable registration. In rigid transformations, it is assumed that the geometry of the object is identical in the two input images and no distortion occurs in the image acquisition process. A rigid transformation consists of six degrees of freedom: three displacement parameters and three rotational parameters. On the other hand, deformable registration, which is the key part in obtaining target delineation from 4DCT (Figure 4.5), is more complicated and entails the modeling of voxel dependent distortion.

Computer-based rigid image registration has gained widespread popularity in the last decade and is mostly used in routine clinical practice. In this approach, the matching of the two input images is formulated into an optimization problem and the best registration of the two images is obtained by iteratively comparing various possible matches until no better registration can be found. The search for the optimal match of the two input images is usually performed by a scoring function constructed based on some physical considerations.

Deformable registration methods have been studied recently by several authors, and a variety of deformable registration tools have been developed. [104-107] These tools match each point in one of the 3DCT scans with the corresponding point in the 3DCT scan of another breathing phase. Popular deformable registration algorithms include empirical B-spline deformation model, demons registration model, optical flow, or finite element methods (FEM).

Bharath et al.[108] and Brock et al.[109] proposed a finite element model, in which images are described as blocks of elastic materials on which forces apply. In this approach, the parameters that control the behavior of the elastic material and are

responsible for the conversion of forces into local deformations of the elastic material are Young's elastic modulus and Poisson's ratio. However, the drawback of this method is that values of the elasticity and density constant for various tissues are not readily available and have to be found by a trial and error procedure. This method also relies on using complicated software to generate an FEM mesh and masks of the involved structures.

Schreibmann and Xing have proposed a general narrow-band approach for deformable registration. [110] Depending on the problem, modeling of individual voxel movement can also be made using either B-splines,[100] thin plate splines,[111] optical flow algorithms,[112] or fluid flow algorithms.[113] Spline interpolation is a relatively simple approach and the free-form registration is stable and accurate for dealing with IGRT image registration problems. An improvement to this method can be achieved by using a spline model with the smoothness of the deformation field assured by the interpolation between grids of fixed control points. A simple method along this line is to deduce the spline coefficients from a set of user-defined control points in warping and registration of MR volumes, as was done by Fei et al.[114] and Lian et al.[115] in warping and registration of MRI volumes. Coselmon et al.[101] used a similar technique to study the accuracy of mutual-information-based CT registration of the lung at exhale and inhale respiratory states.

4.4 Deformable Registration Algorithm

Although 4DCT contains a complete description of the patient geometry for each breathing phase, it does not describe how the tissues move and deform from phase to

phase. In this section, CT deformable registration between different breathing phases was performed to estimate the motion trajectory for tumor in the lung, as well as the necessary transformation vector for the automatic contouring function.

Deformable registration was performed with ITK (Insight ToolKit), an open source software toolkit for medical image registration and segmentation (http://www.itk.org). The motion between breathing phases was modeled using B-splines registration tool to smoothly encode the amount of deformation at each point in the image. Optimization is performed by minimizing the mean squared difference in intensity, and is implemented with a multi-resolution, gradient descent procedure. The total function of the registration problem could be formulated as the following:

$$f[\vec{u}] = \int_{\vec{x}\in R^3}[S(\vec{x}+\vec{u}(\vec{x})) - T(\vec{x})]^2\,dx + \alpha\int_{\vec{x}\in R^3}g(|\nabla u_i(\vec{x}))d\vec{x}| \qquad (4.2)$$

Where, $f[\vec{u}]$ is the optimization function, $S[\vec{u}]$ is the source image and $T[\vec{u}]$ is the target image. $\vec{u}(\vec{x})$ is the displacement field representing the transformations from the source image to the target image. $\vec{u}=(u_x,u_y,u_z)$ and $\vec{x}=(x,y,z)$ are three-dimensional vectors in the Cartesian coordinate system. α is a free parameter and R^3 is the 3D image domain. $g(|\nabla u_i(\vec{x}))d\vec{x}|$ is the intensity gradient function of displacement fields. The first term is the summation of the squared differences in intensity error caused by the intensity (in CT numbers) discrepancies between the target image and the source image. The second term is related to some predefined requirements or assumptions for the transformation. For example, penalties could be reinforced if the smoothness of the displacement field $\vec{u}(\vec{x})$ is not satisfied.

Deformation vector is given by B-spline functions:

$$\vec{u}(x,y,z) = \sum_{i,j,k \in \aleph} \vec{c}_{i,j,k} B^3_{i,j,k}(x/\delta_x - x_i) \times B^3_{i,j,k}(y/\delta_y - y_j) \times B^3_{i,j,k}(z/\delta_z - z_k) \qquad (4.3)$$

Where $\delta_x, \delta_y, \delta_z$ is the B-spline grid size defined by the user, $\vec{c}_{i,j,k}$ is the vector

of coefficient at grid (i,j,k); and $B^3_{i,j,k}$ is third order B-spline basis function.

The basic steps of the multi-grid method are as follows: (1) convert the original

fine grid problem to multiple hierarchical coarser levels. (2) interpolate the solutions

from the coarsest level to the next finer level using tri-linear interpolation, and recycle the

results at the coarse level as the initial guess for the next level of iterations. (3) Repeat

step (2) until the finest level is reached. This process is efficient because the iterations at

the coarse grid levels are calculated fast and converge quickly. In addition, the smoothing

error appears to be higher in frequency and thus can be naturally fixed in the next finer

grid.

The software determines the 3D nonlinear deformation field required to register

the two volumes by sequentially stepping through the source volume on a 3D cubic

lattice and estimating at each node the displacement vector required to maximize the

correlation coefficient of image intensities in the neighborhood of the node. The

algorithm was applied iteratively in a multi-scale hierarchy on data at different

resolutions, beginning with very blurred data (using an isotropic Gaussian kernel with

full width at half maximum equal to 16 times the image resolution) so that gross features

drive the fit first. In this study, the initial image resolution of 64×64×34

(6.71875×6.71875×10mm^3) was chosen as the beginning stage of the deformable

registration. The resulting deformation field was used as a starting point for the next scale

step, where less blurred data (image blurring and lattice grid spacing were reduced after

each iteration) allow smaller details to be included, thus refining the fit. The deformation lattice spacing on each consecutive registration step was 10, 5, and 2.5 mm, respectively.

The deformable registration algorithm relies on the assumption that the pixels representing the same homologous points on an object which has the same intensity on both the fixed and moving images to be registered. It then selects the number of bins to represent the histograms and the number of points where the histogram is to be matched. The registration filter used in the algorithm has two parameters: the number of iterations to be performed and the standard deviation of the Gaussian smoothing kernel to be applied to the image prior to calculating gradients. The registration algorithm is triggered by updating the filter, or increased voxel resolution scales. The final filter output is the computed deformation field.

4.5 Procedure of Performing Deformable Registration

Deformable registration with the ITK toolkits requires the CT image property conversion. That is, it is needed to convert the DICOM format of 4DCT image to .mha format in order to use the ITK toolkits. After the deformable registration was performed, the .mha format of the deformed CT images was then converted to .nii format for the free medical image software MRIcro to read. In this study, Matlab 7.0 was used to perform these image property conversions.

The overall deformable registration procedure is summarized in Figure 4.6.

69

```
┌─────────────────────────────────────────────────────────────┐
│ Convert all .dicom images to .mha format with 'Dicomtomha3D.m'│
└─────────────────────────────────────────────────────────────┘
```

Read parameter file containing image sizes, type of images (fixed or moving), B-spline grid spacing and grid resolution

Update grid resolution, smoothing parameters, etc.

Load B-spline registration tool

Computed deformation field

Good ?

No

yes

Final deformation field with .mha format

Convert .mha format to .nii format

Image analysis with MRIcro

Figure 4.6 Flowchart of performing deformable registration with ITK toolkits.

4.6 Registration Results Assessment

To assess the registration results, the deformable registration was performed between the extreme breathing phases that correspond to the largest deformations, (i.e.,

end of inhale T0 and end of exhale T5). This allows the largest registration error to be checked.

Figure 4.7 (a) shows the overlaid image of EOI (T0) to EOE (T5) before deformable registration, and (b) the overlaid image of the final registered T0-to-T5 images and T5 at a specific slice after registration. The CT image of T5 was in grey color for both image fusion, T0 was in red in (a), and the registered T0-to-T5 images were in red in (b). The visual inspection of the overlaid images showed a good performance of the B-spline registration algorithm. Using image fusion tool provided by MRIcro, deviations can be clearly distinguished from matched regions.

(a)　　　　　　　　　　(b)
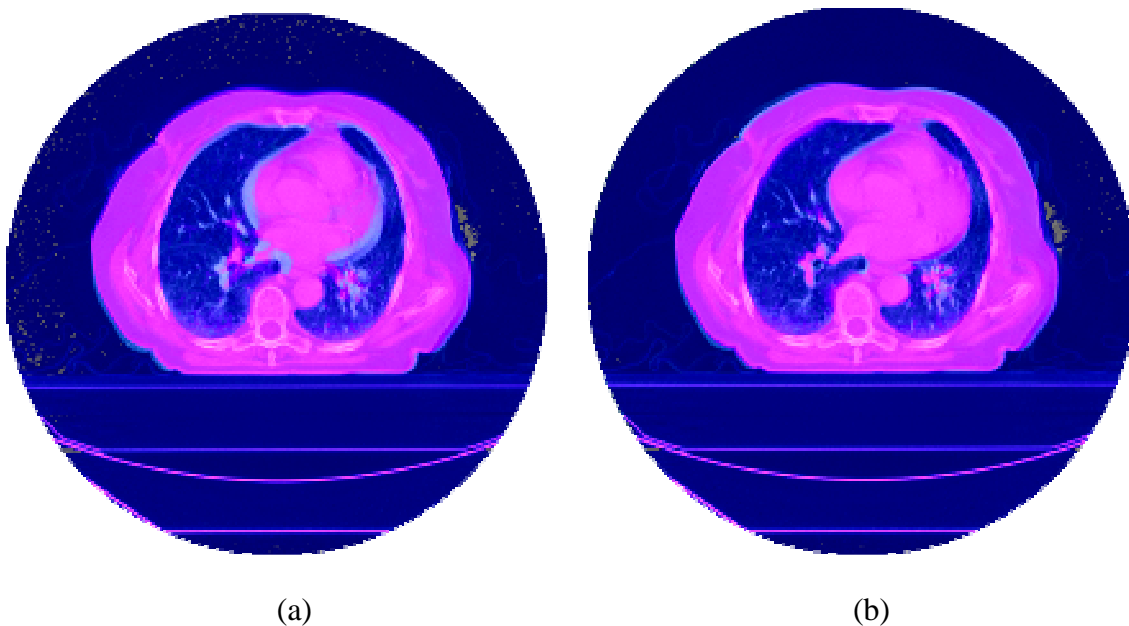
Figure 4.7 Image fusion from phase T0 (EOI) to phase T5 (EOE) with image resolution of 256×256×136. (a) Before B-spline deformable registration, T5 in grey color and T0 in red color; and (b) after deformable registration, T5 in grey color and registered T0-to-T5 images in red color.

The registration results of three different image resolution are shown in Figure 4.8: (a) 256×256×136; (b) 128×128×136; and (c) 128×128×68. Visually, there was a larger error if the resolution is coarser than 128×128×136. If the resolution is finer than 256×256×136, there was no further improvement of registration results, but CPU running time was doubled. In this study, the resolution of 256×256×136 was chosen for all deformable registration.

It should be pointed out that, the B-spline deformable registration for the automated delineation can work well on images with higher contrast, e.g., thoracic CT images.[116, 117] However, some artifacts such as zigzag or irregularly shaped contours can still exit in low-contrast regions because of image noise and artifacts. Therefore contour smoothing and manual editing could be necessary as the next step of this study.

4.7 Conclusions

4DCT could give a more accurate description on respiratory related tumor motion. The extreme breathing phases that correspond to the largest deformations could be matched with a reasonable accuracy with the B-spline deformable registration with ITK toolkit and the developed in-house custom software. The automatic contouring tool could significantly save time for the target delineation from all phases of the respiratory cycle. The image resolution used during the deformable registration (i.e., 256×256×136) could bring the registration accuracy to the clinical image resolution level.

(a)

(b)

(c)
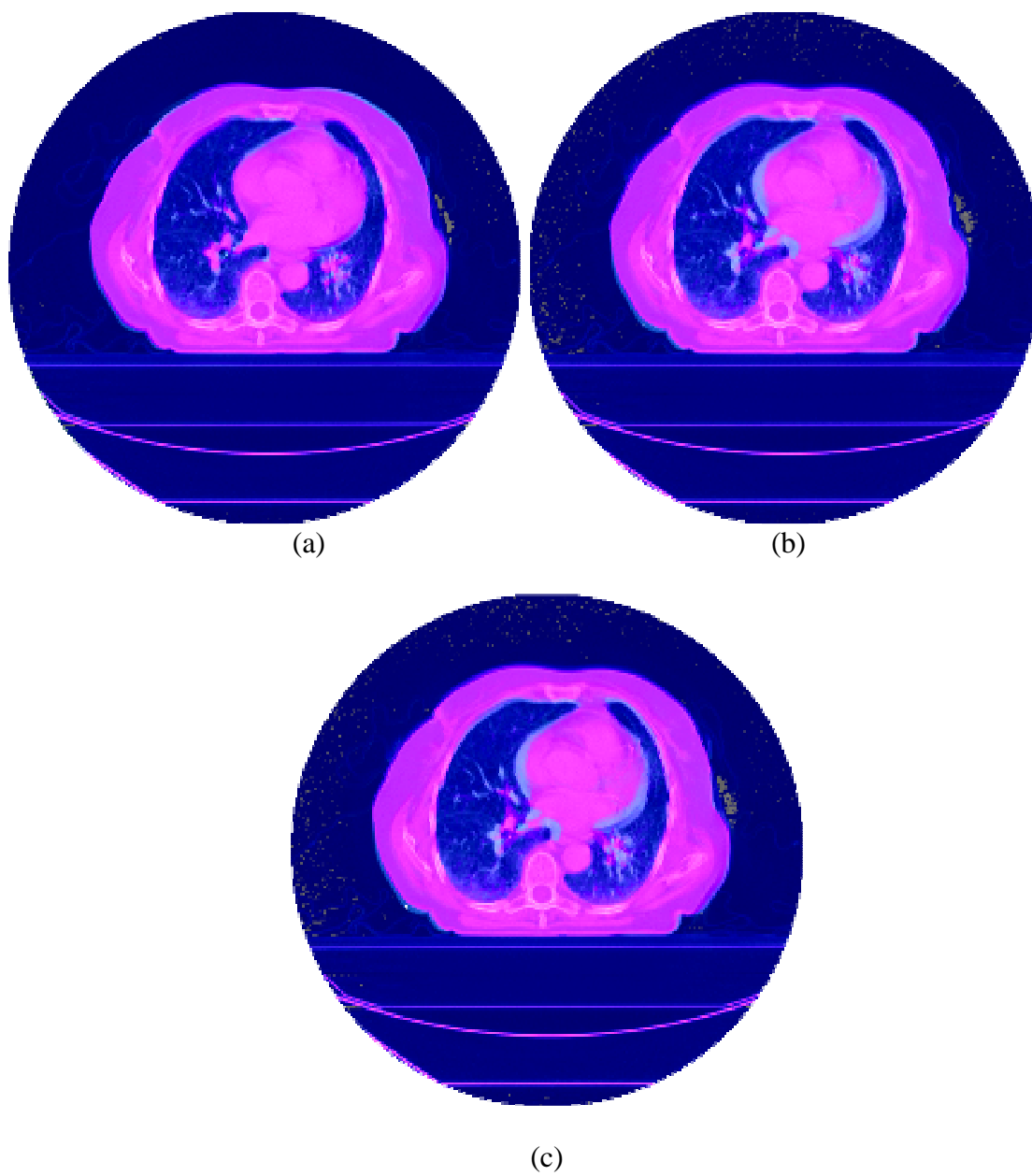
Figure 4.8 Image fusion results from phase T0 (EOI) to phase T5 (EOE) with different resolutions: (a) 256×256×136; (b) 128×128×136; and (c) 128×128×68. T5 in grey color and registered T0-to-T5 images in red color.

CHAPTER 5

Evaluation of Lung Tumor Mobility and

Dosimetric Effects with 4DCT

5.1 Methods and Materials

5.1.1 Target Volume Definition

Target volumes were defined as follows in this study: gross tumor volume (GTV) represents the primary lesion that can be visualized on the CT images; clinical target volume (CTV) is the GTV volume plus certain margin to account for possible positive disease. When the treatment target is constantly moving caused by involuntary or voluntary organ motion, an adequate margin must be applied to the CTV to compensate this motion. This forms the planning target volume (PTV) upon which the treatment plan is based. Internal target volume (ITV) is defined as the tumor volume includes the motion trajectory of the gross target volume (GTV) and possible invasive lesions from each phase of the 4DCT image scans.

In this Chapter, the tumor volumes were defined both in 3D and 4D. The 3D volumes were taken from the free breathing helical CT scanner, and 4D volumes were drawn based on 4DCT scanner with different respiratory phases (e.g., phase 0 to phase 9). In detail, the 3D target volumes were derived from CTV plus global margin which include internal organ motion and setup margins. The GTV to CTV margin was set to be

8.0 mm to account for possible positive disease.[118] The margin for the PTV_{3D} was defined as another 7.4 mm in lateral (x), 12 mm in longitudinal (y), and 6.8 mm in vertical (z) direction from the previous clinical experience of lung patient treatment shown in Table 2.4. In total, the GTV to PTV margin is 15.4 mm, 20 mm, and 14.8 mm for lateral, longitudinal and vertical direction.

The internal target volume ITV from 4DCT encompassed all 10 phase GTV volumes with the margin of 8.0 mm to account for possible positive disease. Planning target volume PTV_{4D} was the ITV plus the setup margin (SM). From the previous study for lung patients in Table 2.4, SM was chosen 5.5 mm, 6.6 mm, and 5.1 mm for lateral (x), longitudinal (y), and vertical (z) respectively. The final GTV to PTV margin is 13.5 mm, 14.6 mm and 13.1 mm for lateral, longitudinal and vertical directions.

The definition of tumor volume is summarized in Table 5.1.

Table 5.1 Tumor volume definition for both 3DCT and 4DCT in the study

	GTV_{3D}	From free breathing CT scan
3D tumor volume	CTV_{3D}	GTV_{3D} + 8.0 mm
	PTV_{3D}	CTV_{3D} + (7. 4 mm, 12 mm, 6.8 mm in x, y, z respectively)
	GTV_{4D}	From phase 0 to phase 9
4D tumor volume	ITV_{4D}	GTV_{4D} + 8.0 mm
	PTV_{4D}	ITV_{4D} + (5.5 mm, 6.6 mm, 5.1 mm in x, y, z respectively)

x, y and z stands for lateral, longitudinal, and vertical direction respectively.

5.1.2 Target Volume Analysis and Dosimetric Evaluation

Total of six patients were involved in the tumor mobility study with 4DCT images in this Chapter. Three patients had left lesion and the other three had right lesion in the

lung. Patients' characters such as disease stage, weight and ages were not included since this study only investigates the magnitude of tumor motion during different respiratory phase at this point. The GTV volumes were calculated for each patient from each phase of respiratory cycle. The GTV percent volume change relative to respiratory phase 2 was calculated. Phase 2 was chosen as a reference because it is in the middle of EOI (T0) and EOE (T5) and could be used to check the volume change from the extreme phases. The definition of respiratory phase was previously defined in Figure 4.4.

The motion of GTV mass center was used to assess the tumor motion during the ten respiratory phases. The coefficient of variation (standard deviation divided by average) of GTV was used to evaluate the percentage change of GTV volume during different respiratory phase. GTV centroid motion trajectories were investigated throughout respiratory cycle.

The tumor volumes including CTV_{3D}, PTV_{3D} and ITV_{4D}, PTV_{4D} from 3D and 4D were calculated and compared according to the tumor definition in previous section.

To compare the dosimetric results from with PTV_{3D} and PTV_{4D}, and ensure that PTV_{4D} could accurately provide sufficient tumor coverage and spare more normal tissue, two IMRT treatment plans were performed to investigate the dosimetric and biological effects. The 3D and 4D treatment plans were designed for each patient with different PTVs: PTV_{3D} and PTV_{4D}. Both of the plans were designed at the free-breathing CT image. The dose was prescribed so that 95% of PTV volume would receive the full prescription dose. Five equal spaced beam angles (0°, 72°, 144°, 216°, 288°) with energy 18X were chosen for both plans. The total dose was 66 Gy with 30 fractions.

The following dosimetric parameters were used to check the dose coverage for tumor volume from both PTV_{3D} and PTV_{4D}: V_{100}, V_{98} and V_{95} (the relative volume of PTV covered by 100%, 98% and 95% isodose line to PTV volume). The maximum dose to target (D_{max}), minimum dose to target (D_{min}) and mean dose to target (D_{mean}) from these two plans were also compared. For normal tissue, i.e., ipsilateral lung, contralateral lung, heart and spinal cord, mean dose and maximum dose were compared.

Pinnacle ADAC treatment planning system (Phillips Medical Systems, Milpitas, CA) was a dedicated commercial treatment planning system in radiation therapy planning. The ADAC system was utilized to calculate the position of GTV mass center, tumor volume calculation, perform IMRT planning and dosimetric comparisons.

Student t test was performed to check if there were any significant differences between the 3D and 4D plans.

5.1.3 Lyman NTCP Model

The radiobiological effects of different planning parameters on normal tissue complication probability could be described with the Lyman NTCP model.[119] The Lyman NTCP model was initially proposed by Kallman et al.[120] and was modified by Zaider and Amols.[121] Kehwar and Sharma[122] and Kehwar[123] have further extended this model for the multiple components (MC) model and the linear quadratic (LQ) model. These extended forms, of the NTCP model for MC and LQ models, were fitted to the normal tissue tolerance doses reported by Emami et al.[124] at $TD_{5/5}$ (tumor dose that could cause 5% complication within 5 years) and $TD_{50/5}$ (tumor dose that could cause 50% complication within 5 years) for partial volumes of different normal tissues / organs.

The Lyman NTCP model assumes a sigmoid dose–response relationship with no threshold, and could be depicted as in Equation (5.1):

$$NTCP = \phi(t) = \frac{1}{\sqrt{2\pi}} \int_{-\infty}^{t} e^{-x^2/2} dx \qquad (5.1)$$

Where

$$t = \frac{D - TD_{50}(v)}{m \cdot TD_{50}(v)}$$

$TD_{50}(v)$ represents the tolerances doses associated with a 50% chance of complications for uniform partial normal tissue irradiation. $TD_{50}(v)$ is related to the whole organ ($v = 1$) tolerance through the power law relationship:

$$TD_{50}(v) = TD_{50}(1) \cdot v^{-n} \qquad (5.2)$$

$TD_{50}(1)$ represents the tolerance dose of the whole organ to irradiation, m characterizes the steepness of the dose– response at $TD_{50}(1)$, and n represents the volume effect, which relates the tolerance doses of uniform whole organ irradiation to uniform partial organ irradiation. When n is near 1, the volume effect is large and when it is near 0, the volume effect is small.

5.2 Results and Discussion

5.2.1 Target Volume Analysis

The comparison of GTV volumes from different respiratory phases on the 4DCT of six patients and results of GTV motion amplitudes for each patient over the whole respiratory cycle were summarized in Table 5.2. The average GTV volume ranged from

4.5±0.1 cc to 67.9±2.1 cc. The mean GTV volume was 26.4 cc from these six patients. The coefficient of variation (standard deviation divided by average) of GTV ranged from 2.4% to 4.8% with an average of 3.4% during a respiratory cycle. The 3D centroid motion peak-to-peak amplitude of the GTVs caused by respiration ranged from 3.0 mm to 10.4 mm with average of 5.8 mm and standard deviation of 2.5 mm. Patient #1 has largest mass center deviation and patient #5 has the smallest deviation.

Table 5.2 GTV volume study and GTV center motion during respiratory cycle for six patients.

Patient	Location	GTV volume, cc			GTV center motion, mm			
		average	SD	SD/avg (%)	x	y	z	3D
1	RUL	29.3	0.8	2.9	5.7	8.5	2.1	10.5
2	LLL	18.5	0.5	2.9	1.2	4.7	0.9	4.9
3	LUL	5.8	0.3	4.8	1.5	4.2	1.9	4.9
4	RLL	67.9	2.1	3.1	3.6	3.8	2.1	5.6
5	RUL	4.5	0.1	2.4	0.7	2.9	0.3	3.0
6	LLL	32.2	1.3	4.0	3.1	4.3	2.2	5.7
Mean		26.4	0.9	3.4	2.6	4.7	1.6	5.8
SD		23.4	0.7	0.9	1.9	1.9	0.8	2.5
Max		67.9	2.1	4.8	5.7	8.5	2.2	10.4
Min		4.5	0.1	2.4	0.7	2.9	0.3	3.0

Abbreviations: RUL = right upper lung; LLL = left lower lung, LUL = left upper lung, SD = standard deviation; x = lateral; y = longitudinal; z = vertical; 3D = three dimensional vector.

The mean GTV center motion from the 4D studies were 5.8 mm, which is similar to the 3D vector obtained from previous intrafractional organ motion study ($\sqrt{1.9^2 + 5.4^2 + 1.7^2} = 5.97$ mm, Table 2.4). This shows that the 4DCT data gave a relative accurate description about the real intrafractional organ motion.

The relative tumor volume changes (using phase 2 as reference) from patient #1 and patient #5 are given in Figure 5.1. It can be seen from the figure that, although the lung tidal volume is the maximum in phase 0 (EOI) and minimum in phase 5 (EOE), the tumor volume didn't follow the same changing pattern. Instead, the tumor volume reached maximum around phase 5 for patient #1 and around phase 6 for patient #5.
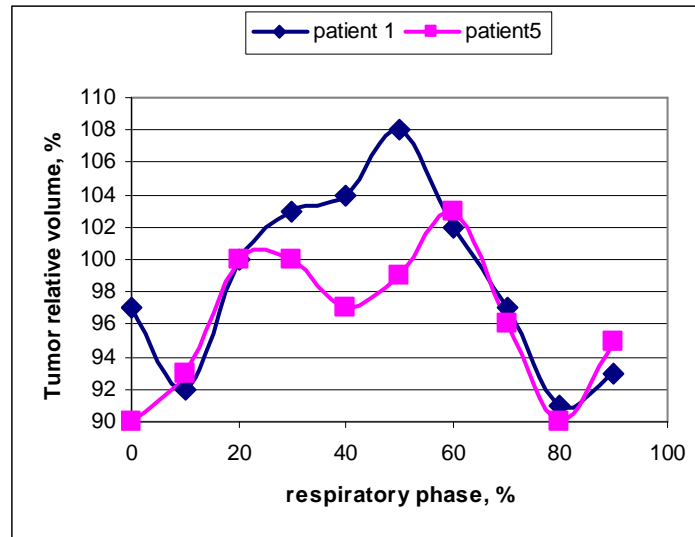
Figure 5.1 Volumetric variations of GTV volume over the respiratory cycle for patient #1 and patient #5. Respiratory phase 2 was used as reference to calculate the volume change.

The relative GTV centroid position trajectories in lateral, longitudinal and vertical directions (phase 2 as reference) from patient #1 and patient #5 are shown in Figure 5.2 (a) and (b).

(a)   (b)
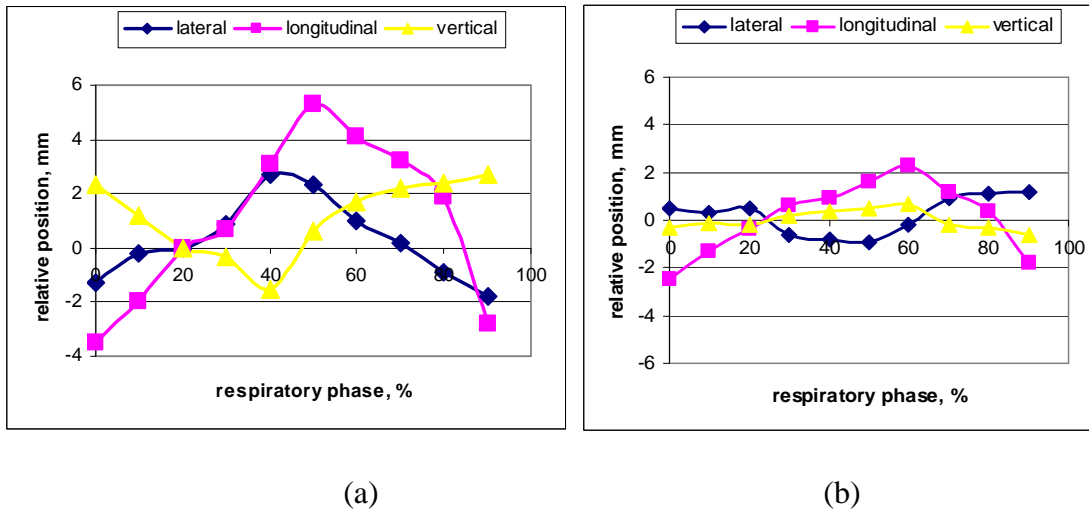
Figure 5.2 GTV volume centroid motion trajectories for patient #1(a) and patient #5 (b) throughout respiratory cycle in three dimensions.

Patient #1 showed a larger displacement in all the three directions compared to Patient #5. There was no similar motion pattern in the direction between these two patients, although the tumors were located in the similar position, i.e., RUL from these two patients. The relative position of each of the three directions was also independent in the lateral, longitudinal and vertical direction for both patients.

5.2.2 Comparison of Target Volumes from 3DCT and 4DCT

The tumor volumes including CTV_{3D}, PTV_{3D} and ITV_{4D}, PTV_{4D} were calculated and compared for each patient using the ADAC treatment planning system. The tumor volumes from 3D and 4D are summarized in Table 5.3. The average PTV volume in the 4D was 304.2 cc, and average PTV volume in 3D was 367.0 cc. The PTV_{4D} was 18.7% (range 11.2–26.8%) less than the 3D plans. Although the tumor was located in different position, the PTV_{4D} volumes were smaller than PTV_{3D} in all 6 patients.

The detailed axial view comparisons were performed to compare the PTV volume from 4D and 3D. The PTV$_{4D}$ was smaller than PTV$_{3D}$ in all three orthogonal planes for four of the chosen patients, but it exceeded PTV$_{3D}$ in some slices for the other two patients. The PTV$_{3D}$ encompassed the PTV$_{4D}$ in all three dimensions (e.g., patient # 1, #3, #4, and #5), indicating that conventional margins added to CTV in 3D plan exceeded those actually needed and resulted in unnecessary irradiation of normal tissues, especially for the liver and the normal lung. For patient # 2 (Figure 5.3), although the PTV$_{4D}$ was smaller than PTV$_{3D}$ (266.3 cc vs. 315.5 cc), there was a part of PTV$_{4D}$ not included in the posterior and lateral directions. This illustrated that the PTV$_{3D}$ not only included excess normal tissues but also might result in missing the target during certain phases of the breathing cycle for some cases.

Table 5.3 Target volume comparisons for six patients

Patient No.	CTV$_{3D}$, cc	ITV$_{4D}$, cc	PTV$_{3D}$, cc	PTV$_{4D}$, cc	PTV$_{4D}$/PTV$_{3D}$, %
1	65.3	198.2	352.6	263.2	74.6
2	48.6	132.5	315.5	266.3	84.4
3	38.2	129.4	223.5	175.3	78.4
4	113.5	335.6	587.1	521.4	88.8
5	26.2	89.6	267.2	195.7	73.2
6	78.4	296.4	456.2	403.2	88.4
mean	61.7	197.0	367.0	304.2	81.3
SD	31.5	99.4	134.0	133.0	6.8
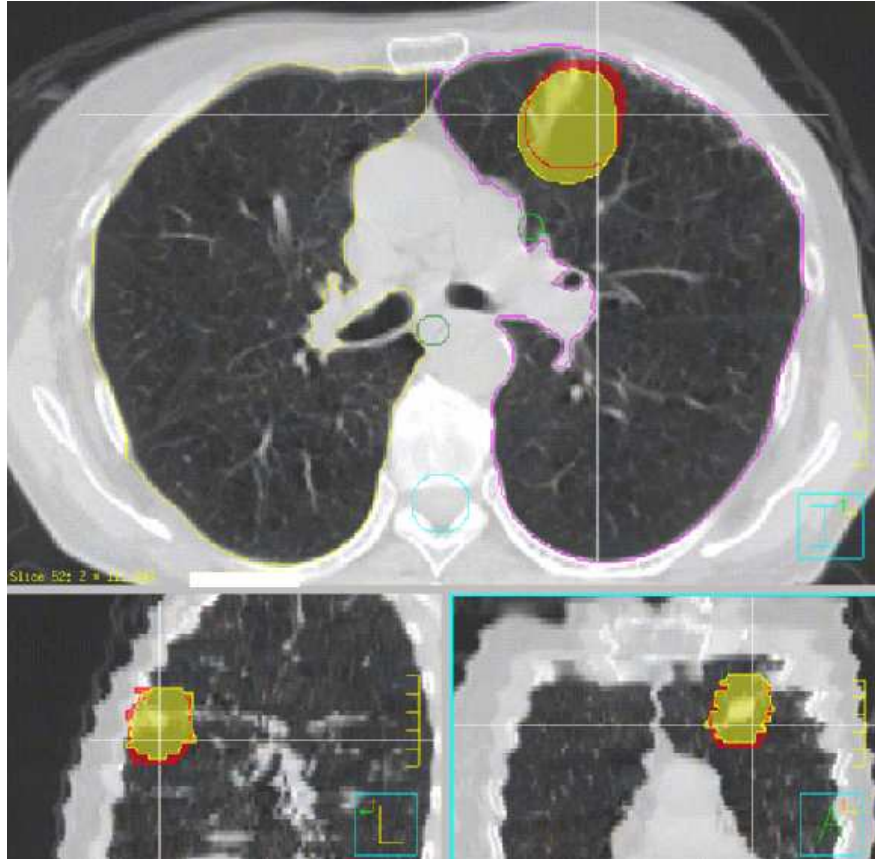
Figure 5.3 Comparison of PTV$_{3D}$ (red) and PTV$_{4D}$ (yellow). This figure illustrated that the volume of PTV$_{4D}$ was not covered by PTV$_{3D}$ in the posterior and right direction on the selected slice. Top: transverse views; Bottom-left: sagittal views; Bottom-right: coronal views.

5.2.3 Dosimetric Evaluation of Target Volumes

The parameters of the Lyman NTCP (Normal tissue complication probability) model for lung, heart and spinal cord, *TD$_{50}$*, *n*, and *m* are summarized in Table 5.4. These parameters were derived from the studies by Burman et al.[125]

Table 5.4 Normal tissue complication probability (NTCP) parameter values

Organ	TD_{50}, Gy	m	N	End point of complications
lung	24.5	0.18	0.87	Pneumonitis
heart	48	0.1	0.25	Pericarditis
Spinal cord	66.5	0.175	0.05	Myelitis Necrosis

TD_{50}: the tolerance of 50% complication; m: slope factor, steepness of the dose-response at TD_{50}; n: volume factor, volume-effect parameter.

4DCT images comprise patient-specific respiratory motion into treatment planning and could be used to ensure dose coverage of tumor during the breathing cycle. The results of the dosimetric evaluation of PTV coverage from 3D and 4D plans are shown in Table 5.5. Both 3D and 4D plans could get dose coverage above 90% of volume for V_{100}, V_{98} and V_{95}. Student t test were performed for both volume coverage and dose coverage and the results showed that there was no significant difference in PTV coverage and dose uniformity between these two plans (p>0.05).

Table 5.5 Dosimetric comparisons between 3D and 4D plans for six patients.

Item	PTV_{3D}	PTV_{4D}	p value
V_{100} , cc	275.64 ± 88.91	280.12 ± 72.63	> 0.05
V_{98} , cc	292.14 ± 75.32	293.52 ± 52.54	> 0.05
V_{95} , cc	337.19 ± 53.25	298.23 ± 66.65	> 0.05
Dmax (Gy)	72.25 ± 2.35	71.74 ± 3.54	> 0.05
Dmin (Gy)	62.58 ± 6.39	62.42 ± 3.52	> 0.05
Dmean (Gy)	68.40 ± 2.54	68.85 ± 3.62	> 0.05

V_{100}, V_{98} and V_{95}: the average volume of PTV covered by 100%, 98% and 95% isodose line from six patients; Dmax: maximum dose to target; Dmin: minimum dose to target; Dmean: mean dose to target. Student t test showed no significant difference between the 3D and 4D plans.

The ipsilateral lung was defined as the contoured ipsilateral lung volume minus the PTV. Table 5.6 summarizes the dosimetric comparison between 3D plan and 4D plan for all OARs in six patients. Figure 5.4 illustrates an example of the dose volume histogram (DVH) comparison for heart and ipsilateral lung between the two plans for patient #4. The 4D plan spared more ipsilateral lung and heart than 3D plan. The mean dose for ipsilateral lung and heart were reduced from 19.74 ± 4.21 Gy and 11.87 ± 3.35 Gy to 6.16 ± 3.26 Gy and 6.08 ± 1.28 Gy ($p<0.001$). There were no statistical significance for contralateral lung and heart between 3D and 4D plans. This is because these two OARs were relatively far away from the PTV and there is no overlapping area between these organs and PTVs.

Table 5.6 Dosimetric comparisons of OARs between 3D and 4D plans for six patients

OARs	Doses	PTV_{3D}	PTV_{4D}	p value
Ipsilateral lung	Mean dose (Gy)	19.74 ± 4.21	6.16 ± 3.26	<0.001
	Max dose (Gy)	71.93 ± 12.41	52.35 ± 19.54	<0.001
Contralateral lung	Mean dose (Gy)	1.14 ± 0.82	1.10 ± 0.68	ns
	Max dose (Gy)	18.41 ± 7.23	16.28 ± 8.52	ns
Heart	Mean dose (Gy)	11.87 ± 3.35	6.08 ± 1.28	<0.001
	Max dose (Gy)	55.41 ± 19.52	32.11 ± 18.96	<0.001
Spinal Cord	Mean dose (Gy)	2.10 ± 1.01	1.95 ± 2.14	ns
	Max dose (Gy)	25.74 ± 3.45	24.61 ± 5.43	ns

Student t test showed that there was no significant difference in contralateral lung and spinal cord between the 3D and 4D plans. ns: not significant.

(a)

(b)
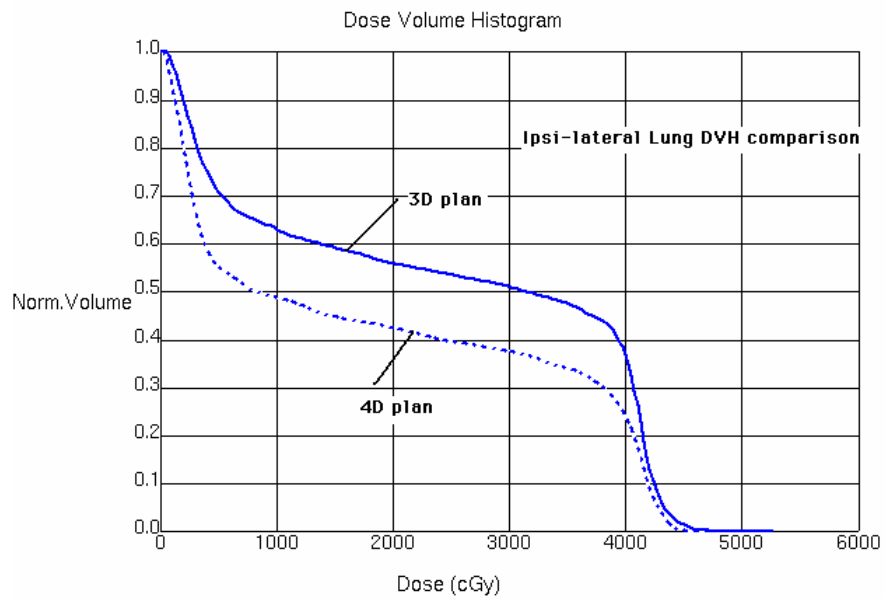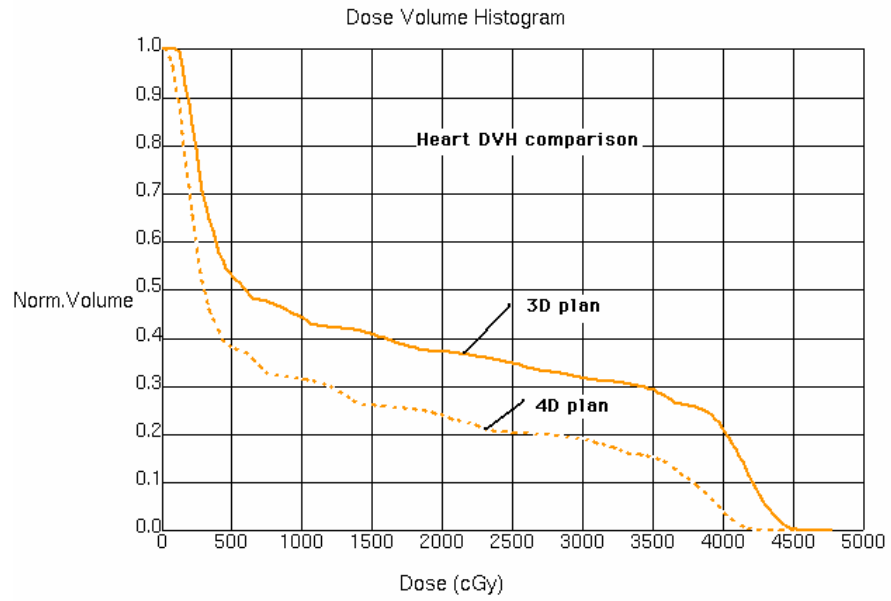
Figure 5.4 Comparison of heart DVHs (a) and ipsilateral lung DVHs (b) between 3D plan and 4D plan from patient #4 planning data.

Normal tissue complication probability (NTCP) comparison between 3D and 4D plans for ipsilateral lung, contralateral lung, cord and heart for six patients are summarized in Table 5.7. The NTCP from 4D plan was smaller than 3D plan for both ipsilateral lung and heart, and the differences were statistically significant. Since there was no biologically significant dose given to contralateral lung and spinal cord, these two OARs showed zero NTCP in this study.

Table 5.7 NTCP comparison between OARs for six patients.

	NTCP values 3D plan (%)	NTCP values 4D plan (%)	P value
Ipsilateral lung	5.64 ± 2.85	2.15 ± 1.54	<0.001
Contralateral lung	0*	0*	na
Spinal cord	0*	0*	na
heart	12.53 ± 9.87	5.45 ± 4.22	<0.001

*NTCP for contralateral lung and spinal cord was zero because there was no biologically significant dose given to them. Student t test showed that there was a significant difference for ipsilateral lung and heart between the 3D and 4D plans.

The study on target volume obtained from both 3D and 4D plans showed that the PTV$_{4D}$ was smaller than PTV$_{3D}$ (81.3% ± 6.8%) for all patients. This indicated that tumor motion was smaller than 3D plan estimation, so there could be unnecessary normal tissue being irradiated. However, for some cases, PTV$_{4D}$ was smaller than PTV$_{3D}$ (e.g., Patient #2), and there was some part of PTV$_{4D}$ not included in the PTV$_{3D}$. If the margins were chosen according to the current conventional experience (i.e., 7.4 mm lateral, 12 mm longitudinal and 6.8 mm vertical), both geometric miss of target and overdose of normal tissue could happen.

With the respiratory motion encoded 4DCT, the target volume could be delineated more accurately, and normal tissue could be spared more with the reduction of PTV_{4D}. The comparison of the plans showed that 4D plan could spare more normal ipsilateral lung and heart than 3D plan. The ipsilateral lung NTCP decreased from $5.64 \pm 4.85\%$ in 3D plan to 2.15 ± 1.54 % in 4D plan for ($p<0.001$); and heart NTCP decreased from 12.53 ± 9.87 % in 3D plan to 5.45 ± 4.22 % in 4D plan.

It should be noted that, although the Lyman NTCP model could be used to predict the normal tissue complication probability, the three parameters used in the model were different according to different researchers,[126] and were under influence of many factors, i.e., treatment method, disease diagnosis as primary or metastases, gender, et al. The parameters used in this study were from experimental data and were used as references to optimize and compare treatment plans. In practice, the clinician should carefully examine the model before to make any clinical decision.

The data in this study only represented randomly chosen patients with a natural free-breathing 4DCT simulation, which represents a single snapshot of the course of therapy. Because of the influence of the lung tumors and the possible co-existence of pulmonary disease, lung cancer patients are likely to have altered breathing patterns to compensate for the loss of pulmonary function. Furthermore, because the degree of tumor motion largely depends on how the patient breathes during a 4DCT session, the results could change dramatically if the patient was instructed differently (e.g., to breathe with full inspiration and expiration). In addition, patient breathing patterns will likely change during the course of therapy, which will result in large uncertainties in the ITV determination, even if it is done using 4DCT. To lift the limitation of the current data

sets, further studies should be pursued to prospectively assess the effects of changes in breathing patterns and tumor anatomy during the course of therapy by performing multiple 4DCT sessions in lung cancer patients.

5.3 Conclusions

Tumor motion trajectory does not necessary change with respiratory phases. For example, although the lung tidal volume is the maximum in phase 0 and minimum in phase 5, the tumor volume didn't follow the same pattern. Instead, the tumor volume reached maximum around phase 5 for patient #1 and around phase 6 for patient #5.

The PTV_{4D} volumes were smaller than PTV_{3D} in all six patients, no matter where the tumor was located in the lung. The dosimetric studies of PTV volume comparison between 3D and 4D plans showed that conventional margins added to CTV in 3D plan exceeded those actually needed and resulted in unnecessary irradiation of normal tissue. Detailed transverse view comparison showed that PTV_{3D} not only included excess normal tissues, but also might result in missing the target during certain phases of the breathing cycle in some cases.

4DCT images comprise patient-specific respiratory motion into treatment planning and could be used to ensure dose coverage of tumor during the breathing cycle. The IMRT planning comparison demonstrated that the 4D plan spared more normal tissue, e.g., ipsilateral lung and heart than 3D plan.

CHAPTER 6

Conclusions and Future Work

6.1 Conclusions

This study focused on using imaging guidance techniques to investigate organ motion which includes positional organ motion (or setup uncertainties) and internal organ motion during the daily radiation therapy treatment.

In Chapter 2, the interfractional setup uncertainties and intrafractional internal organ motion from different anatomic sites were studied with Helical TomoTherapy unit. The pre-treatment MVCT, which provides the real-time tumor and organ shift coordinates, was used to improve the accuracy of patient positioning. The setup errors of the five sites: HN, brain, prostate, abdomen and lung, were analyzed in this chapter. Among them, the mean interfractional setup errors for HN and brain were the smallest. The mean setup errors in the 3D translational for the five sites were 2.2 mm, 2.3 mm, 3.2 mm, 4.4 mm and 7.7 mm, respectively. The largest motion in lung was in the longitudinal direction, with mean error of 6.0 mm and standard deviation of 4.8 mm. The mean rotational variation for the five sites ranged from 0.2° to 0.5°, with the standard deviation from 0.7° to 0.9°. The maximum three dimensional intrafractional displacements were within 4.5mm. The observed overall variation from interfractional setup uncertainties was larger than the intrafractional organ motion. The setup variations from lateral, longitudinal and vertical were randomly distributed. The interfractional system errors and random errors were analyzed and the suggested margin for the five sites ranged from 4.2

to 8.2 mm, 5.0 mm to 12.0 mm, and 1.5 mm to 6.8 mm, in the direction of lateral, longitudinal and vertical, respectively.

In Chapter 3, preliminary data for lung SBRT using the MIDCO BodyLoc whole body stereotactic localizer, combined with TomoTherapy MVCT image guidance, were studied. In this chapter, eight lung cancer cases where the patients were treated with SBRT were retrospectively analyzed, and in total, 224 tumor shifts were recorded and analyzed to assess inter- and intrafractional tumor motion. For interfraction, the mean setup errors and standard deviations averaged across all patients were -1.1 ±2.8 mm, -2.5 ±8.7 mm, and 4.1 ±2.6 mm for lateral, longitudinal, and vertical variation, respectively; the mean setup rotational variation was -0.3° ±0.7°; and the maximum motion was 13.5 mm in the longitudinal direction. For intrafraction, the mean setup errors and standard deviations averaged across all patients were 0.1 ±0.7 mm, -0.3 ±2.0 mm, and 0.5 ±1.1 mm for the lateral, longitudinal, and vertical displacements, respectively; the mean rotational variation was 0.1° ±0.2°; and the maximum motion was 3.8 mm in the longitudinal direction. By comparing 3D displacement in the patient group with and without BodyLoc immobilization, the results showed that internal organ motion was reduced effectively by the BodyLoc immobilization devices. With the use of BodyLoc immobilization devices, the mean 3D displacement was reduced from 3.5mm to 1.7mm. Furthermore, no significant correlation was observed among patient characteristics, setup uncertainties and organ motion; and the interfractional setup uncertainties were higher than the observed intrafractional organ motion. These results suggest that image-guided stereotactic body radiotherapy using the BodyLoc system with TomoTherapy is a safe and reliable treatment method and can provide highly accurate target localization.

The application of B-spline deformable registration for four dimensional radiation therapy (4DRT) was investigated in Chapter 4. 4DCT is one of the clinically valuable tools for assessing respiration and tumor movement. Deformable registration between different breathing phases was performed with an algorithm to estimate the motion trajectory of the tumor. In this algorithm, the optimization is performed by minimizing the mean squared difference in intensity, and is implemented with a multi-resolution, gradient descent procedure. This algorithm saves clinician time for target delineation on only certain respiratory phases of the respiratory cycle in stead of all phases. The deformable registration was performed and tested between the extreme breathing phases and gives reasonably good results.

Chapter 5 described a lung tumor mobility evaluation study and compared dosimetric effects from 4DCT and traditional helical 3D CT scan. Respiratory GTV motion was characterized by assessing the GTV mass center in three dimensions with 4DCT. The coefficient of variation (standard deviation divided by average) of GTV ranged from 2.4% to 4.8% with an average of 3.4% during a respiratory cycle. The 3D centroid motion peak-to-peak amplitude of the GTVs caused by respiratory ranged from 3.0 mm to 10.4 mm, with an average of 5.8 mm and standard deviation of 2.5 mm. The averaged PTV volume for the selected six patients in the 4D (PTV_{4D}) was 304.2 cc and the averaged PTV volume in 3D (PTV_{3D}) was 367.0 cc. On average, the PTV_{4D} was 18.7% (range 11.2–26.8%) less than the PTV_{3D}. For some patients, although PTV_{4D} was smaller than PTV_{3D} (e.g., 266.3 cc vs. 315.5 cc), there was a part of PTV_{4D} not included in the posterior and lateral directions. This illustrated that PTV_{3D} not only included excess normal tissues in SI direction but also might result in missing the target during

certain phases of the breathing cycle. Statistically, the normal tissue complication probability (NTCP) from 4D plan was significantly smaller than 3D plan for both ipsilateral lung and heart.

In summary, this study has the following significance for both clinical and research purposes:

Firstly, a large patient population is involved in this positional organ motion study. Although there have been some publications on the similar research, this is one of the few studies that include five anatomy sites with a systematic study. The analytic results of interfractional setup uncertainties and intrafractional internal organ motion on these sites showed that the use of pre-treatment MVCT reduced the systematical setup error and hence can be used to improve the accuracy of patient positioning.

Secondly, this is the first study reported on the benefits of BodyLoc immobilization devices. The BodyLoc device is developed in-house with a neurosurgeon who worked very closely with the author. This device is under the application of FDA approval and ready for clinical application. The preliminary data for lung SBRT using this device, combining with TomoTherapy MVCT image guidance, showed significant improvement on tracking patient positional and organ motions and hence can produce a much better treatment outcome.

Thirdly, other than the usual clinical practice of using manual contour on each of the phases on 4DCT images to obtain ITV, this study attempts a real-time automatic segmentation delineation. This work significantly reduces radiation oncologist's time and has the potential of helping tracking anatomic changes and evaluating daily treatments in the future.

6.2 Future Work

6.2.1 Unresolved Issues in 4DCT

Although 4DCT is capable of providing accurate information on target and organ motion, there are some inherent issues that need to be further investigated. Among them, the first is that 4DCT uses phase rather than amplitude to sort data. If the breathing were perfectly regular from cycle to cycle, then phase- and amplitude-based sorting would give very similar results. However, inconsistent results arise when there is a variation in amplitude, period, or in baseline, or when the onset of end-expiration does not occur at the same point of each cycle. Under these circumstances, the sorted CT images may contain mismatch artifacts at the interface between bed positions (see Figure 6.1). Recent studies have investigated amplitude-based binning as an alternative to the phase-based approach, which may improve image quality in many cases.[127] Other researchers have matched adjacent CT slices without using a respiratory trace, by maximizing the continuity of CT units integrated over regions of interest.[35] The second issue with 4DCT is that there is a correlation between external fiducial movement and tumor and organ motion. Amplitude ratios between fiducial and tumor displacement may vary from cycle to cycle, and thoracic and abdominal points may involve relative phase shifts.[128] These shifts may be especially crucial for tumors near the lung, where hysteresis is prevalent. The third issue is that larger organs such as the liver can experience substantial deformation during inspiration and expiration, which may not be adequately captured by rigid-body interpolation between points in the respiratory cycle.

Figure 6.1 Example of 4DCT where respiratory cycle irregularities have produced significant mismatches near the base of the lung.

Finally, even if the 4DCT images have been acquired without problem, there remains the issue of reproducibility during patient treatment. In 4DCT based treatment planning and delivery, there is an assumption that anatomic motion during treatment will match the tumor and organ motion observed during setup. This assumption can be verified to some degree through frequent gated or breath-hold portal imaging. However, it is reasonable to assume the patients will relax over time, and their breathing becomes shallower or changes tempo. Indeed, studies have already demonstrated that some patients exhibit systematic respiratory changes over a multi-week course of radiation therapy, even with visual and audio coaching. All these unsolved issues strike at the heart of 4DCT, and provide a fertile ground for further research.

6.2.2 Solving the Problem of Tumor Mobility without 4DCT

4DCT is a good choice for reducing tumor and organ motion in routine clinic work. However, the expense of purchasing a 4DCT system sometimes hinders its clinical

implementation. For a clinic with limited budget, other non-4DCT approaches to reduce the tumor and organ motion need to be considered. Currently, there are several ways to handle the problem of tumor mobility in radiotherapy planning without using 4DCT. One approach is to use breath hold devices to immobilize the patient,[129] which shows a significant reduction of target motion. Another approach is to use respiratory gating[130] that does not directly compensate for breathing motion, so the radiation beam is switched off whenever the target is outside a predefined window. In clinic, a combination of both approaches is often applied, and the commercial systems based on them are currently available, e.g., deep inspiration breath hold[131] or active breath control[132]. Breath-holding techniques have the potential to reduce the effects of breathing motion,[58] however, in practice they are limited by the fact that many patients cannot tolerate holding their breath. On the other hand, gating techniques significantly increase the expense of time for the patient and the physician. There are some attempts to explicitly account for free breathing but these efforts suffer from little existing knowledge regarding the spatial-temporal behavior of anatomical and pathological structures involved. In a current study, the tracking of the tumor motion is done by a combination of external infrared emitters on the patient's surface and implanted gold fiducials. The position of the gold fiducials is then computed repeatedly by x-ray imaging. Although this may solve the technical problems arising for motion adaptive radiation therapy, an accurate non-invasive tracking method for following the tumor motion is still needed.

6.2.3 Adaptive Planning for Changing Target

With TomoTherapy, pre-treatment MVCT allows one to verify the correct patient setup and internal target and organ position prior to treatment. In addition to tumor localization, the CT images acquired during IGRT can be used to measure and evaluate the response to treatment. Recent studies have shown that lung tumors can substantially change in size, shape, density, and center of movement during the course of radiation therapy.[133-135]

During the course of this study, it was also observed that the GTV for some non–small-cell lung cancer (NSCLC) patients and head and neck patients decreased significantly during the radiation therapy treatment. Figure 6.2 shows the dramatic shifts and reduction in tumor volume for a patient with a large primary lung tumor. With the information from DVH, the daily delivered dose for GTV was not fully covered as desired because of the tumor shrinkage and movement.

(a: 0 Gy delivered)   (b: after 18.0 Gy)
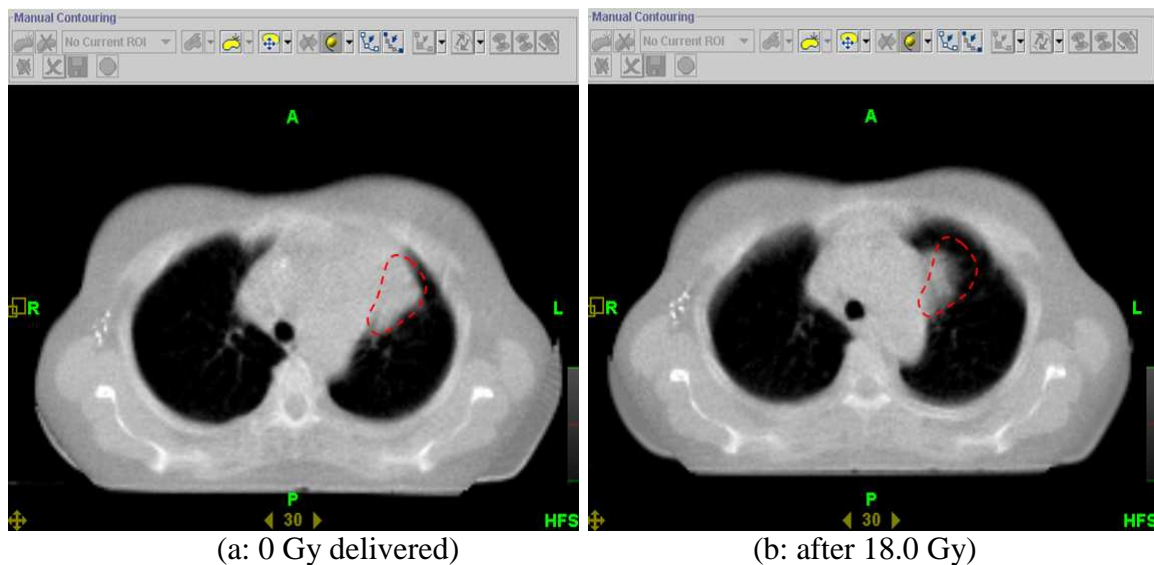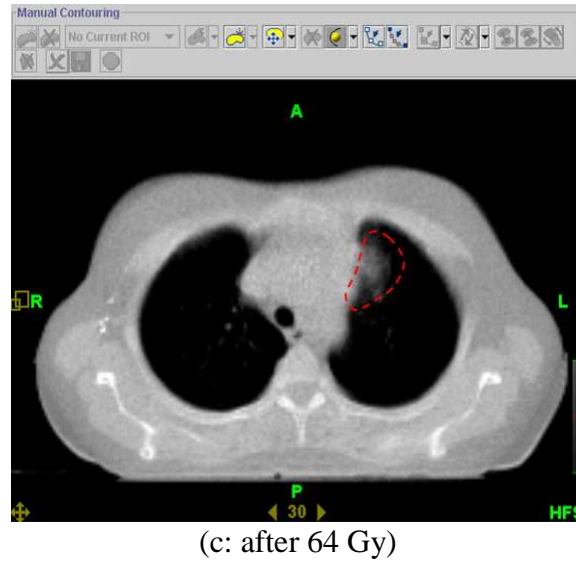
(c: after 64 Gy)

Figure 6.2 Changes in lung tumor volume and shape during the radiation treatment. Panel (a-c): comparison of a lung patient taken at the 1st (a), after 18.0 Gy (b), and after 64 Gy (c) using a daily dose of 2.0 Gy/fx.

Tumor volume changes also occur to other anatomic sites such as head and neck. Figure 6.3 shows the obvious response of one head and neck patient to radiation from treatment day #1 to day #10 and day #20. The DVHs in the figure were obtained by overlaying the initial treatment planning on the original tumor and OARs.

(a)

(b)
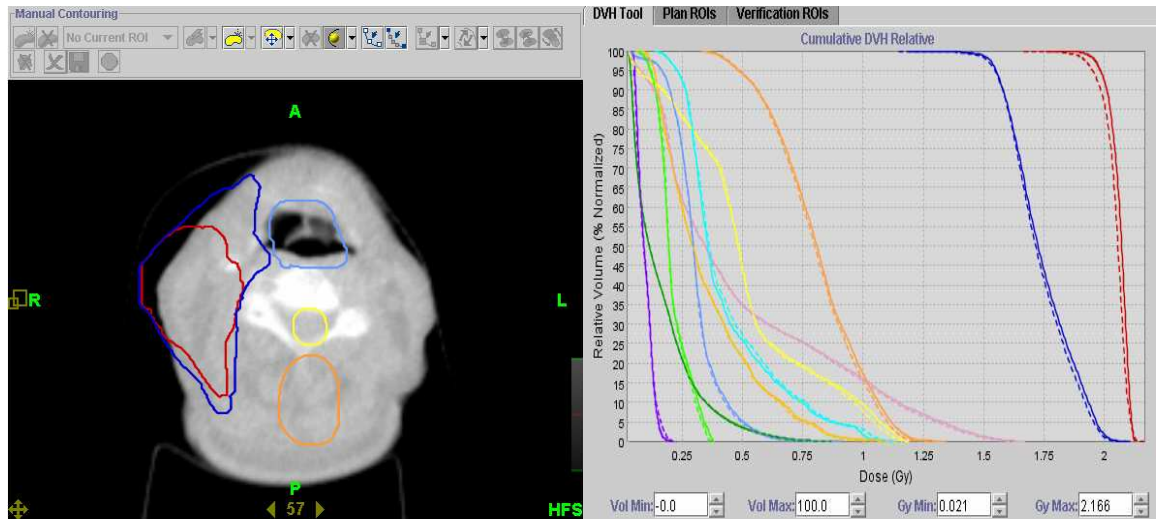
(c)

(d)
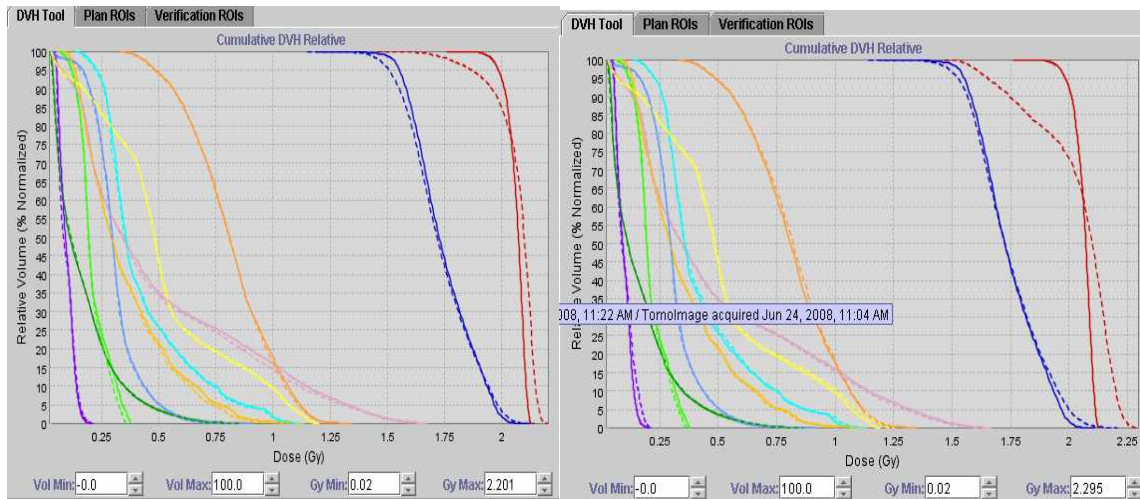
(e)   (f)

Figure 6.3 Examples of tumor volume changes in a head and neck cancer patient. Contours outlined from pre-treatment KVCT projected on the on-the-treatment MVCTs taken at the 1st (a), 10th(b), and 20th (c)treatment using daily dose of 1.8 Gy/fx. The color codes are: red: GTV, blue: PTV, light blue: larynx, yellow: spinal cord, and orange for the avoidance structure for planning; Panel (d-f): DHV of all organs including GTV and PTV for treatment day #1, #10, and #20 respectively. The DVHs were obtained using the initial treatment planning and initial definitions of tumor and OARs.

Based on these observations, a retrospective treatment planning study can be developed to evaluate the potential for adaptive radiation therapy. Adaptive radiation therapy is the next step in image-guided radiation therapy, where treatment delivery is modified to compensate for changes in patient anatomy. The specific goal of this treatment planning study is to give more accurate dose coverage for tumor and to spare normal tissue on a weekly or biweekly basis to compensate for reduction in GTV volume. The conceptual flow diagram of adaptive TomoTherapy is illustrated in Figure 6.4.
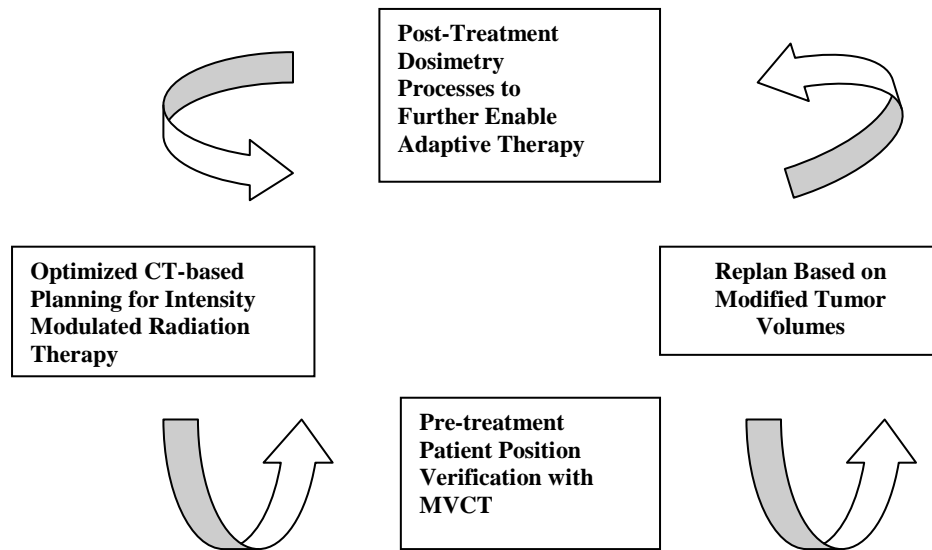
Figure 6.4 Conceptual flow diagram of adaptive TomoTherapy.

More specifically, the procedures involved in adaptive planning could include the following steps:

Step 1. Perform initial IMRT planning with simulation KVCT.

Step 2. Perform patient position verification and tumor volume reduction measurement during treatment with TomoTherapy or other IGRT tools. After image reconstruction, the MVCT images of the patients will be automatically fused with the treatment planning KVCT images on the operator station using a full image pixel-by-pixel deformable registration.

Step 3. Transfer MVCT images to contouring workstations, where the tumor volumes are outlined on each MVCT slice. The only structures that typically require modifications on the merged images are the ipsilateral lungs, GTVs and PTVs to account for target volume changes if for lung patient treatment.

Step 4. Overlay the initial treatment planning on the modified volumes if there is no need to change the plan. If there is a dramatic volume change, a new plan could be created based on the new structures.

Step 5. Summarize the total Dose Volume Histogram (DVH) for each patient underwent adaptive planning, and perform the post treatment dosimetry evaluation for further adaptive therapy.

References

1.   Brenner, DJ; Hlatky, LR; Hahnfeldt, PJ; Huang, Y; et al. The linear-quadratic model and most other common radiobiological models result in similar predictions of time-dose relationships. *Radiat. Res.* **150**:83-91; 1998.

2.   IMRT Collaborative Working Group. Intensity-modulated radiotherapy: Current status and issues of interest. *Int. J. Radiat. Oncol. Biol. Phys.* **51**:880 –914; 2001.

3.   AAPM IMRT Sub-Committee. Guidance document on delivery, treatment planning, and clinical implementation of IMRT: Report of the IMRT Subcommittee of the AAPM Radiation Therapy Committee. *Med. Phys.* **30**:2089 –2115; 2003.

4.   Galvin, JM; Ezzell, G.; Eisbrauch, A.; et al. Implementing IMRT in clinical practice: A joint document of the American Society for Therapeutic Radiology and Oncology and the American Association of Physicists in Medicine. *Int. J. Radiat. Oncol.Biol. Phys.* **58**:1616–1634; 2004.

5.   Zelefsky, MJ; Fuks, Z; Hunt, M. High-dose intensity modulated radiation therapy for prostate cancer: Early toxicity and biochemical outcome in 772 patients. *Int. J. Radiat. Oncol. Biol. Phys.* **53**:111-116; 2002.

6.   Hunt, MA; Zelefsky, MJ; Wolden, S. Treatment planning and delivery of intensity-modulated radiation therapy for primary nasopharynx cancer. *Int. J. Radiat. Oncol. Biol. Phys.* **49**:623–632; 2001.

7. Bel, A; Van Herk, M.; Lebesque, JV; et al. Target margins for random geometrical treatment uncertainties in conformal radiotherapy. *Med. Phys.* **23**:1537–1545; 1996.

8. Van Herk, M. Quantification of organ motion during conformal radiotherapy of the prostate by three dimensional image registration. *Int. J. Radiat. Oncol. Biol. Phys.* **33**:1311-1320; 1995.

9. Yan, D.; Wong; JW; Gustafson, G.; Martinez, A. . A new model for 'accept or reject' strategies in off-line and on-line megavoltage treatment evaluation. *Int. J. Radiat. Oncol. Biol.Phys. .* **31**:943–952; 1995.

10. Alasti, H; Petric, MP; Catton, CN; Warde, PR. Portal imaging for evaluation of daily on-line setup errors and off-line organ motion during conformal irradiation of carcinoma of the prostate. *Int. J. Radiat. Oncol. Biol. Phys.* **49**:869–884; 2001.

11. Byhardt, RW; Cox, JD; Hornburg, A. Weekly localization films and detection of field placement errors. *Int. J. Radiat. Oncol. Biol. Phys.* **4**:881–887; 1978.

12. Rabinowitz, I; Broomberg, J; Goitein, M. Accuracy of radiation field alignment in clinical practice. *Int. J. Radiat. Oncol. Biol. Phys.* **11**:1857–1867; 1985.

13. Rosenthal, SA; Galvin, JM; Goldwein, JW. Improved methods for determination of variability in patient positioning for radiation therapy using simulation and serial portal film measurements. *Int. J. Radiat. Oncol. Biol. Phys. .* **23**:621–625; 1992.

14. Boyer, AL; Antonuk, L; Fenster, A. A review of electronic portal imaging devices (EPIDs). *Med. Phys.* **19**:1-16; 1992.

15. Michalski, JM; Graham, MV; Bosch, WR. Prospective clinical evaluation of an electronic portal imaging device. *Int. J. Radiat. Oncol. Biol. Phys.* **34**:943–951; 1996.

16. Baily, NA; Horn, RA; Kampp, TD. Fluoroscopic visualization of megavoltage therapeutic x-0ray beams. *Int. J. Radiat. Oncol. Biol. Phys.* **6**:935–939; 1980.

17. Meertens, H; Van Herk M.; Bijhold, J. First clinical experience with a newly developed electronic portal imaging device. *Int. J. Radiat. Oncol. Biol. Phys.* **18**:1173–1181; 1990.

18. Valicenti, RK; Michalski, JM; Bosch, WR. Is weekly port filming adequate for verifying patient position in modern radiation therapy? . *Int. J. Radiat. Oncol. Biol. Phys.* **30**:431–438; 1994.

19. Herman, MG; Abrams, R; Mayer, RR. Clinical use of on-line portal imaging for daily patient treatment verification. *Int. J. Radiat. Oncol. Biol. Phys.* **28**:1017–1023; 1994.

20. Balter, JM; Chen, GT; Pelizzari, CA. Online repositioning during treatment of the prostate: A study of potential limits and gains. *Int. J. Radiat. Oncol. Biol. Phys.* . **27**:137–143; 1993.

21. Bel, A; Van Herk, M; Bartelink, H. A verification procedure to improve patient set-up accuracy using portal images. *Radiother. Oncol.* **29**:253–260; 1993.

22. Bissett, R; Boyko, S; Leszczynski, K. Radiotherapy portal verification: An observer study. *Br. J. Radiol.* **68**:165–174; 1995.

23. Perera, T; Moseley, J; Munro, P. Subjectivity in interpretation of portal films. *Int. J. Radiat. Oncol. Biol. Phys.* **45**:529–534; 1999.

24. Chen, JC. Novalis stereotactic radiosurgery and radiotherapy. Foreword. *Neurosurgery*. **62**:A1; 2008.

25. Lee, SW; Jin, JY; Guan, H; Martin, F*; et al.* Clinical assessment and characterization of a dual tube kilovoltage X-ray localization system in the radiotherapy treatment room. *J Appl Clin Med Phys*. **9**:2318; 2008.

26. Wurm, RE; Erbel, S; Schwenkert, I; Gum, F*; et al.* Novalis frameless image-guided noninvasive radiosurgery: initial experience. *Neurosurgery*. **62**:A11-17; discussion A17-18; 2008.

27. Grills, IS; Hugo, G; Kestin, LL; Galerani, AP*; et al.* Image-guided radiotherapy via daily online cone-beam CT substantially reduces margin requirements for stereotactic lung radiotherapy. *Int J Radiat Oncol Biol Phys*. **70**:1045-1056; 2008.

28. Thilmann, C; Nill, S; Tucking, T; Hoss, A*; et al.* Correction of patient positioning errors based on in-line cone beam CTs: clinical implementation and first experiences. *Radiat Oncol*. **1**:16; 2006.

29. Yin, FF; Wang, Z; Yoo, S; Jackie, Q*; et al.* Integration of Cone-Beam CT in Stereotactic Body Radiation Therapy. *Technol Cancer Res Treat*. **7**:133-140; 2008.

30. Grills, IS; Hugo, G; Kestin, LL; Galerani, AP*; et al.* Image-Guided Radiotherapy Via Daily Online Cone-Beam CT Substantially Reduces Margin Requirements for Stereotactic Lung Radiotherapy. *Int J Radiat Oncol Biol Phys*. **70**: 1045-562007.

31. Mackie, T; Olivera, G; Kapatoes, J. Helical Tomotherapy; Intensity-Modulated Radiation Therapy – The State of the Art. *Medical Physics Publishing*. 247–284; 2003.

32. Welsh, JS; Patel, RR; Ritter, MA, Harari, P; Mackie, T R; Mehta, M P. Helical Tomotherapy: An Innovative Technology and Approach to Radiation Therapy. *Technol. Canc. Res. Treat.* . **1**:55-63; 2002.

33. Jeraj, R; Mackie, TR; Balog, J; Olivera, G*; et al.* Radiation characteristics of helical Tomotherapy. *Med. Phys.* **31**:396–404; 2004.

34. Ford, EC; Mageras, GS; Yorke, E. Respiration-correlated spiral CT: A method of measuring respiratory-induced anatomic motion for radiation treatment planning. *Med Phys*. **30**:88 –97; 2003.

35. Pan, T; Lee, T; Rietzel, ER. 4D-CT imaging of a volume influenced by respiratory motion on multi-slice CT. *Med Phys*. **31**:333–340; 2004.

36. Underberg, RW; Lagerwaard, FJ; Slotman, BJ; Cuijpers, JP*; et al.* Benefit of respiration-gated stereotactic radiotherapy for stage I lung cancer: an analysis of 4DCT datasets. *Int J Radiat Oncol Biol Phys*. **62**:554-560; 2005.

37. Vander Geld, YG; Senan, S; JR., Van Sornsen de Koste JR. Evaluating mobility for radiotherapy planning of lung tumors: a comparison of virtual fluoroscopy and 4DCT. *Lung Cancer*. **53**:31–37; 2006.

38. ICRU Report 50. International Commission on Radiation Units and Measurements. Prescribing, recording and reporting photon beam therapy.1993.

39. ICRU Report 62. International Commission on Radiation Units and measurements. Prescribing, Recording and Reporting Photon Beam Therapy, . 1999.

40. Mayo, JR; M¨uller, NL; Henkelman, RM. The double-fissure sign: a motion artifact on thin-section CT scans *Radiology*. **165**:580–581; 1987.

41.   Ritchie, CJ; Hseih, J; Gard, MF; Godwin, JD; et al. Predictive respiratory gating: a new method to reduce motion artifacts on CT scans *Radiology*. **190**:847–852. 1994.

42.   Giraud, P; De Rycke, Y; Rosenwald, JC; Cosset, JM. Conformal radiotherapy planning for lung cancer: analysis of set-up uncertainties. *Cancer Invest*. **25**:38-46; 2007.

43.   Smith, RP; Bloch, P; Harris, EE; McDonough, J*; et al.* Analysis of interfraction and intrafraction variation during tangential breast irradiation with an electronic portal imaging device. *Int J Radiat Oncol Biol Phys*. **62**:373-378; 2005.

44.   Little, DJ; Dong, L; Levy, LB; Chandra, A; et al. Use of portal images and BAT ultrasonography to measure setup error and organ motion for prostate IMRT: implications for treatment margins. *Int J Radiat Oncol Biol Phys*. **56**:1218-1224; 2003.

45.   Trichter, F; Ennis, RD. Prostate localization using transabdominal ultrasound imaging. *Int J Radiat Oncol Biol Phys*. **56**:1225-1233; 2003.

46.   Ghilezan, M; Yan, D; Liang, J; Jaffray, D; et al. Online image-guided intensity-modulated radiotherapy for prostate cancer: How much improvement can we expect? A theoretical assessment of clinical benefits and potential dose escalation by improving precision and accuracy of radiation delivery. *Int J Radiat Oncol Biol Phys*. **60**:1602-1610; 2004.

47.   Letourneau, D; Martinez, AA; Lockman, D; Yan, D; et al. Assessment of residual error for online cone-beam CT-guided treatment of prostate cancer patients. *Int J Radiat Oncol Biol Phys*. **62**:1239-1246; 2005.

48. Oita, M; Ohmori, K; Obinata, K; Kinoshita, R; et al. Uncertainty in treatment of head-and-neck tumors by use of intraoral mouthpiece and embedded fiducials. *Int J Radiat Oncol Biol Phys*. **64**:1581-1588; 2006.

49. Xu, T; Wong, JT; Shikhaliev, PM; Ducote, JL; et al. Real-time tumor tracking using implanted positron emission markers: concept and simulation study. *Med Phys*. **33**:2598-2609; 2006.

50. Bijhold, J; Lebesque, JV; Hart, AA; Vijlbrief, RE. Maximizing setup accuracy using portal images as applied to a conformal boost technique for prostatic cancer. *Radiother Oncol*. **24**:261-271; 1992.

51. Stroom, JC; Koper, PC; Korevaar, GA; Van Os, M; et al. Internal organ motion in prostate cancer patients treated in prone and supine treatment position. *Radiother Oncol*. **51**:237-248; 1999.

52. Van Herk, M. Errors and margins in radiotherapy. *Semin Radiat Oncol*. **14**:52-64; 2004.

53. Keall, PJ; Mageras, GS; Balter, JM. The management of respiratory motion in radiation oncology. report of AAPM Task Group 76. *Med Phys*. **33**:3874 –3900; 2006.

54. Li, XA; Stepaniak, C; Gore, E. Technical and dosimetric aspects of respiratory gating using a pressure-sensor motion monitoring system. *Med Phys*. **33**:145–154; 2006.

55. Jin, JY; Ajlouni, M; Chen, Q; Yin, FF*; et al.* A technique of using gated-CT images to determine internal target volume (ITV) for fractionated stereotactic lung radiotherapy. *Radiother Oncol*. **78**:177-184; 2006.

56. Wurm, RE; Gum, F; Erbel, S; Schlenger, L; et al. Image guided respiratory gated hypofractionated Stereotactic Body Radiation Therapy (H-SBRT) for liver and lung tumors: Initial experience. *Acta Oncol*. **45**:881-889; 2006.

57. Mechalakos, J; Yorke, E; Mageras, GS; Hertanto, A; et al. Dosimetric effect of respiratory motion in external beam radiotherapy of the lung. *Radiother Oncol*. **71**:191-200; 2004.

58. Shirato, H; Seppenwoolde, Y; Kitamura, K; Onimura, R; et al. Intrafractional tumor motion: lung and liver. *Semin Radiat Oncol*. **14**:10-18; 2004.

59. Van de Steene, J; Van den Heuvel, F; Bel, A; Verellen, D; et al. Electronic portal imaging with on-line correction of setup error in thoracic irradiation: clinical evaluation. *Int J Radiat Oncol Biol Phys*. **40**:967-976; 1998.

60. Drabik, DM; MacKenzie, MA; Fallone, GB. Quantifying appropriate PTV setup margins: analysis of patient setup fidelity and intrafraction motion using post-treatment megavoltage computed tomography scans. *Int J Radiat Oncol Biol Phys*. **68**:1222-1228; 2007.

61. Beltran, C; Herman, MG; Davis, BJ. Planning target margin calculations for prostate radiotherapy based on intrafraction and interfraction motion using four localization methods. *Int J Radiat Oncol Biol Phys*. **70**:289-295; 2008.

62. Hugo, GD; Yan, D; Liang, J. Population and patient-specific target margins for 4D adaptive radiotherapy to account for intra- and inter-fraction variation in lung tumour position. *Phys Med Biol*. **52**:257-274; 2007.

63. Perkins, CL; Fox, T; Elder, E; Kooby, DA; et al. Image-guided radiation therapy (IGRT) in gastrointestinal tumors. *Jop*. **7**:372-381; 2006.

64. Shimizu, S; Shirato, H; Ogura, S; Akita-Dosaka, H; et al. Detection of lung tumor movement in real-time tumor-tracking radiotherapy. *Int J Radiat Oncol Biol Phys*. **51**:304-310; 2001.

65. Hodge, W; Tome, WA; Jaradat, HA; Orton, NP; et al. Feasibility report of image guided stereotactic body radiotherapy (IG-SBRT) with tomotherapy for early stage medically inoperable lung cancer using extreme hypofractionation. *Acta Oncol*. **45**:890-896; 2006.

66. Lee, SW; Choi, EK; Park, HJ; Ahn, SD; et al. Stereotactic body frame based fractionated radiosurgery on consecutive days for primary or metastatic tumors in the lung. *Lung Cancer*. **40**:309-315; 2003.

67. Ng, AW; Tung, SY; Wong, VY. Hypofractionated stereotactic radiotherapy for medically inoperable stage I non-small cell lung cancer - report on clinical outcome and dose to critical organs. *Radiother Oncol*. **87**:24-28; 2008.

68. Timmerman, R; Papiez, L; McGarry, R; Likes, L; et al. Extracranial stereotactic radioablation: results of a phase I study in medically inoperable stage I non-small cell lung cancer. *Chest*. **124**:1946-1955; 2003.

69. Fuss, M; Salter, BJ; Rassiah, P; Cheek, D; et al. Repositioning accuracy of a commercially available double-vacuum whole body immobilization system for stereotactic body radiation therapy. *Technol Cancer Res Treat*. **3**:59-67; 2004.

70. Negoro, Y; Nagata, Y; Aoki, T; Mizowaki, T; et al. The effectiveness of an immobilization device in conformal radiotherapy for lung tumor: reduction of respiratory tumor movement and evaluation of the daily setup accuracy. *Int J Radiat Oncol Biol Phys*. **50**:889-898; 2001.

71. Kimura, T; Hirokawa, Y; Murakami, Y; Tsujimura, M; et al. Reproducibility of organ position using voluntary breath-hold method with spirometer for extracranial stereotactic radiotherapy. *Int J Radiat Oncol Biol Phys*. **60**:1307-1313; 2004.

72. Stock, M; Kontrisova, K; Dieckmann, K; Bogner, J; et al. Development and application of a real-time monitoring and feedback system for deep inspiration breath hold based on external marker tracking. *Med Phys*. **33**:2868-2877; 2006.

73. Wang, L; Feigenberg, S; Chen, L; Pasklev, K; et al. Benefit of three-dimensional image-guided stereotactic localization in the hypofractionated treatment of lung cancer. *Int J Radiat Oncol Biol Phys*. **66**:738-747; 2006.

74. Slotman, BJ; Lagerwaard, FJ; Senan, S. 4D imaging for target definition in stereotactic radiotherapy for lung cancer. *Acta Oncol*. **45**:966-972; 2006.

75. Guckenberger, M; Meyer, J; Wilbert, J; Baier, K; et al. Cone-beam CT based image-guidance for extracranial stereotactic radiotherapy of intrapulmonary tumors. *Acta Oncol*. **45**:897-906; 2006.

76. Purdie, TG; Moseley, DJ; Bissonnette, JP; Sharpe, MB; et al. Respiration correlated cone-beam computed tomography and 4DCT for evaluating target motion in Stereotactic Lung Radiation Therapy. *Acta Oncol*. **45**:915-922; 2006.

77. Hinson, WH; Kearns, WT; Ellis, TL; Sprinkle, D; et al. Reducing set-up uncertainty in the Elekta Stereotactic Body Frame using Stealthstation software. *Technol Cancer Res Treat*. **6**:181-186; 2007.

78. AAPM Report 54. Stereotactic radiosurgery. New York: Radiation therapy committee; 1995.

79. Lagerwaard, FJ; Van Sornsen de Koste, JR; Nijssen-Visser, MR; Schuchhard-Schipper, RH; et al. Multiple "slow" CT scans for incorporating lung tumor mobility in radiotherapy planning. *Int J Radiat Oncol Biol Phys*. **51**:932-937; 2001.

80. Smeenk, C; Gaede, S; Battista, JJ. Delineation of moving targets with slow MVCT scans: implications for adaptive non-gated lung tomotherapy. *Phys Med Biol*. **52**:1119-1134; 2007.

81. Purdie, TG; Bissonnette, JP; Franks, K; Bezjak, A; et al. Cone-beam computed tomography for on-line image guidance of lung stereotactic radiotherapy: localization, verification, and intrafraction tumor position. *Int J Radiat Oncol Biol Phys*. **68**:243-252; 2007.

82. Le, QT; Loo, BW; Ho, A; Cotrutz, C; et al. Results of a phase I dose-escalation study using single-fraction stereotactic radiotherapy for lung tumors. *J Thorac Oncol*. **1**:802-809; 2006.

83. Nelson, C; Starkschall, G; Chang, JY. The potential for dose escalation in lung cancer as a result of systematically reducing margins used to generate planning target volume. *Int J Radiat Oncol Biol Phys*. **65**:573-586; 2006.

84. Kong, FM; Ten Haken, RK; Schipper, MJ; Sullivan, MA; et al. High-dose radiation improved local tumor control and overall survival in patients with inoperable/unresectable non-small-cell lung cancer: long-term results of a radiation dose escalation study. *Int J Radiat Oncol Biol Phys*. **63**:324-333; 2005.

85. Bradley, J. A review of radiation dose escalation trials for non-small cell lung cancer within the Radiation Therapy Oncology Group. *Semin Oncol*. **32**:S111-113; 2005.

86. Schild, SE; Korte, SM; Wong, WW; Vora, SA; et al. Treatment planning for dose escalation in non-small cell lung cancer (NSCLC). *Med Dosim*. **29**:196-203; 2004.

87. Wu, KL; Jiang, GL; Liao, Y; Qian, H; et al. Three-dimensional conformal radiation therapy for non-small-cell lung cancer: a phase I/II dose escalation clinical trial. *Int J Radiat Oncol Biol Phys*. **57**:1336-1344; 2003.

88. Allen, AM; Siracuse, KM; Hayman, JA; Balter, JM. Evaluation of the influence of breathing on the movement and modeling of lung tumors. *Int J Radiat Oncol Biol Phys.* **58**:1251–1257; 2004.

89. Ekberg L; HO, Wittgren L; Bjelkengren G;Landberg T. What margins should be added to the clinical target volume in radiotherapy treatment planning for lung cancer? *Radiother Oncol. .* **48**:71–77; 1998.

90. Aruga, T; Itami, J; Aruga, M. Target volume definition for upper abdominal irradiation using CT scans obtained during inhale and exhale phases. *Int J Radiat Oncol Biol Phys.* **48**:465–469; 2000.

91. Gagne, I; Robinson, D. The impact of tumor motion upon CT image integrity and target delineation. *Med Phys. .* **12**:3378–3392; 2004.

92. Chen, G; Kung, J; Beaudette, K. Artifacts in computed tomography scanning of moving objects. *Geriatr. Nephrol. Urol.* **14**:19–26; 2004.

93. Balter, J; Ten Haken, R; Lawrence, T; LamL, K; et al. Uncertainties in CT-based radiation therapy planning associated with patient breathing. *Int. J. Radiat. Oncol., Biol., Phys.* **36**:167–174; 1996.

94. Shimizu, S; Shirato, H; Kagei, K; Nishioka, T; et al. Impact of respiratory movement on the computed tomographic images of small lung tumors in three-dimensional radiotherapy. *Int. J. Radiat. Oncol., Biol., Phys.* **46**:1127-1133; 2000.

95. Balter, J; Lam, K; McGinn, C; Lawrence, T; et al. Improvement of CT-based treatment planning model of abdominal targets using static exhale imaging. *Int. J. Radiat. Oncol., Biol., Phys.* **41**:939–943; 1998.

96. Remouchamps, VM; Letts, N; Yan, D; Vicini, FA; et al. Three-dimensional evaluation of intra- and interfraction immobilization of lung and chest wall using active breathing control: a reproducibility study with breast cancer patients. *Int J Radiat Oncol Biol Phys*. **57**:968-978; 2003.

97. Wilson, EM; Williams, FJ; Lyn, BE; Wong, JW; et al. Validation of active breathing control in patients with non-small-cell lung cancer to be treated with CHARTWEL. *Int J Radiat Oncol Biol Phys*. **57**:864-874; 2003.

98. Mageras, G; Pevsner, A; York, E. Measurement of lung tumor motion using respiration-correlated CT. *Int J Radiat Oncol Biol Phys*. **60**:933–941; 2004.

99. Underberg, RW; Lagerwaard, FJ; Cuijpers, JP; Slotman, BJ; et al. Four-dimensional CT scans for treatment planning in stereotactic radiotherapy for stage I lung cancer. *Int J Radiat Oncol Biol Phys*. **60**:1283-1290; 2004.

100. Schreibmann, E; Chen, GT; Xing, L. Image interpolation in 4D CT using a BSpline deformable registration model. *Int J Radiat Oncol Biol Phys.* . **1**:1537-1550; 2006.

101. Coselmon, MMB, J.M.; McShan, D.L.; et al. . Mutual information based CT registration of the lung at exhale and inhale breathing states using thin-plate splines. *Med. Phys.* **31**:2942–2948; 2004.

102. Luo, G; Heng, PA. LV shape and motion: B-spline-based deformable model and sequential motion decomposition. *IEEE Trans Inf Technol Biomed.* **9**:430-446; 2005.

103. Klein, AK; Lee, F; Amini, AA. Quantitative coronary angiography with deformable spline models. *IEEE Trans Med Imaging.* **16**:468-482; 1997.

104. Lu, W; Chen, ML; Olivera, GH; Ruchala K, J; et al. Fast free-form deformable registration via calculus of variations. *Phys. Med. Biol.* . **49**:3067–3087; 2004.

105. Hawkes, DJ; Barratt, D; Blackall, JM; Chan, C; et al. Tissue deformation and shape models in image-guided interventions: a discussion paper. *Med. Image Anal.* **9**:163–175; 2005.

106. Ragan, D; Starkschall, G; McNutt, T; Kaus, M; et al. Semiautomated four-dimensional computed tomography segmentation using deformable models. *Med. Phys.* . **32**:2254–2261; 2005.

107. Wang, H; Dong, L; O'Daniel, J; Mohan, R; et al. Validation of an accelerated 'demons' algorithm for deformable image registration in radiation therapy. *Phys. Med. Biol.* . **50**:2887–2905; 2005.

108. Bharath, A; Hirose, M; Hata, N. Evaluation of threedimensional finite element-based deformable registration of preand intraoperative prostate imaging. *Med. Phys.* **28**:2551–2560; 2001.

109. Brock, KK; McShan, DL; Balter, JM. A comparison of computer- controlled versus manual on-line patient setup adjustment. *J. Appl. Clin. Med. Phys.* **3**:241–247; 2002.

110. Schreibmann, E; Xing, L. Narrow band deformable registration of prostate MRI/MRSI and CT studies. *Int. J. Radiat. Oncol. Biol. Phys.* **62**:595–605; 2005.

111. Bookstein, FL. Thin plate splines and the decomposition of deformations. *IEEE Trans. Pattern Anal. Mach. Intell.* . **11**:567– 585; 1989.

112. Guerrero, T; Zhang, G; Huang, TC. Intrathoracic tumor motion estimation from CT imaging using the 3D optical flow method. . *Phys. Med. Biol.* **49**:4147–4161; 2004.

113. Mageras, GS; Pevsner, A; Yorke, ED. Measurement of lung tumor motion using respiration-correlated CT. *Int. J. Radiat. Oncol. Biol. Phys.* . **60**:933–941; 2004.

114. Fei, B; Wheaton, A; Lee, Z; Duerk, JL; et al. Automatic MR volume registration and its evaluation for the pelvis and prostate. *Phys Med Biol*. **47**:823-838; 2002.

115. Lian, JX, L.; Hunjan, S.; et al. Mapping of the prostate in endorectal coil-based MRI/MRSI and CT: A deformable registration and validation study. *Med. Phys.* . **31**:3087–3094; 2004.

116. Rietzel, E; Chen, GT; Choi, NC; Willet, CG. Four-dimensional image-based treatment planning: Target volume segmentation and dose calculation in the

presence of respiratory motion. *Int J Radiat Oncol Biol Phys*. **61**:1535-1550; 2005.

117. Zhang, T; Orton, NP; Tome, WA. On the automated definition of mobile target volumes from 4D-CT images for stereotactic body radiotherapy. *Med Phys*. **32**:3493-3502; 2005.

118. Rietzel, E; Chen, GT; Choi, NC. Four-dimensional image based treatment planning: Target volume segmentation and dose calculation in the presence of respiratory motion. *Int J Radiat Oncol Biol Phys*. **61**:1535–1550; 2005.

119. Lyman, JT. Complication probability as assessed from dose volume histograms. *Radiat Res*. **8**:S13–S19; 1985.

120. Kallman, P; Agren, A; Brahme, A. Tumour and normal tissue responses to fractionated non-uniform dose delivery. *Int J Radiat Biol*. **62**:249-262; 1992.

121. Zaider, M; Amols, HI. Practical considerations in using calculated healthy - tissue complication probabilities for treatment - plan optimization. . *Int J Radiat Oncol Biol Phys.* **44**:439– 447; 1999.

122. Kehwar, TS; Sharma, SC. The best fit of the normal tissue tolerance data to the multiple component model. *Polish J Med Phys Eng*. **9**:239– 269; 2003.

123. Kehwar, TS. Analytical approach to estimate normal tissue complication probability using best fit of normal tissue tolerance doses into the NTCP equation of the linear quadratic model. *J Cancer Res Ther.* **1**:168–179; 2005.

124. Emami, B; Lyman, J; Brown, A. Tolerance of normal tissue to therapeutic radiation. *Int J Radiat Oncol Biol Phys.* **21**:109– 122; 1991.

125.   Burman, CM; Kutcher, GJ; Emami, B; Goitein, M. Fitting of normal tissue tolerance data to an analytic function. *Int J Radiat Oncol Biol Phys.* **21**:123-135; 1991.

126.   Webb, T; Nahum, AE. A model for calculating tumour control probability in radiotherapy including the effects of inhomogeneous distributions of dose and clonogenic cell density. *Phys. Med. Biol. .* **38**:653– 666; 1993.

127.   Starkschall, GH, S.; Keall, P.J.; et al. . XIVth International Conference on the Use of Computers in Radiation Therapy, 2004, pp 53. Displacement based binning of 4-D CT image data sets. XIVth International Conference on the Use of Computers in Radiation Therapy; 2004.

128.   Seppenwoolde, YS, H.; Kitamura, K. Precise and real-time measurement of 3D tumor motion in lung due to breathing and heartbeat, measured during radiotherapy. *Int. J. Radiat. Oncol. Biol. Phys. .* **53**:822-834; 2002.

129.   Lax, I; Blomgren, H; Naslund, I; Svanstrom, R. Stereotactic radiotherapy of malignancies in the abdomen. *Methodological aspects. Acta Oncol* **33**:677–683; 1994.

130.   Kubo, HD; Hill, BC. Respiration gated radiotherapy treatment: a technical study. *Phys Med Biol.* **41**:83-91; 1996.

131.   Rosenzweig, K; Hanley, J; Mah, D. The deep inspiration breath-hold technique in the treatment of inoperable non-small-cell lung cancer. *Int J Radiat Oncol Biol Phys* **48**:81–87; 2000.

132.   Wong, JW; Sharpe, MB; Jaffray, DA; Kini, VR; et al. The use of active breathing control (ABC) to reduce margin for breathing motion. *Int J Radiat Oncol Biol Phys*. **44**:911-919; 1999.

133.   Ramsey, CR; Langen, KM; Kupelian, PA. A technique for adaptive image-guided helical tomotherapy for lung cancer. *Int J Radiat Oncol Biol Phys*. **64**:1237–1244; 2006.

134.   Underberg, WM; Lagerwaard, FJ; Tinteren, HV. Time trends in target volumes for stage I non-small-cell lung cancer after stereotactic radiotherapy. *Int J Radiat Oncol Biol Phys*. **64**:1221–1228; 2006.

135.   Kupelian, PA; Ramsey, CR; Meeks, SL. Serial megavoltage CT imaging during external beam radiotherapy for non–small-cell lung cancer: Observations on tumor regression during treatment. *Int J Radiat Oncol Biol Phys* **63**:1024–1028; 2005.

Appendix **A**

ANOVA Test with Bonferroni Post-hoc Comparisons for Five Sites

SPSS (V16.0) was used for lateral displacement analysis in interfractional setup uncertainty comparisons among five anatomic sites. (group 1: HN; group 2: Brain; group 3: prostate; group 4: abdomen; group 5: lung)

Multiple Comparisons

Displacement in lateral direction

Bonferroni

(I) group	(J) group	Mean Difference (I-J)	Std. Error	Sig.	95% Confidence Interval	
					Lower Bound	Upper Bound
1.00	2.00	-.17126	.32396	1.000	-1.0821	.7395
	3.00	-2.70553*	.28654	.000	-3.5111	-1.8999
	4.00	-4.38139*	.40312	.000	-5.5147	-3.2481
	5.00	-4.42115*	.29101	.000	-5.2393	-3.6030
2.00	1.00	.17126	.32396	1.000	-.7395	1.0821
	3.00	-2.53427*	.30851	.000	-3.4016	-1.6669
	4.00	-4.21013*	.41901	.000	-5.3882	-3.0321
	5.00	-4.24989*	.31266	.000	-5.1289	-3.3708
3.00	1.00	2.70553*	.28654	.000	1.8999	3.5111
	2.00	2.53427*	.30851	.000	1.6669	3.4016
	4.00	-1.67586*	.39080	1.000	-2.7746	-.5772
	5.00	-1.71562*	.27370	1.000	-2.4851	-.9461
4.00	1.00	4.38139*	.40312	.000	3.2481	5.5147
	2.00	4.21013*	.41901	.000	3.0321	5.3882
	3.00	1.67586*	.39080	1.000	.5772	2.7746
	5.00	-.03975	.39409	1.000	-1.1477	1.0682

Multiple Comparisons (cont.)

displacement

Bonferroni

(I) group	(J) group	Mean Difference (I-J)	Std. Error	Sig.	95% Confidence Interval	
					Lower Bound	Upper Bound
5.00	1.00	4.42115*	.29101	.000	3.6030	5.2393
	2.00	4.24989*	.31266	.000	3.3708	5.1289
	3.00	1.71562*	.27370	1.000	.9461	2.4851
	4.00	.03975	.39409	1.000	-1.0682	1.1477

*. The mean difference is significant at the 0.05 level.

Appendix B

Source Code of Deformable Registration

Step 1.   Matlab code: convert 4DCT image to mha file

File name: dicomtomha3D.m

```matlab
% /* dicomtomha3D.m */
clear all
close all

indir = 'c:/4DCT/IMG/CT10010/4D_LUNG/T90/';
outfn = 'c:/4DCT/IMG/CT10010/4D_LUNG/t9.mha';
d = dir(indir);

for di = 3 : length(d)
    n = d(di).name;
    fn = [indir, n];
    A = dicomread(fn);
    MHD(:,:,di-2) = A';
end

info = dicominfo(fn);
offset = info.ImagePositionPatient';
spacing = [info.PixelSpacing' 2.5];

writemha(outfn, MHD, offset, spacing, 'short');
```

File name: dicominfo.m

```matlab
% /* **************************************************/
% dicominfo Read a DICOM image: image tool box
% /* **************************************************/
function writemha(fn,A,offset,spacing,type)
%% writemha(fn,A,offset,spacing,type)
%%   fn       filename
%%   A        Volume
%%   offset
%%   spacing
%%   type     'uchar','float', or 'short'
```

```
if (ndims(A) ~= 3)
  error ('Sorry, only 3D volumes supported');
end

fp = fopen(fn,'w');
error ('Cannot open mha file for writing');
end

fprintf (fp,'ObjectType = Image\n');
fprintf (fp,'NDims = 3\n');
fprintf (fp,'BinaryData = True\n');
fprintf (fp,'BinaryDataByteOrderMSB = False\n');
fprintf (fp,'Offset = ');
fprintf (fp,' %g',offset);
fprintf (fp,'\n');
fprintf (fp,'ElementSpacing = ');
fprintf (fp,' %g',spacing);
fprintf (fp,'\n');
fprintf (fp,'DimSize = ');
fprintf (fp,' %d',size(A));
fprintf (fp,'\n');
switch(lower(type))
 case 'uchar'
  fprintf (fp,'ElementType = MET_UCHAR\n');
  fprintf (fp,'ElementDataFile = LOCAL\n');
  fwrite (fp,A,'uint8');
 case 'short'
  fprintf (fp,'ElementType = MET_SHORT\n');
  fprintf (fp,'ElementDataFile = LOCAL\n');
  fwrite (fp,A,'int16');
 case 'float'
  fprintf (fp,'ElementType = MET_FLOAT\n');
  fprintf (fp,'ElementDataFile = LOCAL\n');
  fwrite (fp,A,'real4');
 otherwise
  fclose(fp);
  error ('Sorry, unsupported type');
end

fclose(fp);
```

Step 2.   Script of deformable registration with ITK tool kit

Script file: run_registration.bat

```
    ra_registration.exe  BS_882.txt
    date /T
    time /T
    ra_registration.exe  BS_442.txt
    date /T
    time /T
    ra_registration.exe  BS_441.txt
    date /T
    time /T
    ra_registration.exe  BS_221.txt
```

Config file:

```
[GLOBAL]
fixed=c:\4DCT\IMG\CT10010\4D_LUNG\t5.mha
moving=c:\4DCT\IMG\CT10010\4D_LUNG\t0.mha
img_out=c:\4DCT\IMG\CT10010\4D_LUNG\bspline_output_05_221.mha

[STAGE]
xform=bspline
optim=lbfgsb
metric=mse
grad_tol=0.05
convergence_tol=5.0
max_its=200
grid_spac=15 15 15
num_grid=15 15 15
res=8 8 4

[STAGE]
res=8 8 2

[STAGE]
res=4 4 2

[STAGE]
res=4 4 1

[STAGE]
res=2 2 1
```

Step 3.   Matlab code: convert .mha file to .nii file

File name: main_mha2nill.m

```
mha_to_nii('bspline_output_05_221.mha','bspline_output_05_221.nii');
mha_to_nii('bspline_output_05_441.mha','bspline_output_05_441.nii');
mha_to_nii('bspline_output_05_442.mha','bspline_output_05_442.nii');
mha_to_nii('bspline_output_05_882.mha','bspline_output_05_882.nii');
```

File name: mha_to_nii.m

```
function mha_to_nii(mhafn, niifn)

[A, Ainfo] = readmha(mhafn);

origin = -Ainfo.Offset';

B = flipdim(A, 2);

nii = make_nii(B, [], origin, 4);

save_nii(nii, niifn);


%end of mha_to_nii()


function [A, Ainfo] = readmha(fn)
nii = make_nii(varargin)
function save_nii(nii, fileprefix, old_RGB)

%All the three functions above are from ITK tool kit
```

Step 4.   Display and analyze the images with MRIcro

Vita

Jining Zhou was born on September, 1970 in Nantong, Jiangsu, China. She earned her Bachelor of Engineering degree with a major in Chemistry at Central South University of Technology, China, in 1992. She received her Master's degree in Chemical Engineering at Guangxi University in 1995, and worked as a research associate in the Biochemistry Department in East China University of Science and Technology, Shanghai, China, from 1995 to 1998. In 1999 she was admitted to Virginia Commonwealth University, and received her Master's degree in Biomedical Engineering in 2001. She has been working as a clinical medical physicist in the Department of Radiation Oncology, at Mount Sinai Medical Center, New York, from 2002 to 2006, and at Sharp Grossmont Hospital, San Diego, since 2007.